





**UNIVERSIDAD DE INVESTIGACIÓN DE TECNOLOGÍA  
EXPERIMENTAL YACHAY**

**Escuela de Ciencias Físicas e Ingeniería**

**TÍTULO: Design of Doped and Co-Doped Hydroxyapatite Nanoparticles  
with Ceria Nanoparticles and Lithium ions with Potential  
Bioimaging Applications**

Trabajo de integración curricular presentado como requisito para la  
obtención del título de Ingeniero en Nanotecnología

**Autor:**

Pesantez Torres Fernando Alexander

**Tutora:**

Gema González, Ph.D

**Co-tutor:**

Manuel Caetano, Ph.D

Urcuquí, Noviembre 2020



Urcuquí, 6 de noviembre de 2020

**SECRETARÍA GENERAL**  
(Vicerrectorado Académico/Cancillería)  
**ESCUELA DE CIENCIAS FÍSICAS Y NANOTECNOLOGÍA**  
**CARRERA DE NANOTECNOLOGÍA**  
**ACTA DE DEFENSA No. UITEY-PHY-2020-00018-AD**

A los 6 días del mes de noviembre de 2020, a las 15:30 horas, de manera virtual mediante videoconferencia, y ante el Tribunal Calificador, integrado por los docentes:

**Presidente Tribunal de Defensa** Dr. CHACON TORRES, JULIO CESAR , Ph.D.

**Miembro No Tutor** Dra. BRICEÑO ARAUJO, SARAH ELISA , Ph.D.

**Tutor** Dra. GONZALEZ VASQUEZ, GEMA , Ph.D.

El(la) señor(ita) estudiante **PESANTEZ TORRES, FERNANDO ALEXANDER**, con cédula de identidad No. **1401065691**, de la **ESCUELA DE CIENCIAS FÍSICAS Y NANOTECNOLOGÍA**, de la Carrera de **NANOTECNOLOGÍA**, aprobada por el Consejo de Educación Superior (CES), mediante Resolución **RPC-SO-13-No.156-2015**, realiza a través de videoconferencia, la sustentación de su trabajo de titulación denominado: **DESIGN OF DOPED AND CO-DOPED HYDROXYAPATITE NANOPARTICLES WITH CERIA NANOPARTICLES AND LITHIUM IONS WITH POTENTIAL BIOMAGING APPLICATIONS**, previa a la obtención del título de **INGENIERO/A EN NANOTECNOLOGÍA**.

El citado trabajo de titulación, fue debidamente aprobado por el(los) docente(s):

**Tutor** Dra. GONZALEZ VASQUEZ, GEMA , Ph.D.

Y recibió las observaciones de los otros miembros del Tribunal Calificador, las mismas que han sido incorporadas por el(la) estudiante.

Previamente cumplidos los requisitos legales y reglamentarios, el trabajo de titulación fue sustentado por el(la) estudiante y examinado por los miembros del Tribunal Calificador. Escuchada la sustentación del trabajo de titulación a través de videoconferencia, que integró la exposición de el(la) estudiante sobre el contenido de la misma y las preguntas formuladas por los miembros del Tribunal, se califica la sustentación del trabajo de titulación con las siguientes calificaciones:

Tipo	Docente	Calificación
Presidente Tribunal De Defensa	Dr. CHACON TORRES, JULIO CESAR , Ph.D.	9,0
Tutor	Dra. GONZALEZ VASQUEZ, GEMA , Ph.D.	10,0
Miembro Tribunal De Defensa	Dra. BRICEÑO ARAUJO, SARAH ELISA , Ph.D.	9,0

Lo que da un promedio de: **9.3 (Nueve punto Tres)**, sobre 10 (diez), equivalente a: **APROBADO**

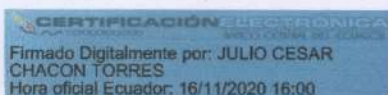
Para constancia de lo actuado, firman los miembros del Tribunal Calificador, el/la estudiante y el/la secretario ad-hoc.

Certifico que *en cumplimiento del Decreto Ejecutivo 1017 de 16 de marzo de 2020, la defensa de trabajo de titulación (o examen de grado modalidad teórico práctica) se realizó vía virtual, por lo que las firmas de los miembros del Tribunal de Defensa de Grado, constan en forma digital.*

PESANTEZ TORRES, FERNANDO ALEXANDER  
**Estudiante**

*Fernando Pesantez*

Dr. CHACON TORRES, JULIO CESAR , Ph.D.  
**Presidente Tribunal de Defensa**



Dra. GONZALEZ VASQUEZ, GEMA , Ph.D.  
**Tutor**

**CERTIFICACIÓN ELECTRÓNICA**  
Firmado Digitalmente por: GEMA GONZALEZ  
VAZQUEZ  
Hora oficial Ecuador: 16/11/2020 07:42

Dra. BRICEÑO ARAUJO, SARAH ELISA , Ph.D.  
**Miembro No Tutor**



Firmado digitalmente por:  
**SARAH ELISA  
BRICENO  
ARAUJO**

VILLARRUEL ALMEIDA, SANDRA VERONICA  
**Secretario Ad-hoc**



Firmado digitalmente por:  
**SANDRA VERONICA  
VILLARRUEL  
ALMEIDA**



## AUTORÍA

Yo, **Fernando Alexander Pesantez Torres**, con cédula de identidad 1401065691, declaro que las ideas, juicios, valoraciones, interpretaciones, consultas bibliográficas, definiciones y conceptualizaciones expuestas en el presente trabajo; así cómo, los procedimientos y herramientas utilizadas en la investigación, son de absoluta responsabilidad de el/la autora (a) del trabajo de integración curricular. Así mismo, me acojo a los reglamentos internos de la Universidad de Investigación de Tecnología Experimental Yachay.

Urququí, noviembre 2020.

Fernando Pesantez

Fernando Alexander Pesantez Torres

CI: 1401065691





## AUTORIZACIÓN DE PUBLICACIÓN

Yo, **Fernando Alexander Pesantez Torres**, con cédula de identidad 1401065691, cedo a la Universidad de Investigación de Tecnología Experimental Yachay, los derechos de publicación de la presente obra, sin que deba haber un reconocimiento económico por este concepto. Declaro además que el texto del presente trabajo de titulación no podrá ser cedido a ninguna empresa editorial para su publicación u otros fines, sin contar previamente con la autorización escrita de la Universidad.

Asimismo, autorizo a la Universidad que realice la digitalización y publicación de este trabajo de integración curricular en el repositorio virtual, de conformidad a lo dispuesto en el Art. 144 de la Ley Orgánica de Educación Superior

Urququí, noviembre 2020.

Fernando Pesantez

Fernando Alexander Pesantez Torres

CI: 1401065691



## **Acknowledgements**

I would like to express my gratitude to all my professors for the experience and knowledge given these last 5 years. Especially to my advisor Dr. Gema Gonzalez as well as my co-advisor Dr. Manuel Caetano for providing me proper guidance on this project as the emotional and economic help given when some obstacles and problems were presented. Moreover, I appreciate the opportunity given by Dr. Stefano Belluci for the given opportunity to work in his laboratory located in the Istituto Nazionale di Fisica Nucleare (INFN), Frascati, Italy. Besides, an acknowledge to Dr. Carlos Reinoso (Yachay Tech professor) and Dr. Antonino Cataldo (INFN) for their respective contributions in the development of this research work.

Fernando Alexander Pesantez Torres

## Resumen

En este trabajo, se doparon sistemas de nanopartículas de hidroxiapatita (HAp) con nanopartículas de ceria ( $\text{CeO}_2$ ) y/o Perclorato de Litio (partiendo de  $\text{LiClO}_4$ ) mediante ultrasonido de alta frecuencia. Además, se realizó un co-dopado con ambos compuestos. Se utilizaron dos solventes diferentes para la dispersión, los cuales fueron agua y DMF. La morfología y estructura de los sistemas nanoestructurados fueron caracterizados mediante el uso de técnicas como microscopía electrónica de barrido (SEM), microscopía electrónica de transmisión (TEM), espectroscopía infrarroja por transformada de Fourier (FTIR), espectroscopia de Raman, espectroscopía de fotoelectrones emitidos por rayos X (XPS) y difracción de rayos X (XRD). Por otro lado, las propiedades ópticas fueron estudiadas mediante el uso de espectroscopía UV-Vis y espectroscopía de fotoluminiscencia. Los resultados experimentales mostraron que efectivamente se obtuvo un dopado externo de las nanopartículas de hidroxiapatita con éxito. Una mejor dispersión se obtuvo cuando el solvente era agua. Así como una mayor respuesta luminiscente en el caso de un dopaje solo con nanopartículas de ceria. Esta propiedad es atribuida a la creación de vacancias en la estructura luego del proceso de calcinación. El análisis UV-Vis reveló que el dopaje con nanopartículas de ceria afecta la banda prohibida de energía. Esto podría estar más relacionado a la contribución de la nanoceria que la de la HAp. Estos resultados sugieren que el sistema compuesto de nanopartículas de hidroxiapatita/ceria podría tener potenciales aplicaciones, especialmente como compuesto fluorescente para propósitos de bioimagen.

**Keywords:** Nanopartículas de Hidroxiapatita, Nanopartículas de Ceria, Dopaje externo, Dopado con  $\text{Li}^+$ , Fotoluminiscencia.

### **Abstract**

In this work, hydroxyapatite (HAp) nanoparticle systems doped with ceria nanoparticles ( $\text{CeO}_2$ ) and/or Lithium Perchlorate ( $\text{LiClO}_4$ ) were synthesized using high-frequency ultrasound. In addition, a co-doping was carried out with both compounds. Two solvents were used for the dispersion: water and DMF. The morphology and structure of the nanostructured systems were characterized by using techniques such as scanning electron microscopy (SEM), transmission electron microscopy (TEM), Fourier transform infrared spectroscopy (FTIR), Raman spectroscopy, X-ray photoelectron spectroscopy (XPS) and X-ray powder diffraction (XRD). On the other hand, the optical properties were studied through the use of UV-Vis spectroscopy and photoluminescence spectroscopy. The experimental results showed that an external doping of the hydroxyapatite nanoparticles was carried out successfully. A better dispersion was obtained in water. The luminescent response was higher in the case of doping only with ceria nanoparticles due to the creation of vacancies in the structure after the calcination process. Moreover, UV-Vis analysis revealed that doping with ceria nanoparticles affects the bandgap. This could be related more to the ceria contribution than to the HAp. Therefore, these results suggest that the external ceria doped-hydroxyapatite nanoparticles system could have potential applications, especially as a fluorescent compound for bioimaging purposes.

**Keywords:** Hydroxyapatite Nanoparticles, Ceria Nanoparticles, External Doping,  $\text{Li}^+$  Doping, Photoluminescence.



# Contents

<b>List of Figures</b>	<b>iv</b>
<b>List of Tables</b>	<b>vi</b>
<b>1 Introduction</b>	<b>1</b>
1.1 Problem Statement . . . . .	2
1.2 General Objectives . . . . .	2
1.3 Specific Objectives . . . . .	2
<b>2 Theoretical Background</b>	<b>3</b>
2.1 Nanomedicine . . . . .	3
2.2 Bioimaging . . . . .	3
2.3 Hydroxyapatite . . . . .	4
2.4 Lithium Perchlorate . . . . .	5
2.5 Ceria Nanoparticles . . . . .	6
2.6 Theory of Luminescence . . . . .	7
2.6.1 Photoluminescence of Hydroxyapatite . . . . .	8
2.6.2 Photoluminescence of Ceria Nanoparticles . . . . .	9
2.7 Chemical Sonication Process . . . . .	9
2.8 State of the art . . . . .	10
2.8.1 Hydroxyapatite doped ceria systems . . . . .	10
2.8.2 Hydroxyapatite doped/substituted lithium systems . . . . .	10
2.8.3 Hydroxyapatite co-doped systems. . . . .	11
2.9 Experimental Characterization Techniques . . . . .	11
2.9.1 Scanning Electron Microscopy . . . . .	11
2.9.2 Transmission Electron Microscopy . . . . .	12
2.9.3 X-ray photoelectron spectroscopy . . . . .	13
2.9.4 Fourier-transform infrared spectroscopy (ATR) . . . . .	14

2.9.5	Raman Spectroscopy . . . . .	15
2.9.6	UV-Vis Spectroscopy . . . . .	16
2.9.7	Photoluminescence Spectroscopy . . . . .	17
2.9.8	X-Ray Powder Diffraction (XRD) . . . . .	18
<b>3</b>	<b>Methodology</b>	<b>21</b>
3.1	Experimental Part . . . . .	21
3.1.1	Reagents and solutions . . . . .	21
3.1.2	Doping of Hydroxyapatite with Lithium . . . . .	21
3.1.3	Doping of Hydroxyapatite with Ceria Nanoparticles . . . . .	21
3.1.4	Co-Doping of Hydroxyapatite with Ceria Nanoparticles and Lithium . . . . .	22
3.2	Morphological and Structural Characterization . . . . .	22
3.2.1	Scanning Electron Microscopy and EDX . . . . .	22
3.2.2	Transmission Electron Microscopy . . . . .	22
3.2.3	Fourier Transform Infrared Spectroscopy . . . . .	22
3.2.4	X-Ray Diffraction . . . . .	23
3.2.5	Diffuse Reflectance . . . . .	23
3.2.6	Raman and Photoluminescence Spectroscopy . . . . .	23
3.2.7	X-ray Photoelectron Spectroscopy . . . . .	23
<b>4</b>	<b>Results &amp; Discussion</b>	<b>25</b>
4.1	Structural and morphological characterization . . . . .	25
4.1.1	Scanning Electron Microscopy and EDX microanalysis . . . . .	25
4.1.2	Transmission Electron Microscopy . . . . .	28
4.1.3	Fourier Transform Infrared Spectroscopy and Raman Spectroscopy . . . . .	30
4.1.4	X-ray Photoelectron Spectroscopy . . . . .	34
4.1.5	X-ray Powder Diffraction . . . . .	40
4.2	Optical Characterization . . . . .	43
4.2.1	Diffuse Reflectance and Band Gap Calculations . . . . .	43
4.2.2	Photoluminescence Spectroscopy . . . . .	45
4.3	Final Discussion and Doping Model . . . . .	48
<b>5</b>	<b>Conclusions &amp; Outlook</b>	<b>51</b>
<b>A</b>	<b>EDS Results</b>	<b>53</b>
	<b>Bibliography</b>	<b>55</b>



# List of Figures

2.1	Hydroxyapatite crystal lattice. . . . .	4
2.2	HAp crystalline structure and typical ionic substitutions in carbonate apatites . . . . .	5
2.3	Ceria crystal structure . . . . .	6
2.4	Luminescence Mechanism. . . . .	7
2.5	Jablonski diagram . . . . .	8
2.6	Useful signals that are generated in SEM when a focused electron beam strikes a specimen. . . . .	12
2.7	Schematic representation of an XPS system . . . . .	14
2.8	Conceptual scheme of a multiple reflection ATR system . . . . .	15
2.9	Raman: Conceptual scheme of the light scattering processes . . . . .	16
2.10	XRD setup for powder measurements . . . . .	18
3.1	Raman Invia Renishaw Spectrometer . . . . .	23
4.1	SEM image of pure Hydroxyapatite . . . . .	25
4.2	SEM micrographs (BSE imaging) of samples with water as solvent . . . . .	26
4.3	SEM micrographs of samples with DMF as solvent. . . . .	27
4.4	EDX microanalysis spectrums . . . . .	28
4.5	TEM images . . . . .	29
4.6	FTIR spectra of uncalcined and calcined hydroxyapatite . . . . .	30
4.7	FTIR spectrums of calcined samples . . . . .	31
4.8	FTIR enlarged regions . . . . .	32
4.9	Raman spectrums of pure HAp and ceria doped-HAp . . . . .	33
4.10	XPS survey spectra . . . . .	35
4.11	Core level Ca 2p XPS spectra . . . . .	36
4.12	Core level P 2p XPS spectra . . . . .	38
4.13	Core level O 1s XPS spectra . . . . .	39
4.14	Core level Ce 3d XPS spectra . . . . .	40
4.15	XRD diffractograms of uncalcined and calcined samples . . . . .	41
4.16	XRD diffractograms of calcined HAp, doped and co-doped HAp nanocomposites. . . . .	42

4.17 Optical band gap energy estimation . . . . .	43
4.18 Photoluminescence spectra . . . . .	45
4.19 Photoluminescence spectra at two excitation wavelengths . . . . .	46
4.20 Photoluminescence spectra of calcined doped and co-doped samples . . . . .	47
4.21 Ceria doping externally hydroxyapatite model. . . . .	48

# List of Tables

4.1	FTIR band assignment of calcined pure HAp, doped HAp and co-doped HAp samples. (W) represents to water and (D) represents to DMF. In the co-doped samples the amount of LiClO <sub>4</sub> is 25% w/w respect to the HAp. . . . .	34
4.2	Core levels Binding Energies (eV) for calcined samples: HAp, doped HAp and codoped HAP. . . .	37
4.3	Reported binding energies and their assignments according to NIST Inorganic Crystal Structure Database and respective references . . . . .	37
4.4	Band Gap (eV) values of the respective HAp-doped system . . . . .	44
A.1	Measured weight percentages of HAp doped with Lithium Perchlorate (25% w/w) using water as solvent. . . . .	53
A.2	Measured weight percentages of HAp doped with ceria NPs (0.1%v/w) using DMF as solvent. . . .	53
A.3	Measured weight percentages of calcined HAp co-doped with ceria NPS (0.1% v/w) and Lithium Perchlorate (25% w/w) using DMF as solvent. . . . .	54
A.4	Measured weight percentages of calcined HAp co-doped with ceria NPs (0.1% v/w) and Lithium Perchlorate (25% w/w) using water as solvent . . . . .	54



# Chapter 1

## Introduction

Nanotechnology, in combination with biomedical developments offers the promise of revolutionary tools for drug delivery and bio diagnostic imaging<sup>1,2</sup>. So, the combination of nanomaterials and medicine can be employed as disease diagnostic tools or to deliver therapeutic agents to specific targeted sites in a controlled manner<sup>3</sup>. Hydroxyapatite (HAp) appears as a promising biomaterial to be used in this field. HAp is an inorganic compound with the formula  $\text{Ca}_{10}(\text{PO}_4)_6(\text{OH})_2$ , and represents the predominant constituent of bones and teeth in the human body<sup>4</sup>. Mineralized HAp crystal presents usually a hexagonal structure with a P63/m space group that can accept a high degree of substitutions. For instance, both  $\text{OH}^-$  and  $\text{PO}_4^{3-}$  in HAp crystal could be substituted by  $\text{CO}_3^{2-}$  resulting in the formation of A-type and B-type carbonated HAp occurring particularly in biological HAp<sup>5,6</sup>. Moreover,  $\text{Ca}^{2+}$  in HAp crystal could also be substituted by other monovalent or bivalent ions as  $\text{Li}^+$ ,  $\text{Mg}^{2+}$ ,  $\text{Fe}^{2+}$ ,  $\text{Co}^{2+}$ ,  $\text{Zn}^{2+}$ , REEs (Rare Earths) and others that comprise almost the half of the periodic table<sup>7,8,9</sup>. This versatile structure allows hydroxyapatite to improve its properties. For example, substituting HAp, can lead in enhancing from its mechanical, biological, antibacterial to luminescent properties<sup>8,9</sup>. Specifically, Lithium ions substitution results in significant enhancements in strength, toughness, bioactivity, thermal stability and osteogenesis of HAp<sup>10,11</sup>. Therefore, enhanced HAp nanoparticles (NPs) exhibiting an excellent biocompatibility, luminescent response, antibacterial or mechanical properties display promising potentials in biomedical fields, including tissue engineering scaffolds, biological probing, luminescent probing, antibacterial reagents, and drug delivery system<sup>8-12</sup>.

On the other hand, ceria nanoparticles ( $\text{CeO}_2$  NPs) have also been demonstrated to have promising applications in the biomedical field. Studies have shown the ability of ceria nanoparticles to mitigate oxidative stresses and reactive oxygen species (ROS) at the biological level due to a transformation between  $\text{Ce}^{3+}$  and  $\text{Ce}^{4+}$ <sup>13</sup>. Moreover, an excellent antibacterial activity of  $\text{CeO}_2$  NPs and cerium-doped composites has also been reported<sup>14,15</sup>. Furthermore,  $\text{CeO}_2$  NPs have been used as probing agents for fluorescent imaging and biosensors due to their excellent fluorescent properties under ultraviolet (UV) excitation<sup>16,17,18</sup>. In this work, we performed a systematic research and development of hydroxyapatite nanoparticles doped externally by  $\text{CeO}_2$  (HAp/ $\text{CeO}_2$ ) to become multifunctional nanoparticles acting as luminescent material with a low toxicological effects. Moreover, a study of the effects of doping with  $\text{Li}^+$  and ceria NPs is carried out, as well as the combination of codoping externally HAp with nanoceria and Lithium ions. Moreover,

there are few reports on the synthesis of luminescence hydroxyapatite for potential applications as bioimaging and nanomedicine. In particular, in our knowledge, there are no reports on the synthesis and characterization of ceria NPs doped and ceria NPs/Li codoped HAp via ultrasonic sonication.

## **1.1 Problem Statement**

There is a need to develop new biocompatible compounds for early diagnosis in humans, bioimaging and simultaneously drug delivery. Hydroxyapatite has been proved to be biocompatible and it has fluorescence properties. Therefore doping hydroxyapatite with some elements as ceria nanoparticles, could improve the luminescence signal, as well as the biocompatibility properties.

## **1.2 General Objectives**

Develop novel biocompatible, bioactive and non-toxic luminescent nanomaterials based on hydroxyapatite ( $\text{Ca}_{10}(\text{PO}_4)_6(\text{OH})_2$ ) doped with cerium oxide ( $\text{CeO}_2$ ) nanoparticles and lithium ions ( $\text{Li}^+$ ) for medical applications such as bio-imaging and drug delivery.

## **1.3 Specific Objectives**

1. Doping of synthesized hydroxyapatite with ceria and/or lithium, by high frequency ultrasound, using different dispersing solvents (water and DMF)
2. Study the effect of the different dopants in hydroxyapatite through a detailed structural characterization by SEM, TEM, XPS, XRD, Raman spectroscopy, FTIR, UV and photoluminescence.
3. Correlate the different results of structure and properties to understand the effect of doping on the hydroxyapatite structure.

## Chapter 2

# Theoretical Background

### 2.1 Nanomedicine

Nanomedicine is an emerging field of medicine. It can be defined as the process of diagnosis, treatment and prevention of disease and traumatic injury by applying the knowledge and tools of nanotechnology<sup>19</sup>. In short, nanomedicine is the use of nanoscale or nanostructured materials in medicine. Nanomaterials become very useful because they are similar in scale to biologic molecules and in contrast to atoms and macroscopic materials, nanomaterials have a high ratio of surface area to volume as well as tunable optical, magnetic, electronic, and biologic properties. Moreover, they can be designed to have different sizes, shapes, chemical compositions, surface chemical characteristics, and hollow or solid structures<sup>20,21</sup>. Therefore, these nanomaterials can be engineered to have various functions. Currently, these nanomaterials are being designed to have several applications within health care. For example, nanocarriers have the potential to package and protect compounds as drugs or imaging agents that are too toxic, insoluble, fragile or unstable to be delivered<sup>2</sup>. Highly luminescent nanomaterials have been developed for tracing drug delivery and as tags for identification and quantitation of small amounts of biological targets<sup>22</sup>. Applications as mentioned before as in vivo imaging, in vitro diagnostics, biomaterials, active implants and others make nanomedicine one of the most important research fields<sup>23</sup>.

### 2.2 Bioimaging

Bioimaging is a noninvasive method of visualizing biological activity processes at a specific time. It does not interfere with the various life processes such as movement, respiration, etc., and it helps to gain information on the 3-D structure of the observed specimens apart from inferencing physically. Moreover, it is useful in connecting the observation of subcellular structures and cells over tissues up to entire multicellular organisms<sup>24</sup>. Among others, bioimaging is achieved by using light, fluorescence, electrons, ultrasound, X-ray, magnetic resonance and positrons as sources for imaging. In cell biology, bioimaging can be used to follow cellular processes, quantify

ion or metabolite levels and measure interactions of molecules where they happen<sup>25</sup>. Nanomaterials have played an important role in this field during the last years, quantum dots<sup>26,27</sup>, magnetic nanoparticles<sup>28</sup>, liposomes<sup>29,30</sup>, dye-doped nanoparticles<sup>31,32</sup> and probe encapsulated by biologically localized embedding (PEBBLEs)<sup>33</sup>, have revolutionized the bio-imaging field.

## 2.3 Hydroxyapatite

Hydroxyapatite (HAp) is an inorganic compound with the formula  $\text{Ca}_{10}(\text{PO}_4)_6(\text{OH})_2$ , and represents the predominant constituent of bones and teeth in the human body<sup>4</sup>. HAp is member of the calcium phosphate salts family and it is the most stable at normal temperatures and pH between 4 and 12<sup>34</sup>. Hydroxyapatite has an atomic ratio Ca/P of 1.67, with 39% by weight of Ca, 18.5% of P and 3.38% of OH<sup>35</sup>. HAp crystallizes in a hexagonal system (see Figure 2.1) with a P63/m space group, characterized by a sixfold c-axis perpendicular to three equivalent a-axes at 120° angles to each other, where calcium cations ( $\text{Ca}^{2+}$ ) sites surrounded by negatively charged tetrahedral ( $\text{PO}_4^{3-}$ ) units and ( $\text{OH}^-$ ) ions occupy columns parallel to the hexagonal axis, where the phosphate groups network which provides the skeletal framework and gives the structure its stability<sup>35,12</sup>.

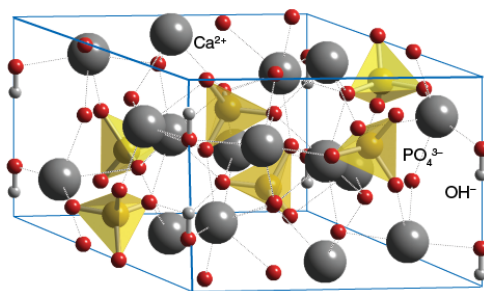


Figure 2.1: Stoichiometric hydroxyapatite crystal lattice<sup>36</sup>.

Chemical and physical properties of HAp depend on their crystallinity and its geometrical structure is important for the biomolecules adsorption by electrostatic attractions<sup>37</sup>. Due to its excellent capacity to couple with living bone tissues it is considered a material bioactive, and is used in several biomedical applications, as orthopaedics and orthodontics<sup>37</sup>. Thanks to its excellent osteoconductive characteristics, biocompatibility, bioactivity and non-toxicity, HAp is extensively used as a bioceramic in different clinical applications, such as bioceramic coating, bone tissue engineering, drug and gene delivery, and dental applications<sup>38,39,40</sup>. HAp has also been used in adsorption chromatography for many years<sup>41</sup>. Moreover, different ionic substitutions in the hydroxyapatite crystal structure ( $\text{Ca}_{10-x}\text{M}_x(\text{PO}_4)_6(\text{OH})_2$ ) can be performed in order to modify its properties<sup>39</sup>, affecting the degree of crystallinity, crystallite size, solubility, thermal stability, lattice parameters, morphology, and bioactivity of hydroxyapatite<sup>8</sup>. For example, substituting a modest quantity of  $\text{Ca}^{2+}$  ions in the hydroxyapatite structure could contribute to lattice disorder, diminish the particle size, reduce the crystallinity degree, and promote a bioresorption process. Also, luminescent properties could be induced into hydroxyapatite by replacing the calcium ( $\text{Ca}^{2+}$ ) ions with different



luminescent rare earth elements<sup>39</sup>. Furthermore, the functional groups  $\text{OH}^-$  and  $\text{PO}_4^{3-}$  in the hydroxyapatite crystal can be substituted by  $\text{CO}_3^{2-}$  resulting in the formation of A-type and B-type carbonated HAp. It occurs generally in biological HAp<sup>5,6</sup>. A typical sketch of this substitution process is shown in Figure 2.2<sup>42</sup>

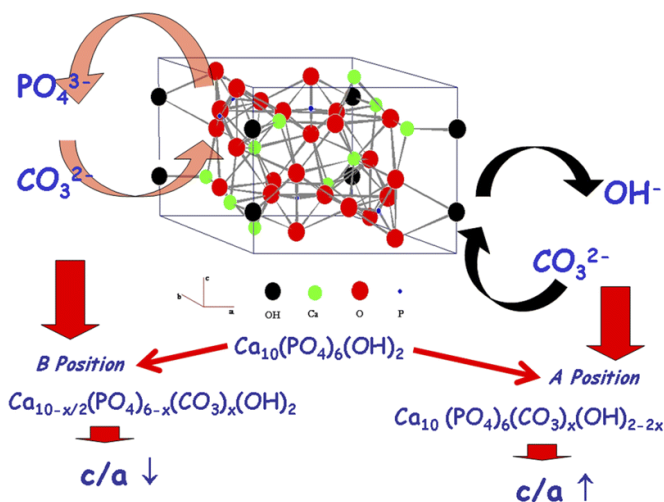


Figure 2.2: HAp crystalline structure and typical ionic substitutions in carbonate apatites taken from Vallet-Regi, M. Navarrete, D.<sup>42</sup>.

## 2.4 Lithium Perchlorate

Lithium perchlorate is a colorless crystalline or white inorganic compound with the formula  $\text{LiClO}_4$ . It presents a high solubility in many solvents and exists both in anhydrous form (widely used in the preparation of inorganic-organic electrolytes for solid state lithium batteries or as a reagent in organic synthesis) and as a trihydrate ( $\text{LiClO}_4 \cdot 3\text{H}_2\text{O}$ ) (which crystallizes non-centrosymmetrically and exhibits pyroelectric behavior)<sup>43</sup>.  $\text{LiClO}_4$  has an orthorhombic system with a space group  $\text{Pnma}$  and is the first perchlorate in the family of isotypic  $\text{MXO}_4$  type compounds<sup>43</sup>. In the crystal structure of  $\text{LiClO}_4$  the  $\text{Li}^+$  ion is surrounded octahedrally by six oxygen atoms which belong to six  $\text{ClO}_4^-$  ions. Within the  $[\text{LiO}_6]$  octahedron four short, (199 pm, 217 pm) and two long (241 pm) distances  $\text{Li}^+ - \text{O}^{2-}$  are found leading to a severe elongation of the polyhedron. This elongation also causes the quite high thermal displacement factor for the  $\text{Li}^+$  ion<sup>43</sup>. Lithium compounds are used in medical applications, organic synthesis, catalysis, absorption, air conditioning, photographic processing, and in batteries<sup>44</sup>.

## 2.5 Ceria Nanoparticles

Cerium is the most abundant and reactive rare earth metal. With an atomic number = 58, it is the first element of the lanthanide series in the periodic table. Unlike most rare earth metals that exist in a trivalent state, cerium can exist in both 3+ and 4+ states<sup>45</sup>. Therefore, we can find it as both  $\text{CeO}_2$  and  $\text{Ce}_2\text{O}_3$  in the bulk state. Cerium oxide also called ceria ( $\text{CeO}_2$ ) is a semiconductor with wide band gap energy (3.15eV) and a dielectric constant ( $\epsilon = 24.5$ )<sup>46</sup>. Although, the band gap can vary depending on the size, morphology and defects. Ceria has pale yellow appearance and crystallizes in the cubic fluorite crystal structure with space group Fm3m in which  $\text{Ce}^{4+}$  ion is surrounded by eight equivalent  $\text{O}^{2-}$  ions forming the corner of a cube, with each  $\text{O}^{2-}$  coordinated to four  $\text{Ce}^{4+}$  as shown in Figure 2.3<sup>47, 48</sup>. Ceria is characterized by its defects, those can be intrinsic or extrinsic. Intrinsic defects are presented due to thermal disorder or the surrounding atmosphere whereas the extrinsic defects are formed due to trivalent impurities<sup>49</sup>.

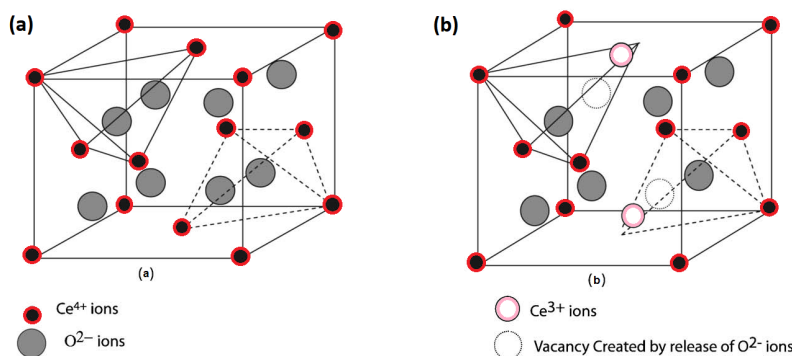


Figure 2.3: Ceria crystal structure. a)  $\text{CeO}_2$  without defects, b)  $\text{CeO}_2$  with intrinsic defects. Modified from Deshpande et al.<sup>47</sup>.

At high temperatures it releases oxygen to give a non-stoichiometric, anion deficient form that retains the fluorite lattice. This material has the formula  $\text{CeO}_{(2-x)}$ , where  $0 < x < 0.28$ . The value of  $x$  depends on both the temperature, surface termination and the oxygen partial pressure. The non-stoichiometric form presents a blue to black color, and exhibits both ionic and electronic conduction with ionic being the most significant at temperatures  $> 500^\circ\text{C}$ <sup>50, 51</sup>. These changes in the structural properties as a decrease in the lattice parameter have been reported as the conversion process of  $\text{Ce}^{4+}$  ions to  $\text{Ce}^{3+}$  ions due to the increase of the formation rate of oxygen vacancies<sup>52</sup>. When we have intrinsic defects, the coordination number of  $\text{Ce}^{4+}$  to  $\text{O}^{2-}$  reduces from eight to seven at elevated temperatures, which introduces  $\text{Ce}^{3+}$  ions into the crystal lattice as two electrons from an oxygen atom are transferred to two cerium ions neighboring the oxygen ion, which leaves the unit cell and a vacancy site is formed (Figure 2.3b). The cerium ions are reduced from the  $\text{Ce}^{4+}$  state to the  $\text{Ce}^{3+}$  state, which leads to form  $\text{Ce}^{3+}$  ions, with a  $\text{Ce} 4f^1$  configuration<sup>53</sup>. Extrinsic defects are formed when a trivalent dopant is substituted for a  $\text{Ce}^{4+}$  ion and the trivalent oxide is instantaneously converted into the trivalent ion and oxygen vacancy in the material with the oxygen atoms released from the crystal matrix. This process is shown in the following chemical reaction<sup>54</sup>,



In the past few years, the importance of ceria nanoparticles in biomedical applications is growing. Due to its dual oxidation state ceria is considered as an ideal catalyst<sup>55</sup>. Moreover, ceria has been used as gas sensor<sup>56</sup>, UV absorbents<sup>57</sup>, polishing materials<sup>58</sup>, thin-film high-K gate dielectric<sup>55</sup>, oxygen fuel cells<sup>55</sup>. Many studies have shown the ability of ceria nanoparticles to mitigate oxidative stresses and reactive oxygen species (ROS) at the biological level<sup>13</sup>. This material can act as a scavenger for excess free radicals such as superoxide ( $\text{O}_2^-$ ) and hydroxyl radical ( $\text{OH}^\cdot$ ), which are responsible for damaging the molecular structures in biological organisms and stripping electrons from cellular macromolecules<sup>52</sup>. Ceria can be used for oxygen sensing based or resistive techniques due to the conductivity of ceria is determined by the mobility and concentration of oxygen vacancies<sup>59</sup>. Several methods are related to ceria synthesis, many of those have been used to produce pure or doped ceria nanoparticles such as precipitation method, hydrothermal synthesis, microwave-assisted heating, microemulsification method, solvothermal method, sol gel method, sol gel method, ball milling, flame spray pyrolysis, reverse phase<sup>60</sup>. Compared to other methods, chemical precipitation is the most attractive due to the cheap salt precursors, simple operation, and ease of mass production<sup>61</sup>.

## 2.6 Theory of Luminescence

Luminescence may can be defined as non-equilibrium radiation that is an excess over and above the thermal radiation background and arises in the presence of intermediate processes of energy transformation between absorption and emission (the emission of photons from a material when this is stimulated by a radiation source)<sup>62</sup>. It depends on both molecular structure and chemical environment<sup>63</sup>. In general, it occurs when an electron from an excited state relaxes to a lower state, releasing energy in the form of photons.

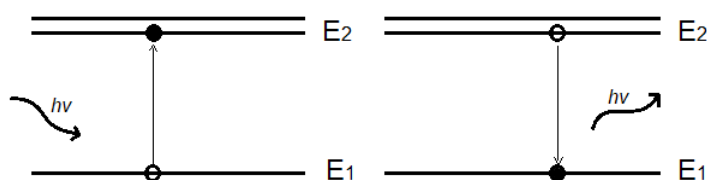


Figure 2.4: Luminescence Mechanism.

There are different types of luminescence depending on how the excitation can take place<sup>64</sup>. So, if the electron is excited by a chemical reaction, it is called chemiluminescence, if it is produced in a mechanical way, it is mechanoluminescence. When the light emission is a result of electron beam excitation it is known as cathodoluminescence. If the electron is excited by an applied electric field it is electroluminescence. If it is excited by ionizing radiation under conditions of increasing temperature, thermoluminescence (TL). Excitation by which light is produced due to the excitation by ultrasonic waves, sonoluminescence. Finally, the more general term is photoluminescence, where

the emission of the light is the result of the excitation by electromagnetic radiation, i.e., photons<sup>64</sup>. It is a simple absorption process that involved only excitation of light and the absorber, as shown in Figure 2.4, the incoming light with photon energy  $h\nu$  will excite the electrons from a ground state  $E_1$  to an upper energy level  $E_2$ , where the photon energy  $h\nu$  must be at least equal to  $E_2 - E_1$ . If the photon energy ( $h\nu$  is larger than  $E_2 - E_1$ ), the excess energy will be released as heat.

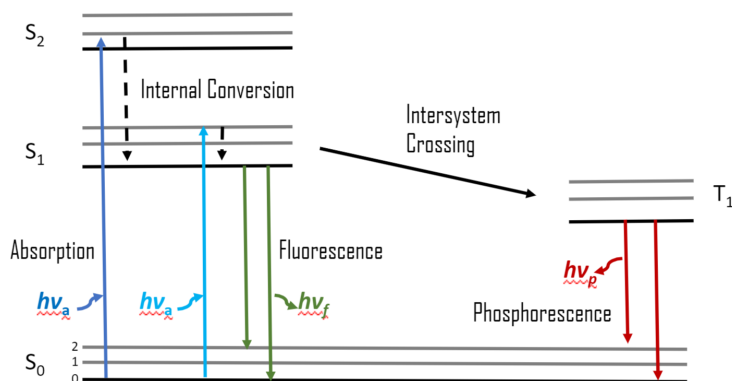


Figure 2.5: One form of Jablonski diagram. Modified from Lakowicz, J.<sup>65</sup>.

According to the duration of the response, photoluminescence can be classified as fluorescence or phosphorescence. Fluorescence takes place when the excited electrons stay in the upper energy band for a very short time before dropping to the ground level (typically, this is in the order of nanoseconds(ns)). Phosphorescence occurs when photons continue to radiate in a relatively long time after the excitation has stopped due to the fact that the excited state has an extremely long lifetime (order of milliseconds(ms))<sup>65,66,67</sup>. Schematically, these two forms of photoluminescence are shown in a Jablonski diagram, as presented in Figure 2.5.

Luminescence has different mechanisms such as charge transfer, donor-acceptor and long afterglow. Charge transfer luminescence is when transition occurs from the orbital of one ion to the orbital of another ion. In this mechanism, the nature of bond and charge distribution of the optical center can change. Donor-acceptor luminescence is when transition occurs between neutral donor and neutral acceptor. This mechanism of luminescence is exhibited in semiconductors which are doped with both p-type and n-type impurities. Long afterglow luminescence is when inside the lattice, a photo-excited ion is trapped emitting visible light after sometime<sup>68</sup>. The light emitted by the luminescent specimen will not depend on the incident radiation<sup>69</sup>.

### 2.6.1 Photoluminescence of Hydroxyapatite

Photoluminescence (PL) properties of hydroxyapatite can be attributed to its structural defects and the content of its respective constituents. According to Gonzalez, et al.<sup>70</sup>, this PL response depends on  $\text{OH}^-$  and  $\text{CO}_3^{2-}$  content and the presence of defects as the reorientation of the c-channel and impurities which are thermally activated in a temperature range of 350–450 °C. Impurities and/or defects in the lattice can be developed due to  $\text{OH}^-$  and  $\text{H}^+$  defects

have the lower energy of formation<sup>71</sup>. Other authors have studied the photoluminescence of hydroxyapatite with different approaches<sup>72,73,74</sup>. Zhang et al.<sup>72</sup> synthesized hydroxyapatite with different morphologies by controlling the pH during the synthesis process. The different samples of hydroxyapatite reported different emission intensities depending on their morphology but all samples showed a maximum centered at 428 nm. Bystrova et al.<sup>73</sup> carried out molecular modelling on photoluminescence data of samples processed with synchrotron irradiation that had been processed by different treatments: heated at temperatures between 542-546 °C under pressure, hydrogenation, microwave radiation and ionization. They obtained a PL emission peak at 420 nm with increased intensity after heating and after microwave irradiation, this was attributed to an increase in OH<sup>-</sup> vacancy defects. Finally, Machado et al.<sup>74</sup> have developed a study of the luminescence of hydroxyapatite by calcining it at different temperatures. They found maximum PL emission peaks in samples that were calcined at 350 and 400 °C which showed a broad spectrum with a maximum between 510 and 590 nm.

### 2.6.2 Photoluminescence of Ceria Nanoparticles

The rare earth ions are widely known and investigated due to their photoluminescent properties in the visible and near-infrared regions<sup>75</sup>. However, the uses of nanoceria in luminescent devices and biomedical areas have been limited due to its little luminescence compared with the other lanthanide elements. Enhancing the optical emission of nanoceria could lead to potential applications. Recent photoluminescence studies of nanoceria have shown different mechanisms through ceria nanoparticles to express their luminescent properties. It can be related with the relaxation via the 5d-4f transition of the Ce<sup>3+</sup> ions, a down conversion process, causing the conduction band electrons to make a transition to the defect state within the bandgap results in photon emission centered at 520nm, when ceria is excited with around 400 nm light, i.e., near UV-excitation<sup>16</sup>. From the defect state, the electron undergoes multiple transitions in order to return to the ground state according to Shockley Reed Hall recombination<sup>76</sup>.

Moreover, Palard, M. et al.<sup>17</sup> have reported ceria emissions peaks at 363, 378 and 400 nm, attributing the first 2 bands to charge transfer transitions between O<sup>2-</sup> and Ce<sup>4+</sup>. The remaining transitions as the system returns to the ground state are non-radiative. Thus, a large amplitude for the fluorescent intensity peak is an indication that the material contains a high concentration of Ce<sup>3+</sup> ions, which is associated with a high concentration of O<sup>-</sup> vacancies. Therefore, materials that contain a high concentration of O<sup>-</sup> vacancies and Ce<sup>3+</sup> ions should be good fluorophores. Another mechanism is reported by Deus, R. et al.<sup>77</sup> where the polycrystalline samples of ceria nanoparticles present two peaks: at 490 nm (blue-green emission) and the other at 610 nm (green emission). They linked this behavior with the structure organization level and the charge transfer occurring between oxygen and cerium ions respectively.

## 2.7 Chemical Sonication Process

This process uses ultrasound energy to agitate particles in a solution. It is usually carried out by an ultrasonic bath or a horn/probe which is also known as the sonicator. During the sonication process, the ultrasound propagates by a series of compression<sup>78</sup>. Sonication can be used for the production of nanoparticles, such as nanoemulsions, nanocrystals, liposomes and wax emulsions, as well as graphene and nanotubes dispersion<sup>79</sup>. Moreover, this technique is very

useful to perform doped systems.

## 2.8 State of the art

### 2.8.1 Hydroxyapatite doped ceria systems

The explanation for the mechanism that doping metal ion into HA is as follows: Apatites general formula is  $M_{10}(YO_4)_6X_2$  (M:  $Ca^{2+}$ ,  $Sr^{2+}$ ,  $Zn^{2+}$ , . . . ,  $YO_4$ :  $PO_4^{3-}$ ,  $VO_4^{3-}$ , .. and X: F, OH, Cl,...)<sup>80</sup>. Apatites crystallize structure have two non-equivalent sites which can be described with cations labeled M (I) and M (II). Due to this specific design, they are capable to form solid solutions and accept many substitutions. Recently, hydroxyapatite doped ceria systems have been developed for different applications. For example, an important work about hydroxyapatites as luminescent materials have also been studied by rare earth elements<sup>81,82</sup> or transition metal ions<sup>83,84</sup> this means, in principle, that they can be utilized in luminescent polymers and even in biological labeling. A new approach of hydroxyapatite doped ceria systems have shown interesting properties leading to excellent applications due in many fields. Some interesting research works have been developed through different synthesis methods of hydroxyapatite doped ceria systems. Steluta et al.<sup>85</sup> used co-precipitation method for the synthesis of stable Ce-substituted Ca hydroxyapatite (HAp) nanoparticles. This exhibited significant antibacterial activity against *Staphylococcus aureus* and *Escherichia coli* bacterial strains compared to Ce:HAp samples with  $x_{Ce} = 0$  (pure HAp). Pathai et al.<sup>86</sup> synthesized cerium-doped hydroxyapatite using an ultrasonic assisted sol-gel technique. Other results showed that  $Ce^{3+}$  and  $Ce^{4+}$  coexisted in the crystal structure of HAp where the Ce-substituted HAp samples contained  $Ce^{3+}$  within the range of 17–18%. Chaudhary et al.<sup>87</sup> describes the fabrication of cerium oxide containing hydroxyapatite (HAp) nanoparticles for environmental remediation. Li et al.<sup>88</sup> showed protective effects of  $CeO_2$  - incorporated hydroxyapatite coatings on the viability and osteogenic differentiation of  $H_2O_2$ - treated BMSCs. Wabha et al.<sup>89</sup> synthesized ceria-containing uncoated and coated hydroxyapatite-based galantamine nanocomposites for formidable treatment of Alzheimer's disease in ovariectomized albino-rat model. Huang, et al.<sup>90</sup> synthesized fluorescent HAp nanoparticles with 1%, 5%, 10% and 20% of cerium doping. This study reported that HAp NPs with content of 5% presented the high fluorescent emission peak near 380 nm at the excitation wavelength of 300 nm. They added that this fluorescent HAp NPs (specifically with 5% of cerium doping) could be used as a fluorescent probing and antioxidant agent against oxidative stress-induced cell damages. All the mentioned research works have doped HAp during its synthesis carrying out a substitution of cerium ions by calcium ions. They did not perform doping of HAp from ceria nanoparticles already synthesized, i.e., an external doping.

### 2.8.2 Hydroxyapatite doped/substituted lithium systems

Substitution/doping of hydroxyapatite with lithium (Li) results in significant enhancements in strength, toughness, bioactivity, thermal stability and osteogenesis of HAp<sup>10</sup>. The reason for the increase of strength of Li doped HAp may be due to that metal ion Li could decrease the porosity of the samples which resulted in a more compact and hard structure<sup>80</sup>. Fanovich et al.<sup>91</sup> and Valerio et al.<sup>92</sup> have determined that lithium addition forms a liquid phase

which improves the sintering process. In some biocompatibility tests lithium is described as an element that does not interfere with the hydroxyapatite biocompatibility<sup>92,93</sup>. Natural bone manifests a particular electrical pattern which is believed to have an important influence on the architecture, composition, and physiology of living osteoblasts<sup>94</sup>. It has been stated that the electromagnetic field is important to bone healing<sup>95,96</sup>. Usually inorganic phosphor hosts are incorporated with small concentrations of activator ions, transition (3d) or rare-earth (4f) metals. The absorption and emission bands of activators are controlled by changing the crystal field or covalence depending on site symmetry and coordination number of activator ions<sup>97</sup>. Therefore, lithium is used to control these parameters and for charge compensation.

### 2.8.3 Hydroxyapatite co-doped systems.

Some interesting research have carried out co-doping hydroxyapatite with different elements and these has shown an improvement on its mechanical, biological and optical properties<sup>98,99,84</sup>. Uysal, I., et al.<sup>98</sup>. have investigated co-doping of hydroxyapatite with zinc and fluoride and showed that it improves mechanical and biological properties of hydroxyapatite. Co-doping of Zn<sup>2+</sup> and F ions highly improves the density, microhardness and fracture toughness of pure HA. Zn<sup>2+</sup> incorporation to the structure resulted with an increase in cell proliferation and ALP activity of cells and further increase was observed with 1 mol% F addition. On the other hand, Ravindranadh, K., et al.<sup>99</sup> have performed structural and photoluminescence studies of Co<sup>2+</sup> doped Ca–Li hydroxyapatite nanopowders. However, hydroxyapatite co-doped with lithium ions and ceria nanoparticles have not still been studied.

## 2.9 Experimental Characterization Techniques

### 2.9.1 Scanning Electron Microscopy

Scanning Electron Microscopy (SEM) is a technique that creates images of a sample by scanning the surface with a focused beam of electrons. SEM combines high-resolution imaging with a large depth of field, because of short wavelengths of electrons and their ability to be focused using electrostatic and electromagnetic lenses. The electrons in the beam interact with the sample, this strong interaction of electrons with matter creates a wide assortment of useful signals that contain important information about the surface topography and composition. When primary electrons strike a sample surface, a wide range of useful interactions can be produced, causing various charged particles and photons to be generated. Those are emitted, collected and used to form an image or a chemical spectrum. Typical signals that are created are shown schematically in Figure 2.6<sup>100</sup>.

In SEM, the principal electron signals that are used are backscattered electrons (BSEs) and secondary electrons (SEs). The generation, transport and escape of these signals can be affected by the differences in composition and surface topography of the specimen and the beam energy. With the increased atomic number of the specimen, the volume and depth of the electron penetration decrease because the number of particles in the specimen increases, stopping the penetration of electrons. However, with the increase of the beam energy, the volume and depth of the penetration increases<sup>100</sup>.

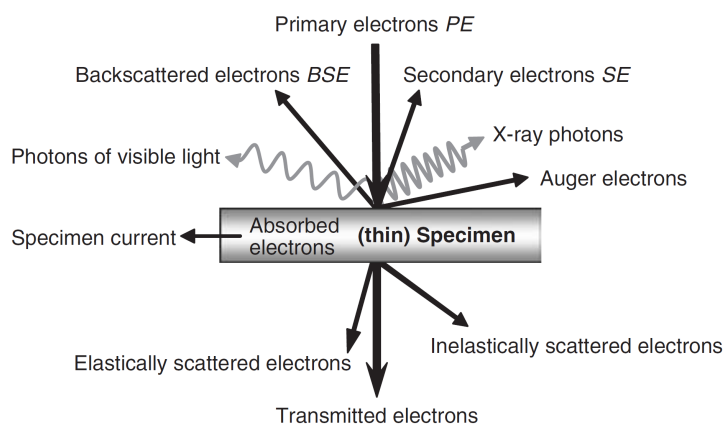


Figure 2.6: Useful signals that are generated when a focused electron beam strikes a specimen. Transmitted electrons can result in a thin sample. Sketch taken from Stokes, D.<sup>100</sup>.

Basically, BSEs are used to give composition information about features that are deep beneath the surface. They also provide topographic information, however, this information differs from secondary electrons because some backscattered electrons are blocked by regions of the specimen. On the other hand, we have the SEs that are characterized for given information about the topography. Mainly, these are used principally to visualize the texture and roughness and surface microstructure of the specimen<sup>101</sup>.

Usually SEM microscopes are equipped for energy-dispersive X-ray spectroscopy (EDX). So, the characteristic X-rays that are produced by the interactions of the electrons with the sample can give us important information about the chemical composition of the specimen (abundance of elements in the sample), since the energies of X-rays are unique of the difference between two shells of the atomic structure of the specific emitting element. Generally, when X-rays hit the sample, it may excite an electron in an inner shell, ejecting it from the shell while creating an electron hole where the electron was. An electron from an outer, higher-energy shell then fills the hole, and the difference in energy between the higher-energy shell and the lower energy shell may be released in the form of an X-ray. The number and energy of the X-rays emitted from a specimen can be measured by an energy-dispersive spectrometer<sup>102</sup>.

## 2.9.2 Transmission Electron Microscopy

Transmission electron microscopy (TEM), is a microscopy technique considered as the central tool for complete characterization of nanoscale materials and devices. The transmission electron microscope is composed mainly by an electron source, a system of objective lenses, a setup of magnifying lenses, a sample holder and data collector. Basically, an electron beam of uniform current is transmitted through a thin specimen, due to this interaction of electrons with the specimen an image is formed. These electrons are emitted from an electron gun by thermionic, Schottky or field emission. Electrons interact strongly with the atoms by elastic and inelastic scattering. Thus, the sample must be very thin, typically in the order of a few nanometers, depending on the density and elemental



composition of the specimen and the resolution desired. The image is magnified and focused onto an imaging device, such as a fluorescent screen, a layer of photographic film, or a sensor such as a scintillator attached to a charge-coupled device<sup>103</sup>.

In conclusion, TEM gives information about the morphology of the sample, crystalline structure and chemical composition. The main advantages of TEM are images of high resolution, electron diffraction analysis, and elemental microanalysis when the equipment has an energy dispersive spectroscopy (EDS) or an electron energy loss spectrometer. Special preparation techniques are used for this; electropolishing and electron-ion in materials science and ultramicrotomy of stained and embedded tissues or cryofixation in the biological sciences<sup>104</sup>. TEM can provide high resolution because elastic interaction is an interaction that is highly localized to the region occupied by the screened Coulomb potential of an atomic nucleus.

### 2.9.3 X-ray photoelectron spectroscopy

X-ray photoelectron spectroscopy (XPS) is a surface-sensitive quantitative spectroscopic technique that gives important information about the elemental composition, empirical formula, chemical state and electronic state of the elements present in the material. XPS is a useful measurement technique because it not only shows what elements are within a film but also what other elements they are bonded to. This means if you have a metal oxide and you want to know if the metal is in a +1 or +2 state, using XPS will allow you to find that ratio. Quantitative data can be obtained from peak heights or peaks areas, and identification of chemical states often can be made from exact measurement of peak positions and separations, as well as from certain positions and separations, as well as from certain spectral features. Moreover, it has a good sensitivity (concentrations down to 0.1 atomic %) and needs relative ease and minimal sample preparation<sup>105</sup>. As XPS is a surface spectroscopic technique, at most the instrument will only probe 10 nm into a sample.

Surface analysis by XPS is accomplished by irradiating a solid in vacuum with monoenergetic soft X-rays and analyzing the energy of the detected electrons. Mg  $K\alpha$  (1253.6 eV) or Al  $\alpha$  (1486.6eV) X-rays are usually used. They interact with atoms in the surface region, causing electrons to be emitted by the photoelectric effect<sup>106</sup>. Generally, a 3-step process takes place. In the first step, a photon is absorbed by the atom based in differential photo-electric cross sections ( $d\sigma/d\Omega$ ) and an electron is excited. In the second step, the photo-electron travels with non-relativistic kinetic energy ( $KE$ ) through the sample to the surface and it is not scattered. And, in the third step, the electron escapes into vacuum through the surface energy barrier ( $\Phi, \phi_s$ ), due to the photo-electron  $KE$  is higher than the spectrometer work function ( $\phi_s$ ). So, electrons that enter to the the collection lens will be analyzed<sup>107</sup>. The emitted electrons have measured kinetic energies given by<sup>106</sup>:

$$KE = h\nu - BE - \phi_s \quad (2.2)$$

Where  $h\nu$  is the energy of the photon and  $BE$  is the binding energy of the atomic orbital from which the electron originates. The binding energy may be regarded as the difference between the initial and final states after the photo-electron has left the atom. Because there is a variety of possible final states of ions from each type of atom, there is a corresponding variety of kinetic energies of the emitted electrons. Moreover, there is a different probability

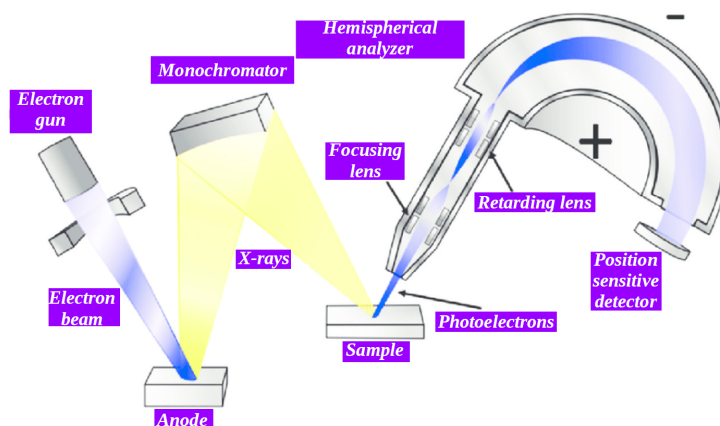


Figure 2.7: Schematic representation of an XPS system<sup>108</sup>.

or cross-section for each final state<sup>106</sup>. A schematic representation of an XPS system is shown in figure 2.7<sup>108</sup>. Here, we can observe an electron gun that hits an anode, generating X-rays that then go to a monochromator to finally reach the sample's surface. Subsequently, photoelectrons pass through an hemispherical analyzer. After that, only electrons within a narrow range of energies arrive at the detector.

#### 2.9.4 Fourier-transform infrared spectroscopy (ATR)

Infrared Spectroscopy is the study of the interaction of infrared light with matter. It probes the molecular vibrations. Functional groups can be associated with characteristic infrared absorption bands, which correspond to the fundamental vibrations of the functional groups. IR absorption arises from a direct resonance between the frequency of a particular normal mode of vibration. Basically, Fourier-transform infrared spectroscopy (FTIR) is a vibrational technique used to obtain an infrared spectrum of absorption or emission of a solid, liquid or gas. An FTIR spectrometer simultaneously collects high-spectral-resolution data over a wide spectral range. This confers a significant advantage over a dispersive spectrometer, which measures intensity over a narrow range of wavelengths at a time. Typically, a FTIR spectrum is between 400 to 4000  $\text{cm}^{-1}$ <sup>109</sup>. Spectral bands in vibrational spectra are molecule specific and provide direct information about the biochemical composition. FTIR peaks are relatively narrow, and in many cases can be associated with the vibration of a particular chemical bond (or a single functional group) in the molecule. There are some FTIR sample handling techniques such as attenuated total reflection (ATR), diffuse reflectance (DRIFTS), true specular reflectance/reflection-absorption and transmission.

Thanks to the development of attenuated total reflection (ATR), measurement of the infrared spectra of many types of samples has become quite routine. ATR is a technique whereby the sample is placed in contact with a sensing element, and a spectrum is recorded as a result of that contact. Unlike many other sampling techniques, radiation is not transmitted through the sample. Moreover, samples can be measured in their neat state, not requiring dilution to record the spectrum<sup>110</sup>. An ATR accessory operates by measuring the changes that occur in a totally

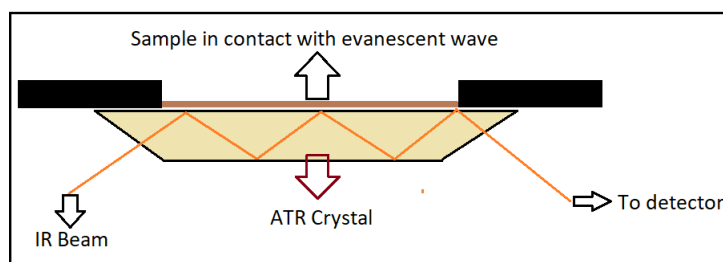


Figure 2.8: Conceptual scheme of a multiple reflection ATR system. Modified sketch from Perkin Elmer<sup>111</sup>.

internally reflected infrared (IR) beam when the beam comes into contact with a sample. An IR beam is directed onto an optically dense crystal with a high refractive index at a certain angle. This internal reflectance creates an evanescent wave that extends beyond the surface of the crystal into the sample held in contact with the crystal. We can observe this working system in Figure 2.8. It can be easier to think of this evanescent wave as a bubble of infrared that sits on the surface of the crystal. This evanescent wave protrudes only a few microns ( $0.5\mu-5\mu$ ) beyond the crystal surface and into the sample. Consequently, there must be good contact between the sample and the crystal surface. In regions of the IR spectrum where the sample absorbs energy, the evanescent wave will be attenuated or altered. The attenuated energy from each evanescent wave is passed back to the IR beam, which then exits the opposite end of the crystal and is passed to the detector in the IR spectrometer. The detector records the attenuated IR beam as an interferogram signal, which can then be used to generate an IR spectrum<sup>111</sup>.

### 2.9.5 Raman Spectroscopy

Raman spectroscopy is a non-destructive spectroscopic technique typically used to determine vibrational modes of molecules, although rotational and other low-frequency modes of systems may also be observed<sup>112</sup>. Raman spectroscopy is commonly used in chemistry to provide a structural fingerprint by which molecules can be identified. It provides detailed information about the molecular structure, because each vibration of atoms shows a characteristic position and intensity. Both position and intensity are influenced by the chemical environment, or in other words by chemical bonds, inter- and intramolecular forces<sup>113</sup>. When light interacts with matter, the photons which make up the light may be absorbed or scattered or may pass straight through it. In a scattering process, the light interacts with the molecule and polarizes the cloud of electrons round the nuclei to form a short-lived state called quickly reradiated<sup>114</sup>. It results in elastic (Rayleigh scattering) and inelastic scattering or Raman scattering. Figure 2.9 shows the basic processes which occur for one vibration. Virtual states are created when the laser interacts with the electrons and causes polarization and the energy of these states is determined by the frequency of the light source used. The Rayleigh process (Figure 2.9a) becomes the most intense process since most photons scatter this way. It does not involve any energy change, so, as can be observed in the diagram, the light returns to the same energy state. Raman scattering is an inelastic scattering process, which means that it can lead in the increase or decrease of the kinetic energy of the photon during interaction. When this process occurs from the ground vibrational state

m, it leads to absorption of energy by the molecule and its promotion to the higher energy excited vibrational state n. This is called Stokes scattering and a scheme is shown in Figure 2.9b. However, some molecules can be present initially in an excited vibrational level (represented as n in Figure 2.9) due to thermal energy. Therefore, the radiated line energy is the sum of the pre-excitation energy and the energy absorbed by the molecule. Scattering from this excited state to the ground state m is called anti-Stokes scattering as shown in Figure 2.9c<sup>114</sup>.

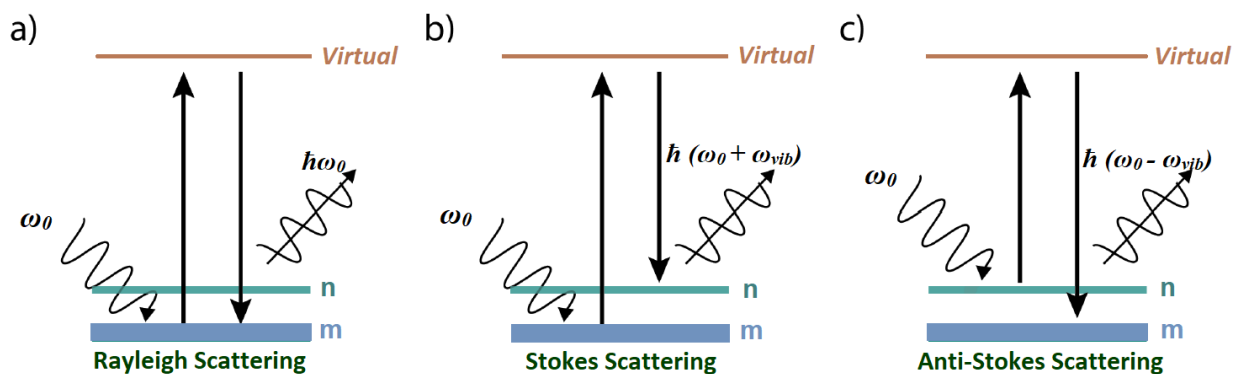


Figure 2.9: Diagram of the Rayleigh and Raman scattering processes.: a) Rayleigh scattering, b) Raman Stokes scattering and c) Raman anti-Stokes scattering, m represents the lowest energy vibrational state and n represents the excited vibrational level of ground state.

Typically, in a Raman microscope, a sample is illuminated with a laser beam. Electromagnetic radiation from the illuminated spot is collected with a lens and sent through a monochromator. Elastic scattered radiation at the wavelength corresponding to the laser line (Rayleigh scattering) is filtered out by either a notch filter, edge pass filter, or a band pass filter, while the rest of the collected light is dispersed onto a detector.

### 2.9.6 UV-Vis Spectroscopy

UV-Vis Spectroscopy refers to absorption or reflectance spectroscopy in part of the ultraviolet and the full, adjacent visible spectral regions. This means it uses light in the visible and adjacent (near-UV and near-infrared (NIR)) ranges. The absorption or reflectance in the visible range directly affects the perceived color of the chemicals involved. In this region of the electromagnetic spectrum, molecules undergo electronic transitions<sup>115</sup>. So, it is used to measure the reflection, transmission and absorption as a function of wavelength or angle of incidence. A specific technique is called diffuse reflectance, it occurs when light impacts on the surface of a material and is partially reflected and transmitted. Basically, it is a reflection of the light in all directions of small interfaces on an irregular surface, where the interfaces formed by small surfaces oriented at all possible angles can be considered. The detected light can be a combination of the reflected and emitted components<sup>116</sup>.

Typically, photons hit the sample (molecules), then, this energy is absorbed by the molecule causing an electron excitation from ground state to a more excited energetic state. UV-visible light has enough energy to promote

electrons to a higher electronic state, from the highest occupied molecular orbital (HOMO) to the lowest unoccupied molecular orbital (LUMO). The energy difference between the HOMO and the LUMO is called the band gap. A spectrometer records the sample absorption at different wavelengths.

### Absorption coefficient and direct band calculations

The absorption coefficient  $\alpha$  is defined as the relative rate of decrease in light intensity  $L(h)$  along its propagation path [14]

$$\alpha' = \left(\frac{1}{L(h\nu)}\right)\left(\frac{d[L(h\nu)]}{dx}\right) \quad (2.3)$$

where  $\alpha$  is expressed in units of  $\text{cm}^{-1}$ . The absorption coefficient for a given photon energy  $h$  is proportional to the probability for the transition from the initial state to the final state of an atom, ion, molecule, or crystal, where the difference in energy between the initial and final state is equal to the photon energy plus or minus the energy of any other particle (e.g., a phonon) that is involved in the transition, and also the density of available final states. When reflectance diffuse is performed, this coefficient can be approximated by using Kubelka-Munk model<sup>117</sup>. The Kubelka–Munk method is based on the following equation:

$$F(R) = 1 - \frac{R}{2R} \quad (2.4)$$

where  $R$  is the reflectance;  $F(R)$  is proportional to the absorption coefficient ( $\alpha$ ). This equation is usually applied to highly light scattering materials and absorbing particles in a matrix<sup>118</sup>. From  $F(R)$ , the optical band gap energy can be evaluated using the Tauc equation<sup>119</sup>. According to this equation, photon energy ( $h\nu$ ) is related to the optical band gap energy  $E_g$  of a semiconductor  $\alpha h\nu$  by the following relationship[24]:

$$\alpha(h\nu) = A * (h\nu - E_g)^\gamma \quad (2.5)$$

Where  $A$  is a constant for any given material and  $E_g$  the energy band gap. The exponent ( $\gamma$ ) depends on the electronic transition type. If  $\gamma = 1/2, 2, 3$  or  $3/2$  represents an indirect allowed transition, direct forbidden transition and indirect forbidden transition, respectively<sup>120</sup>. Plotting  $[F(R)h\nu]^{1/2}$  vs  $h\nu$ , the intersection with x-axis gives the value of direct allowed band gap,  $E_g$ .

### 2.9.7 Photoluminescence Spectroscopy

Photoluminescence spectroscopy is a widely contactless, nondestructive technique used for characterization of the optical and electronic properties of semiconductors and molecules. In chemistry, it is more often referred to as fluorescence spectroscopy, but the instrumentation is the same. Light is directed onto a sample, where it is absorbed and imparts excess energy into the material in a process called photo-excitation. One way this excess energy can be dissipated by the sample is through the emission of light, or luminescence. In the case of photo-excitation, this luminescence is called photoluminescence<sup>121</sup>. It provides information to determine the band gap, purity, crystal

quality, levels of impurity defects of the semiconductor material and to understand the underlying physics of the recombination mechanism<sup>122</sup>.

The Photoluminescence principle consists of hitting the sample with photons from a source of excitation that are sufficiently energetic to excite the electrons and activate the PL<sup>123</sup>. Sample absorbs energy in the form of photons and leads the electrons to an excited state. When these electrons return to the ground state, in certain materials, the excess energy is released in the form of photons. This emission is collected on the computer using an optical fiber from the spectroscopy. As a result, an intensity curve in arbitrary units (a.u.) as a function of the wavelength is displayed as a spectrum<sup>124</sup>.

### 2.9.8 X-Ray Powder Diffraction (XRD)

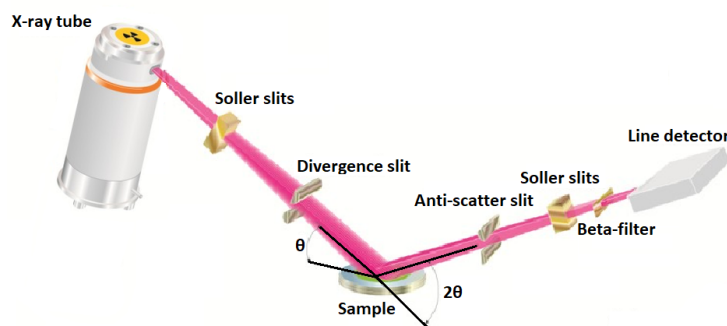


Figure 2.10: XRD setup for powder measurements. Modified figure from Konig et al.<sup>125</sup>.

X-ray powder diffraction (XRD) is a non-destructive analytical technique primarily used for analyzing crystalline materials. It provides detailed information about the crystallographic structure, chemical composition, and physical properties of materials. It provides detailed information about the crystallographic structure, chemical composition, and other structural parameters of a material, such as average grain size, crystallinity, strain and crystal defects. XRD is based on Bragg's law ( $n\lambda = 2d\sin\theta$ ). Where,  $d$  is the interplanar distance,  $n$  is a positive integer and  $\lambda$  is the wavelength of the incident wave. Using this equation, it is possible to calculate lattice parameters<sup>126</sup>. Basically, according to this law when electromagnetic radiation are incident upon a crystalline sample, it would produce a Bragg peak if their reflections off the various planes interfered constructively. So, the respective diffraction peaks are produced by constructive interference of an incident monochromatic beam of X-rays that is scattered at specific angles from different set of lattice planes present in the material. The peak intensities are determined by the atomic positions within the lattice planes. Consequently, the XRD pattern is the fingerprint of periodic atomic arrangements in a given material. A standard database available online for X-ray powder diffraction patterns allows quick phase identification of crystalline samples<sup>127</sup>. Peaks can be either broad or sharp. Broad peaks are produced by amorphous regions of the samples, whereas sharp peaks are produced by crystalline regions<sup>126</sup>.

Generally, X-ray diffractogram of the sample is recorded on an X-ray diffractometer operating at known voltages

and current using a Cu K $\alpha$  X-rays ( $\lambda = 0.15406$  nm) over the  $2\theta$  range from 10 to 100 degrees in the steps of 0.01 degree at room temperature in open quartz sample holders<sup>126</sup>. A XRD setup for powder measurements can be observed in Figure 2.10<sup>125</sup>. It consists of an X-ray source, a spinning sample stage, a high speed linear detector and several optics for optimizing the quality of the data output.





# Chapter 3

## Methodology

Here, it is provided a description of reagents, preparation of solutions, doping and conditions of experiments, as well as the equipment used to achieve the objectives established.

### 3.1 Experimental Part

#### 3.1.1 Reagents and solutions

Two solvents were used, distilled water (DI) and dimethylformamide, DMF ((CH<sub>2</sub>)<sub>2</sub>NCH). Lithium perchlorate (LiClO<sub>4</sub>) was received as a white crystalline salt from Sigma-Aldrich, Commercial carbonated hydroxyapatite (HAp) obtained from Sudeep Pharma, India. Finally, we use a commercial ceria nanoparticles NANO4K-3812 in aromatic-free white spirit, with a size of ~ 10nm obtained from BYK-Chemie GmbH, Germany.

#### 3.1.2 Doping of Hydroxyapatite with Lithium

Hydroxyapatite was doped using the sonication method (High ultrasound). An amount of hydroxyapatite was mixed with Lithium Perchlorate at 10% (w/w) and 25% (w/w). Then, 40 ml of DI water was added and a sonication process was carried out for 10 minutes . After that, the samples were dried at 70 °C. Finally, the resulting samples were calcined in an oven at 400 Celsius degrees for 1 hour.

#### 3.1.3 Doping of Hydroxyapatite with Ceria Nanoparticles

An amount of hydroxyapatite was placed in a precipitated glass. Then a suspension of ceria nanoparticles in aromatic-free white spirit was added at (0.03% and 0.1%) v/w respect to the amount of hydroxyapatite. Then, 40 ml of DI water was added and a sonication process was carried out for 20 minutes. Finally, the samples were dried at 70 °C. Finally, the resulting samples were calcined in an oven at 400 °C for 1 hour. The same process was carried out using DMF instead water as solvent.

### 3.1.4 Co-Doping of Hydroxyapatite with Ceria Nanoparticles and Lithium

An amount of hydroxyapatite was mixed with Lithium Perchlorate at 25% (w/w). Then a suspension of ceria nanoparticles was added at (0.03% and 0.1%) v/w respect to the amount of hydroxyapatite. Then, 40 ml of DI water was added and a sonication process was carried out for 20 minutes. Finally, the samples were dried at 70 °C. Finally, the resulting samples were calcined in an oven at 400 °C for 1 hour. The same process was carried out using DMF instead water as solvent.

## 3.2 Morphological and Structural Characterization

Pristine and calcined samples were characterized by X-Ray powder diffraction (XRD), Raman spectroscopy, Fourier transform infrared spectroscopy (FTIR) using the ATR sample technique, X-ray photoelectron spectroscopy (XPS) and energy-dispersive X-ray spectroscopy (EDAX). Morphological analysis was carried out by SEM and TEM. Optical analysis was carried out using UV-Vis spectroscopy and photoluminescence spectroscopy.

### 3.2.1 Scanning Electron Microscopy and EDX

The microstructural analysis was carried out in a TESCAN MIRA 3 Schottky field electron microscope, working with an acceleration voltage of 10 KV attached with an energy dispersive X-ray microanalysis (EDS Bruker Quantax). The samples were suspended in a solution water/ethanol and then these were shaken for 5 minutes. Then the samples were placed in a SEM grid. (Sample coating was not needed)

### 3.2.2 Transmission Electron Microscopy

Transmission electron microscopy (TEM) analysis was carried out in a Tecnai transmission electron microscope at an acceleration voltage of 200 kV. The samples were suspended by adding 1:1 ml of ethanol/water 70% in a vial with a tiny amount of sample. This suspension was sonicated for 10 minutes, and a drop of this suspension was placed in the TEM grid.

### 3.2.3 Fourier Transform Infrared Spectroscopy

The functional groups of hydroxyapatite, ceria and lithium doped-HAp systems were characterized by using Fourier transform infrared spectroscopy (FTIR), with the ATR sampling technique. The spectroscopy spectrums were recorded using an Agilent Cary 630 FTIR spectrometer FT-IR (Diamond ATR) in the range of 4000–600  $\text{cm}^{-1}$ , with a spectra resolution  $< 2 \text{ cm}^{-1}$ . The data of the samples were acquired in the absorbance mode at room temperature to probe the vibrational spectra of the samples

### 3.2.4 X-Ray Diffraction

The crystalline structure of the different systems was studied by X-ray powder diffraction (XRD). The powder diffractometer used in this characterization was a Mini-flex-600, from Rigaku, with a D/tex Ultra 2 detector. The measurement conditions were 40 kV and 15 mA for the X-ray generator in a sealed tube using Cu  $K\alpha$  radiation ( $\lambda = 1.5418 \text{ \AA}$ ). For collecting data, the selected angular region was  $2\theta = 5^\circ\text{-}90^\circ$  with a step width of  $0.005^\circ$ . Powder samples were placed on a glass and aluminium sample holder.

### 3.2.5 Diffuse Reflectance

Optical properties (diffuse reflectance) of the respective samples were determined by using a UV-Vis Spectrometer Model Lambda 1050 from Perkin Elmer and an accessory praying mantis. Using the program UV-WinLab, each respective diffuse reflectance data was collected. Powder samples were put in the sample holder with the help of a support. Then, the UV/Vis spectra of films were recorded in the range from 400 to 700 nm. The absorbance coefficients were obtained using Kubelka Munk approximations and the band gap was calculated using the Tauc equation. The respective calculations were performed using a script in the programming language R. Moreover, the reflectance data was smoothed using an adaptive polynomial filter (ADPF).

### 3.2.6 Raman and Photoluminescence Spectroscopy

The Raman and photoluminescence spectra were recorded on a Raman Invia Renishaw Spectrometer (see Fig. 3.1) with a motorized stage able to move up to 100nm in xy-plane. These measurements were performed with an excitation wavelength of 532nm and 633 nm. Each powder sample was deposited as a thin film onto a glass slide to be analyzed. Each sample was recorded with an integration time of 5 seconds.

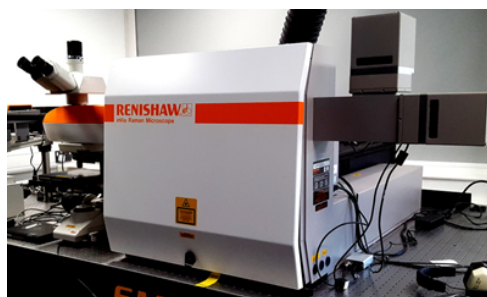


Figure 3.1: Raman Invia Renishaw Spectrometer

### 3.2.7 X-ray Photoelectron Spectroscopy

X-ray photoelectron spectroscopy analysis was performed to get chemical information of the samples. For these measurements a PHI VersaProbe III from Physical Electronics equipped with a 180 hemispherical electron energy

analyzer were used. The source was a monochromatized Al  $K\alpha$  source with 1486.6 eV of energy, operated with an energy band pass 255 kV for the survey acquisition and 55 kV for high resolution log. Sample spot had a diameter of 100  $\mu\text{m}$  and the detection angle relative to the substrate surface was 45°. The binding energy (BE) scale is calibrated by measuring reference C 1s peaks (BE: 284.8 eV) from the surface contamination. The accuracy of the measured BE is 0.1 eV. For the sample preparation, each powder sample was dusted onto a polymeric-based adhesive tape that was holded in a metallic mesh. High resolution deconvolution was performed using Tougaard background subtractions, and Voigtian and Gaussian functions. The software used for these purpose was Origin-Pro 2018.

## Chapter 4

# Results & Discussion

### 4.1 Structural and morphological characterization

#### 4.1.1 Scanning Electron Microscopy and EDX microanalysis

The resultant surface morphologies and chemical composition of the bare hydroxyapatite (HAp) and HAp doped with different concentrations of  $\text{LiClO}_4$  and ceria ( $\text{CeO}_2$ ) were investigated by SEM, EDS and TEM analysis. SEM micrographs at different magnifications are presented in Figure 4.1, 4.2 and 4.3.

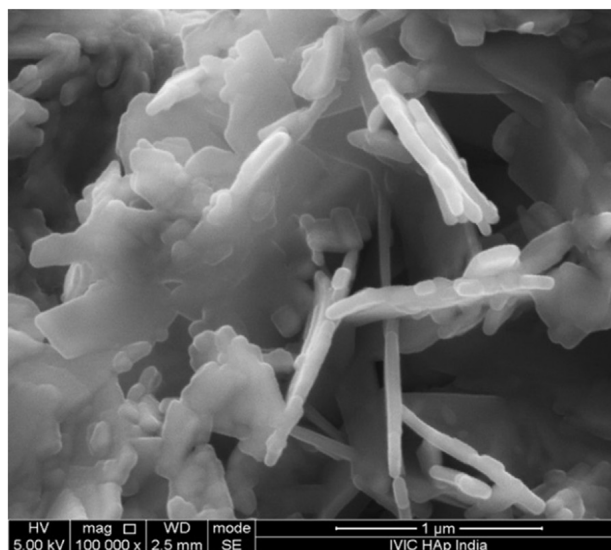


Figure 4.1: SEM image of pure Hydroxyapatite

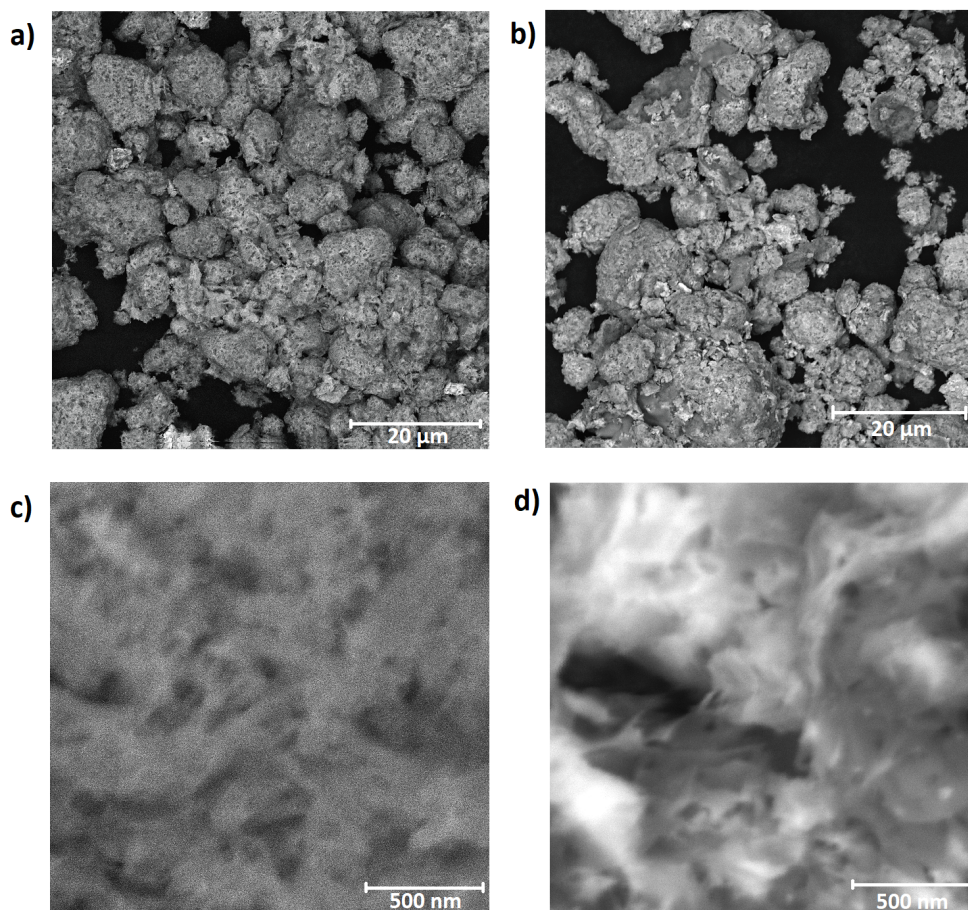


Figure 4.2: SEM micrographs (BSE imaging) of samples with water as solvent. a,c) BSE images of hydroxyapatite doped with ceria NPs (0.1% v/w), b,d) BSE images of hydroxyapatite co-doped with lithium (25% w/w) and ceria NPs (0.1% v/w)

Bare hydroxyapatite (Figure 4.1) shows plate-like particles with an average particle thickness of  $60 \pm 4$  nm and  $1 \pm 0.2$  μm wide. When hydroxyapatite is doped with ceria nanoparticles (0.1%) (figure 4.2a,c) and HAp co-doped with  $\text{LiClO}_4$  (25%) and ceria nanoparticles (0.1%), (figure 4.2b,d) in the presence of water, particle agglomerates are observed, the formation of agglomerates is attributed to the ultrasonic treatment during doping. SEM images reveal that the samples comprise many crystal agglomerates with an irregular morphology. Also, these micrographs indicate that both compounds, ceria and lithium were well dispersed on the hydroxyapatite nanoparticles. The brighter regions in the micrographs correspond to ceria nanoparticles. Since these are backscattered electron images and the atomic number of cerium is higher than the components of the hydroxyapatite. When we observe the same doped systems (figure 4.3) but by using DMF solvent. Agglomeration of hydroxyapatite plates with irregular

morphologies can be observed. Even though these systems show a good distribution of ceria, the presence of some agglomerations can be observed, as can be seen in figure 4.3a and figure 4.3b (brighter spots). As we said in the methodology section (3.1.1), a hydrocarbon solvent (aromatic-free white spirits) is the carrier of ceria nanoparticles. Therefore, this agglomeration of ceria nanoparticles can be related with the solubility of both solvents in non-polar solvents as hydrocarbons. A hydrocarbon solvent is insoluble in water but it is partially miscible with DMF<sup>128</sup>. So, when water is used, colloids are formed. However, the high ultrasound treatment break these colloids allowing an almost uniform dispersion of ceria nanoparticles. On the other hand, when DMF is used, it is partially miscible with the ceria nanoparticles carrier, leading to the formation of small agglomerates of CeO<sub>2</sub> NPs.

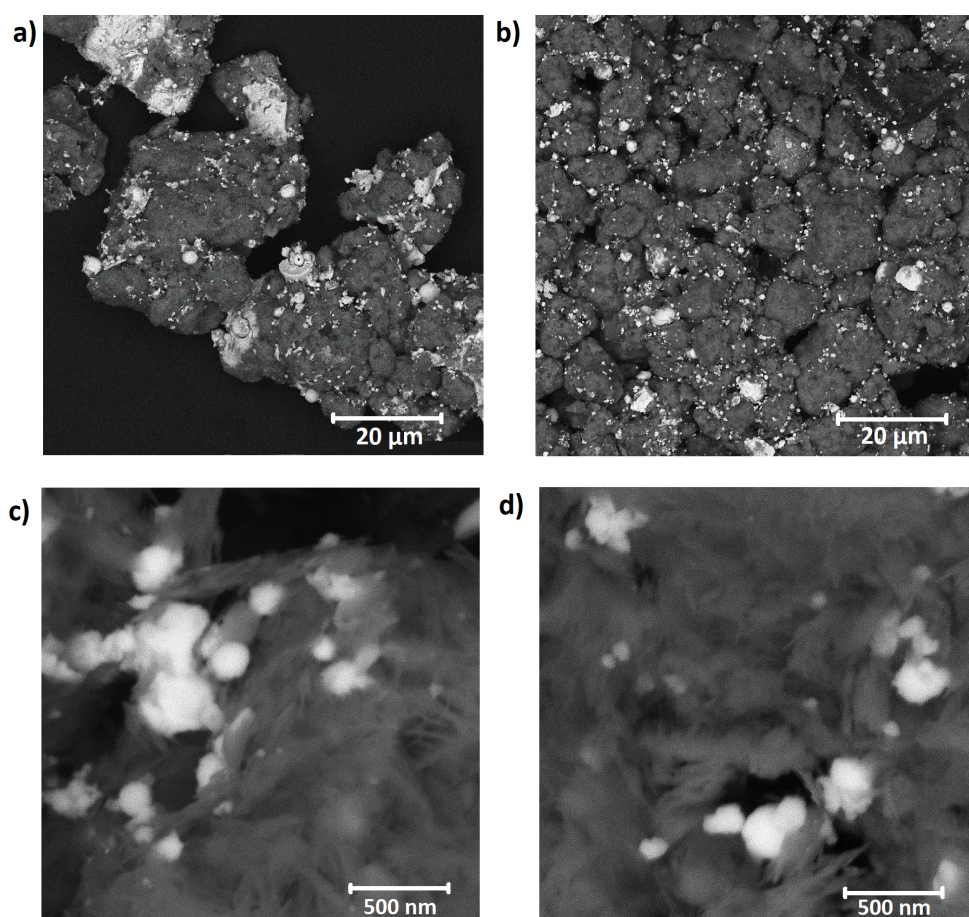


Figure 4.3: SEM micrographs (BSE imaging) of samples with DMF as solvent. a) Hydroxyapatite doped with ceria NPs (0.1% v/w), b) Hydroxyapatite co-doped with lithium (25% w/w) and ceria NPs (0.1% v/w)

The EDX spectra of the studied powders (figure 4.4) confirms the presence of the hydroxyapatite constituents (calcium (Ca), phosphorous (P), oxygen (O), carbon (C)) as cerium (Ce) in the respective nanopowders. Because of

the limitation of the EDS instrument, the Lithium and Hydrogen elements cannot be observed in the EDS spectra<sup>129</sup>. Therefore, in the doped HAp/LiClO<sub>4</sub> sample spectra (figure 4.4a) can only be observed in the hydroxyapatite constituents; Ca, P, O and C. The main carbon signal comes from the carbon support in the sample holder. Also, it is possible to detect the presence of a small Chlorine (Cl) contribution, showing that this element was not completely eliminated and constitutes part of the new composite but in a low percentage. Finally, Ca, P and Ce can be identified from the HAp/CeO<sub>2</sub> sample spectra (figure 4.4b) and Ca, P, Ce and Cl from the co-doped (HAp/LiClO<sub>4</sub>/CeO<sub>2</sub>) samples spectra (figure 4.4c, d). The obtained percentages of the different elements present in the samples are shown in Appendix A (Table A.1, A.2, A.3 and A.4)

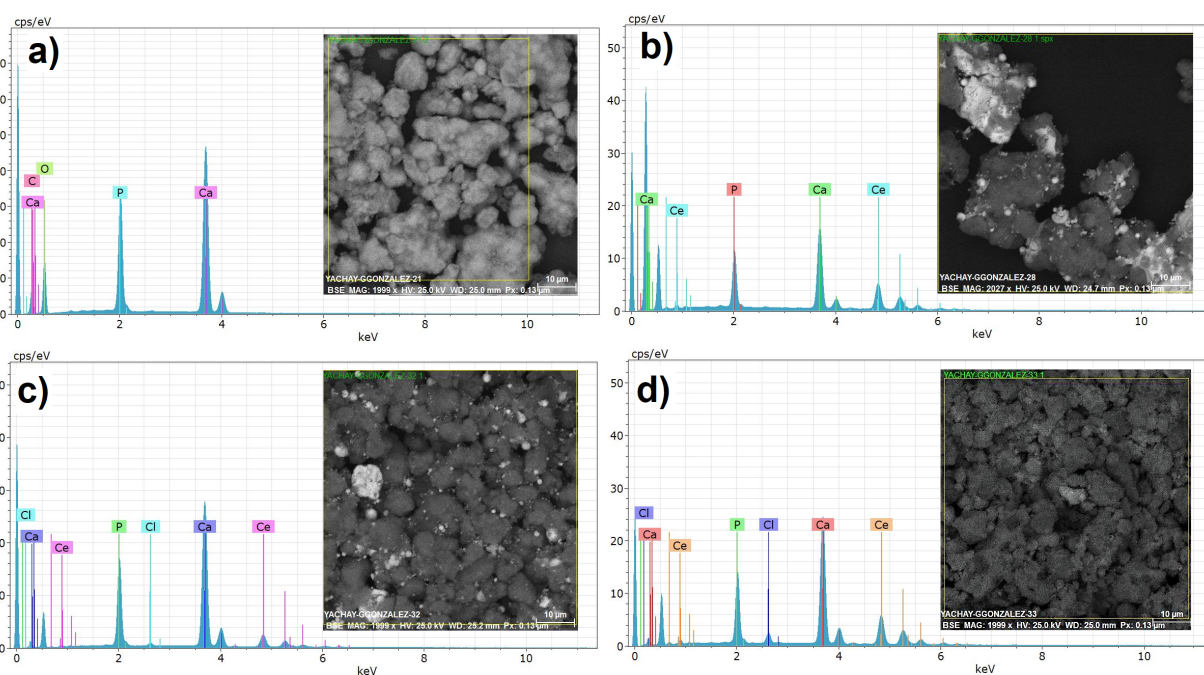


Figure 4.4: EDX microanalysis spectra of different Hydroxyapatite (HAp) doped systems. a) HAp doped with Lithium (25% w/w) using water as solvent, b) HAp doped with ceria NPs (0.1% v/w) using DMF as solvent, c) HAp co-doped with ceria (0.1% v/w) and Lithium (25% w/w) using DMF as solvent, d) HAp doped with ceria (0.1% v/w) and Lithium (25% w/w) using water as solvent. The peaks correspond to the presence of Ce, Ca, P, O and Cl in the doped HAp nanoparticles composition.

#### 4.1.2 Transmission Electron Microscopy

Figure 4.5 illustrates the TEM image of bare HAp nanopowder, and the TEM images of HAp/LiClO<sub>4</sub>, HAp/LiClO<sub>4</sub>/CeO<sub>2</sub> and HAp/CeO<sub>2</sub> samples calcined at 400 °C. Bare hydroxyapatite (Fig. 4.5a) consists of plates with non-uniform morphology with an average size of 200±50 nm long and 80±20 nm wide. This size differs with the SEM image



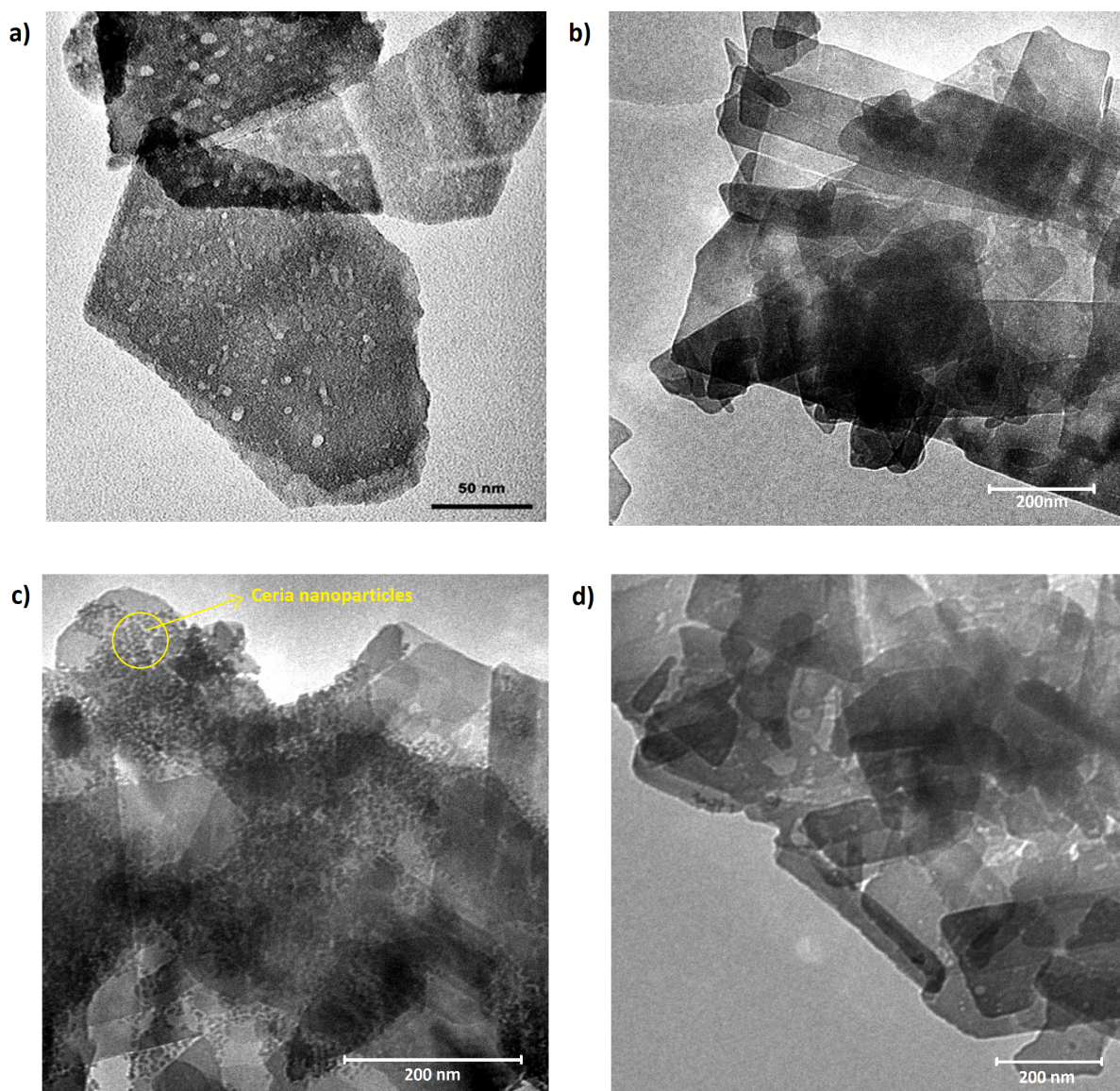


Figure 4.5: TEM images. a) Pure hydroxyapatite, b) Hydroxyapatite (HAp) doped with Lithium Perchlorate (25% w/w) using water as solvent, c) HAp doped with ceria NPs (0.1% v/w) using water as solvent, d) HAp co-doped with ceria NPs (0.1% v/w) and Lithium Perchlorate (25% w/w) using DMF as solvent.

(Fig. 4.1), it is probably a result of the agglomeration of particles in SEM preparation. The morphology of the doped composites, HAp/LiClO<sub>4</sub> (Fig. 4.5b), HAp/CeO<sub>2</sub> (Fig. 4.5c) and the co-doped system. HAp/LiClO<sub>4</sub>/CeO<sub>2</sub> (Fig.

4.5d) exhibit agglomeration of large overlapped plate crystals. The particle agglomeration perhaps is attributed to sample preparation for TEM. In the original hydroxyapatite sample, porosity can be observed. The darker places in figure 4.5b suggests that HAp/LiClO<sub>4</sub> compound could be composed of loaded Li<sup>+</sup> species. HAp/CeO<sub>2</sub> (Fig. 4.5c) shows nanoparticles with diameter around ~10 nm (calculated using ImageJ software), decorating the hydroxyapatite plates, these are ceria nanoparticles (It can be observed in the yellow circle in figure 4.5c) very well distributed and with a very uniform particle size. There is a clear difference between samples prepared using water as solvent or DMF. In the samples prepared in DMF, the distribution of nanoparticles is non-homogeneous. From all the above mentioned considerations (SEM, TEM), it should be noted that a uniform decoration of HAp by ceria nanoparticles and lithium is strongly dependent on the solvent used.

### 4.1.3 Fourier Transform Infrared Spectroscopy and Raman Spectroscopy

FTIR-ATR spectroscopy was used to analyze the corresponding changes of the functional groups in the structures of the raw, doped and co-doped hydroxyapatite nanocomposites. The doping process was carried out with two solvents, water and DMF. A detailed assignment of the vibration bands is given in Table 4.5.

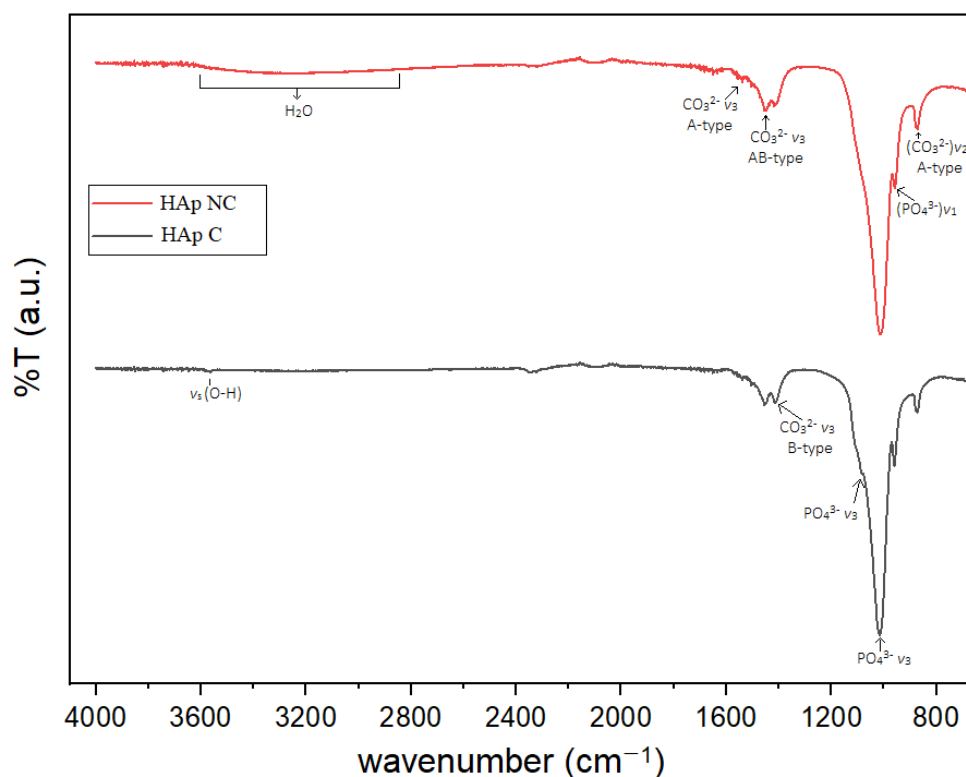


Figure 4.6: FTIR spectra of uncalcined (HAp NC) and calcined hydroxyapatite (HAp C)

Figure 4.6 illustrates the resulting FTIR spectrums of calcined and not calcined hydroxyapatite. Vibrational modes below  $650\text{ cm}^{-1}$  cannot be observed due to the FTIR spectra range. The raw uncalcined HAp shows the characteristic peaks of the phosphate groups. The  $\nu_3$  P-O asymmetric stretching mode is observed around  $1012\text{ cm}^{-1}$  and  $1083\text{ cm}^{-1}$  and the  $\nu_1$  P-O symmetric stretching mode is observed at  $959\text{ cm}^{-1}$ <sup>130</sup>. The characteristic O-H at  $3570\text{ cm}^{-1}$ <sup>131,6</sup> stretching modes  $\nu_s$  is absent, suggesting substitution for carbonate ions in the material. It can be confirmed by the presence of the  $\nu_3$  bending mode of  $\text{CO}_3^{2-}$  at  $1545\text{ cm}^{-1}$  (A type substitution  $\text{CO}_3^{2-} \rightarrow \text{OH}^-$ )<sup>132,133,6</sup>. Moreover, the carbonate groups at  $1456\text{ cm}^{-1}$   $\nu_3$  stretching and  $\nu_2$  bending mode at  $877\text{ cm}^{-1}$  (characteristic of AB and A type, respectively) as the  $\nu_3$  stretching mode at  $1415\text{ cm}^{-1}$  (B type substitution  $\text{CO}_3^{2-} \rightarrow \text{PO}_4^{3-}$ )<sup>132,134,6</sup> are also present. These strong carbonate bands indicate the presence of some important content of  $\text{CO}_3^{2-}$  in the hydroxyapatite structure. The vibrational bands from the region  $3000\text{--}3460\text{ cm}^{-1}$  as the peak at  $1650\text{ cm}^{-1}$  can be attributed to adsorbed water. When the HAp is doped with ceria nanoparticles, a small red shift is produced in the peaks of the phosphate groups as can be observed in the enlarged region ( $950\text{--}1125\text{ cm}^{-1}$ ) shown in figure 4.8b.

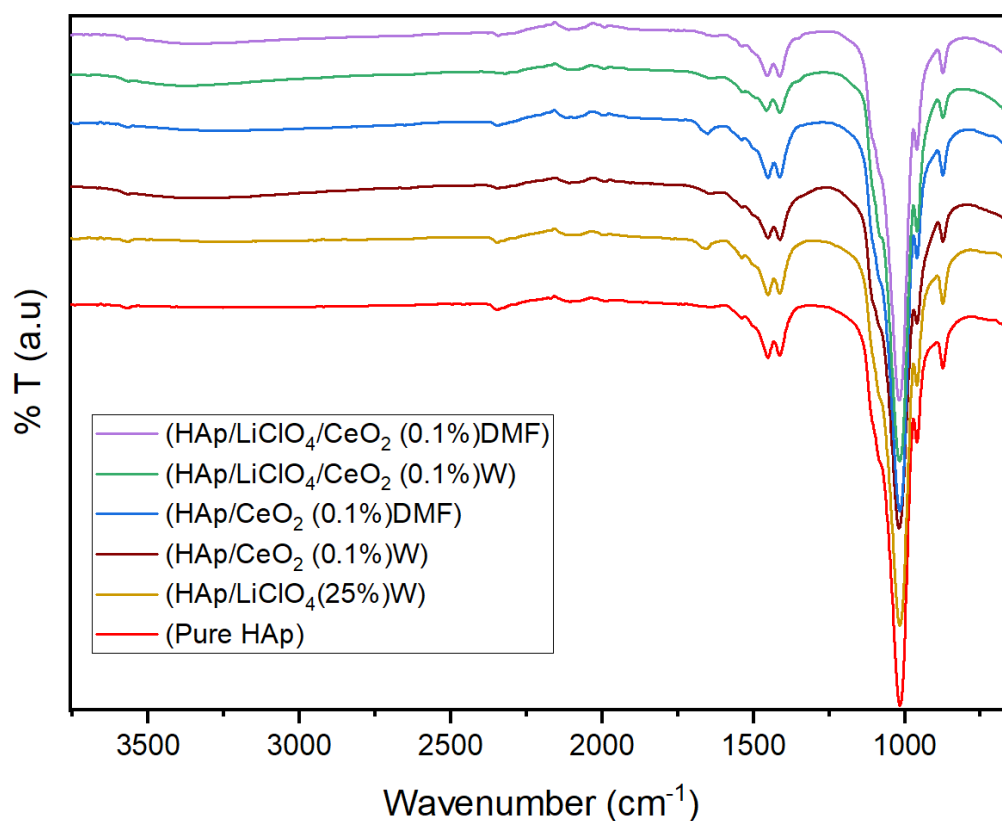


Figure 4.7: FTIR spectrums of calcined Pure HAp, doped and co-doped HAp samples, prepared in water and DMF. The amount of  $\text{LiClO}_4$  in the co-doped samples is 25% (w/w) respect to the HAp.

After the calcination process of the HAp nanopowder, the same vibrations as raw HAp are present, and the characteristic  $\nu_s(\text{O-H})$  band appears at  $3566\text{ cm}^{-1}$ <sup>131</sup>. The  $\nu_3$  asymmetric stretching mode of the phosphate groups can be observed also at  $1086$  and  $1113\text{ cm}^{-1}$ . (the enlarged region of the O-H group vibration ( $3100\text{-}3600\text{ cm}^{-1}$ ) is shown in figure 4.8d). Hydroxyapatite is a highly defective structure with a large content of vacancies, in general related to  $\text{OH}^-$  or  $\text{CO}_3^{2-}$  groups. It seems that during the heating process, a gradual decomposition and release of entrapped species (carbonate and  $\text{OH}^-$  groups) takes place.

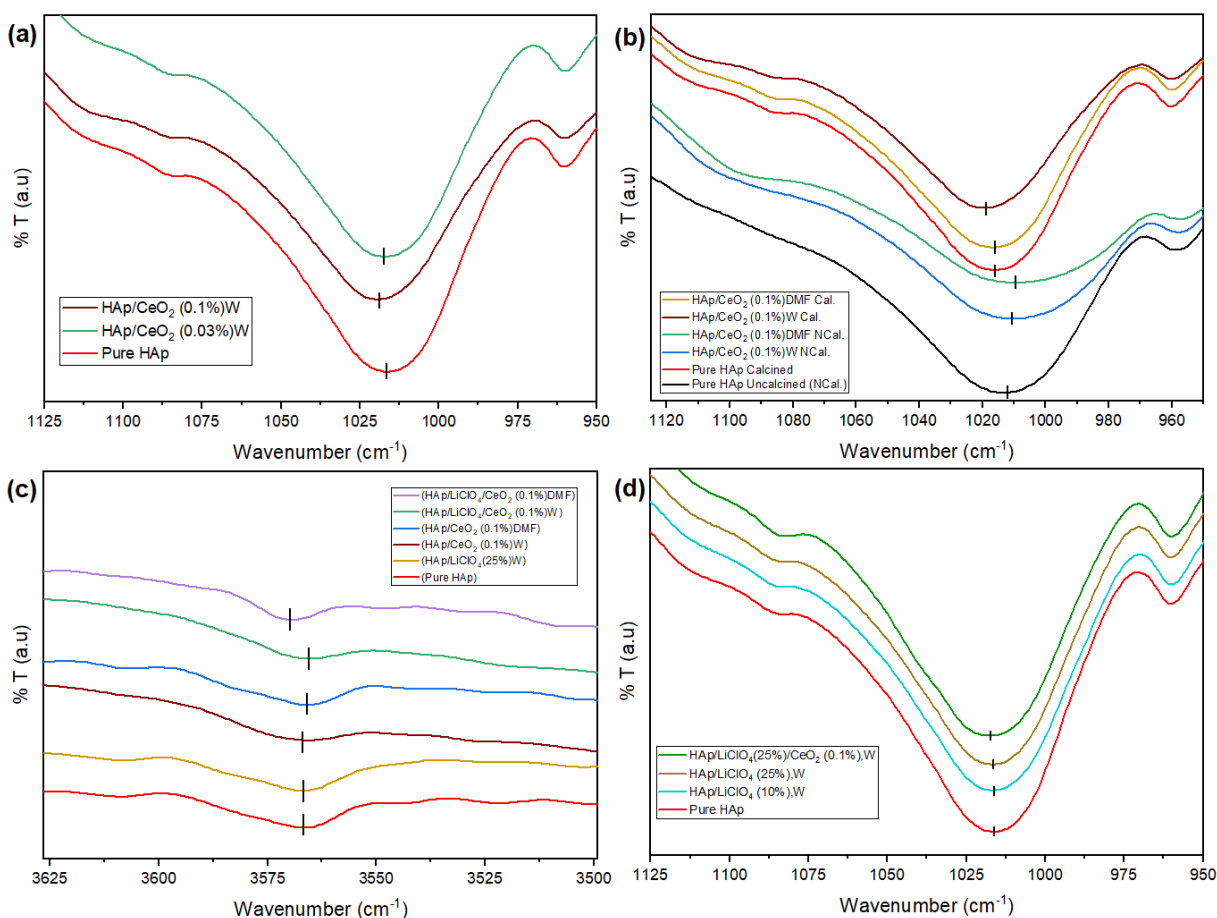


Figure 4.8: FTIR enlarged regions of the phosphate groups and  $\text{OH}^-$  groups. a) phosphate groups different ceria doped systems, b) comparison of phosphate groups between uncalcined and calcined samples, c)  $\text{OH}^-$  stretch, d) HAp doped with lithium perchlorate and co-doped with ceria nanoparticles.

Figure 4.7 illustrates the respective spectrums of calcined doped and co-doped hydroxyapatite nanocomposites. When hydroxyapatite is doped with ceria, some small changes can be observed in the spectra, especially in the peak intensities and some shifts in the phosphate groups. However, these changes can not be appreciated in the full range

of each spectrum. Thus, a comparison of the enlarged regions of the phosphate groups ( $950\text{--}1125\text{cm}^{-1}$ ) and OH groups are shown in figure 4.8.

A blue shift can be observed, that is dependent of the ceria NPs concentration, suggesting that the bond P-O becomes stronger when the hydroxyapatite is doped with cerium oxide nanoparticles after calcination (figure 4.8a) but this shift is not present when the solvent used is DMF, suggesting a stronger interaction between ceria nanoparticles and hydroxyapatite when the materials were prepared in water. This result is also consistent with the TEM micrographs, where a very uniform distribution of ceria nanoparticles is observed in those materials contrary to those prepared in DMF solvent. However, when these doped systems are compared with the same samples without calcination (figure 4.8b) the blue shift is more appreciable and occurs independent of the solvent used. Therefore, suggesting that the calcination process induce an interaction of the ceria ions with the phosphonate oxygen groups.

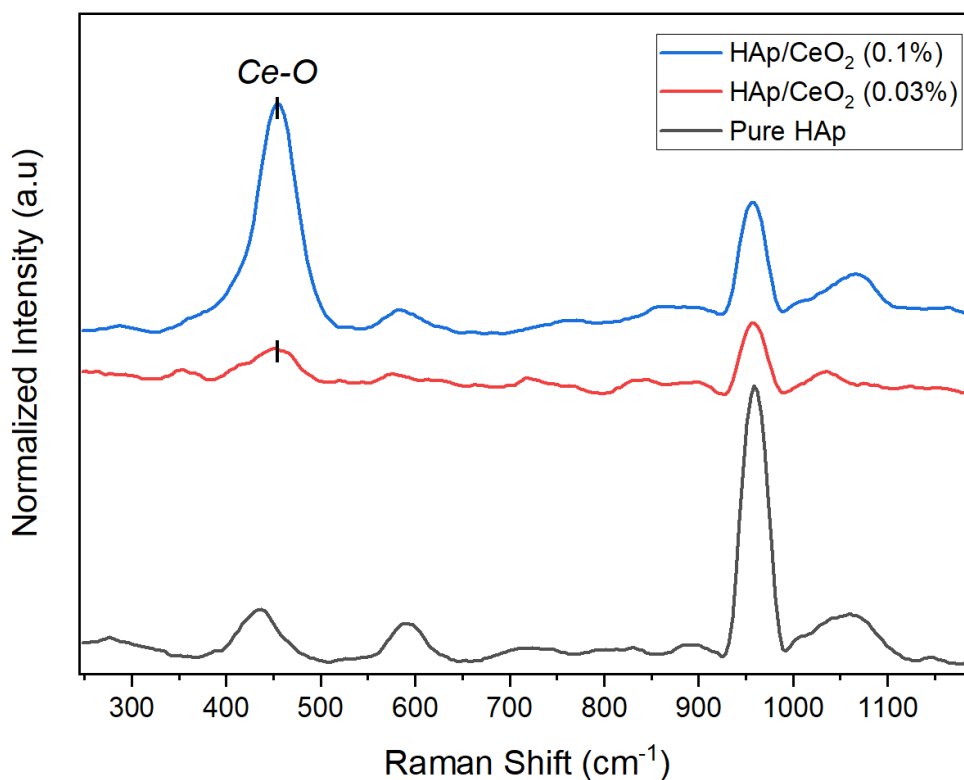


Figure 4.9: Raman spectrums of pure HAp and HAp doped with ceria nanoparticles at different concentrations (0.03% v/w) and (0.1% v/w) using water as solvent. Normalized to [0,1].

Complementary information to FTIR spectroscopy analyses was obtained by using Raman spectroscopy. Specially because of the limitation in range of the FTIR-ATR technique, where information about bands below  $650\text{ cm}^{-1}$  could not be observed. Figure 4.9 shows the Raman spectrums of the HAp and doped HAp without calcination. The

main vibrational bands observed in the uncalcined HAp spectra were attributed to the characteristic modes of the phosphate group. The band at  $435\text{ cm}^{-1}$  were assigned to  $\nu_2$   $\text{PO}_4^{3-}$  bend mode. The bands from  $594$  and  $610\text{ cm}^{-1}$  were assigned to the  $\nu_4$  antisymmetric bend modes of the  $\text{PO}_4^{3-}$  group. The  $\nu_1$   $\text{PO}_4^{3-}$  stretching mode band appeared at  $965\text{ cm}^{-1}$  and the stretching mode ( $\nu_3$ ) was observed at  $1053\text{ cm}^{-1}$ <sup>135</sup>. In the doped spectrums (figure 4.10) we can observe the peak assigned to Ce-O stretching vibrational mode that appears at  $455\text{ cm}^{-1}$ <sup>136</sup>. The intensity of these peaks increases as ceria increases. It is accompanied by red shifting for all characteristic vibrations of phosphate groups in the HAp structure. These results are in agreement with the FTIR results. As was suggested before the presence of strong interactions between phosphonated oxygens and cerium ions are most probably originated. It is in agreement with the reported literature<sup>137</sup>.

Sample	O-H stretch	$\text{CO}_3^{2-}$ $\nu_3$ -A-type	$\text{CO}_3^{2-}$ $\nu_3$ -B-type	$\text{CO}_3^{2-}$ $\nu_3$ -AB-type	$\text{PO}_4^{3-}$ $\nu_3$	$\text{PO}_4^{3-}$ $\nu_1$	$\text{CO}_3^{2-}$ $\nu_2$ -A-type
Uncalcined HAp	—	1539	1415	1456	[1012,1083]	959	873
Calcined HAp	3566	1539	1414	1453	[1016,1083]	959	872
HAp/CeO <sub>2</sub> (0.03)W	3567	1538	1415	1456	[1019,1082]	960	872
HAp/CeO <sub>2</sub> (0.1)W	3567	1539	1415	1456	[1020,1082]	960	872
HAp/LiClO <sub>4</sub> /CeO <sub>2</sub> (0.03)W	3565	1539	1415	1456	[1018,1082]	959	872
HAp/LiClO <sub>4</sub> /CeO <sub>2</sub> (0.1)W	3565	1539	1414	1456	[1018,1082]	959	872
HAp/CeO <sub>2</sub> (0.03)D	3566	1539	1415	1455	[1016,1082]	960	873
HAp/CeO <sub>2</sub> (0.1)D	3566	1539	1415	1455	[1016,1082]	960	873
HAp/LiClO <sub>4</sub> /CeO <sub>2</sub> (0.03)D	3570	1538	1415	1457	[1018,1083]	961	872
HAp/LiClO <sub>4</sub> /CeO <sub>2</sub> (0.1)D	3570	1538	1414	1457	[1018,1083]	961	872
HAp/LiClO <sub>4</sub> (10)W	3566	1539	1415	1456	[1016,1084]	960	872
HAp/LiClO <sub>4</sub> (25)W	3566	1539	1414	1456	[1016,1085]	960	872

Table 4.1: FTIR band assignment of calcined pure HAp, doped HAp and co-doped HAp samples. (W) represents to water and (D) represents to DMF. In the co-doped samples the amount of LiClO<sub>4</sub> is 25% w/w respect to the HAp.

#### 4.1.4 X-ray Photoelectron Spectroscopy

The surface composition and binding environment of the respective samples were analyzed by the use of this technique. For calibration due to charging effects Au, adventitious carbon peak and Fermi level were verified. The total spectrum of the Raw, doped and co-doped samples (calcined and uncalcined) are presented in Figure 4.10. The XPS survey spectrum (figure 4.10) of each sample shows the presence of characteristic elements constituents of hydroxyapatite such as Ca 2p, P 2p and O 1s<sup>138, 139</sup>. Moreover, the doping elements as cerium and lithium could also be identified in the respective spectra and the presence of chlorine residue.

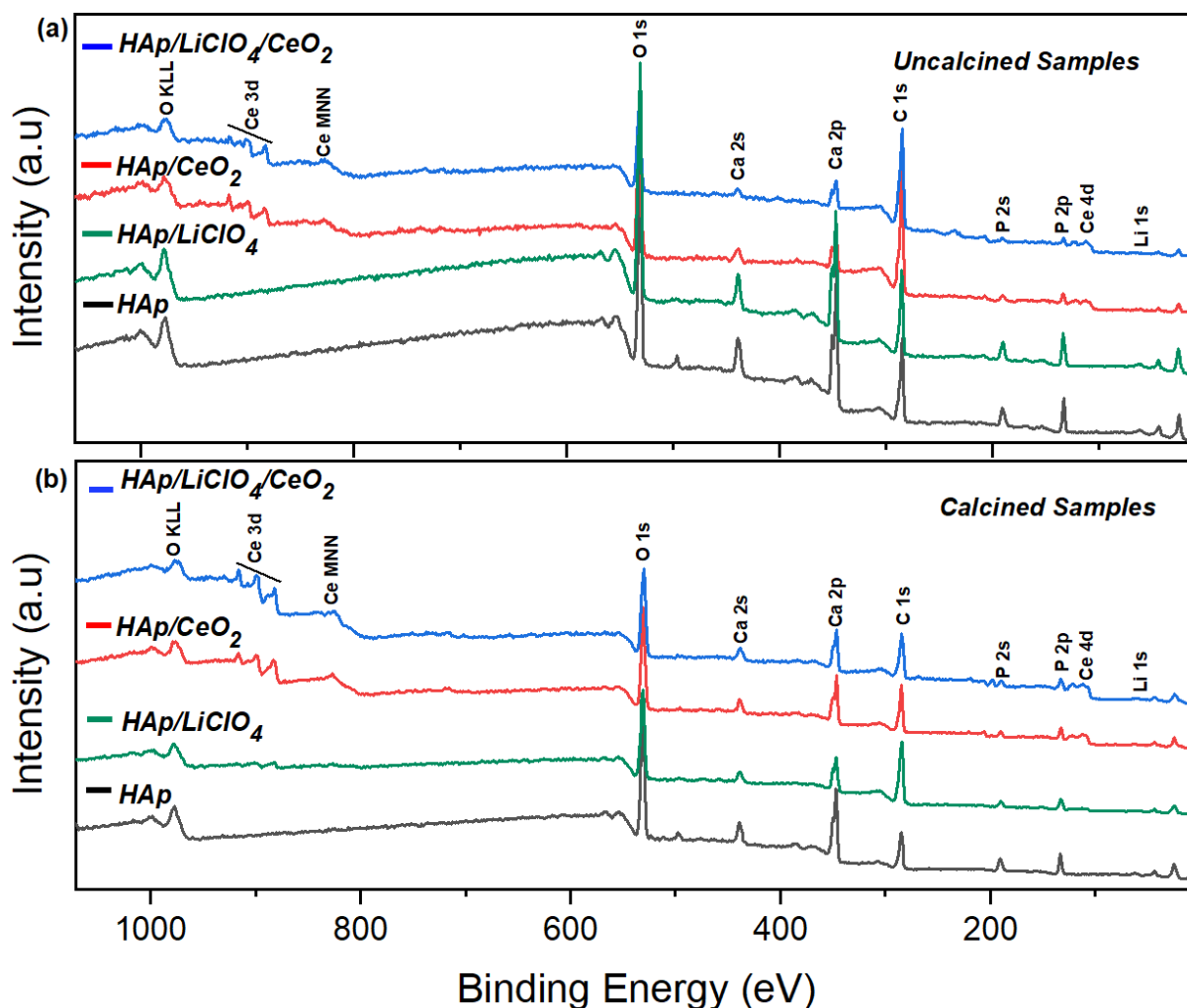


Figure 4.10: XPS spectra the undoped (black line), doped hydroxyapatite (green and red line) with  $\text{LiClO}_4$  (25% w/w) and  $\text{CeO}_2$  (0.1% v/w) respectively and codoped (blue line): (a) uncalcined, (b) calcined at 400 Celsius degrees.

Calcined samples show some differences in comparison with uncalcined samples. For example, the intensity of the samples has a slight change. Besides, a peak at 198 eV is present in the co-doped sample  $\text{HAp/LiClO}_4/\text{CeO}_2$  (Figure 4.10b, blue line), suggesting the presence of a small amount of Lithium Chloride ( $\text{LiCl}$ ) on this sample<sup>140</sup>. On the other hand, the detection of lithium is very low, due to two reasons. First, the relative sensitivity for each chemical element due to the electronic structure of lithium, making its detection by XPS a difficult process. Second a small amount of lithium is on the sample surface as lithium perchlorate ( $\text{LiClO}_4$ ) or in the case of the calcined  $\text{HAp/LiClO}_4/\text{CeO}_2$  as both  $\text{LiCl}$  and  $\text{LiClO}_4$ , and the rest of lithium ions entering to the structure of hydroxyapatite

and cerium filling interstitial spaces. The respective core level binding energies (BE) of Ca 2p, P 2p, O 1s, Ce 3d of each sample are shown in Table 4.6. These obtained BE values were in good agreement with the corresponding reported literature data (Table 4.7)<sup>140, 141, 142, 143, 144, 145, 146, 147</sup>.

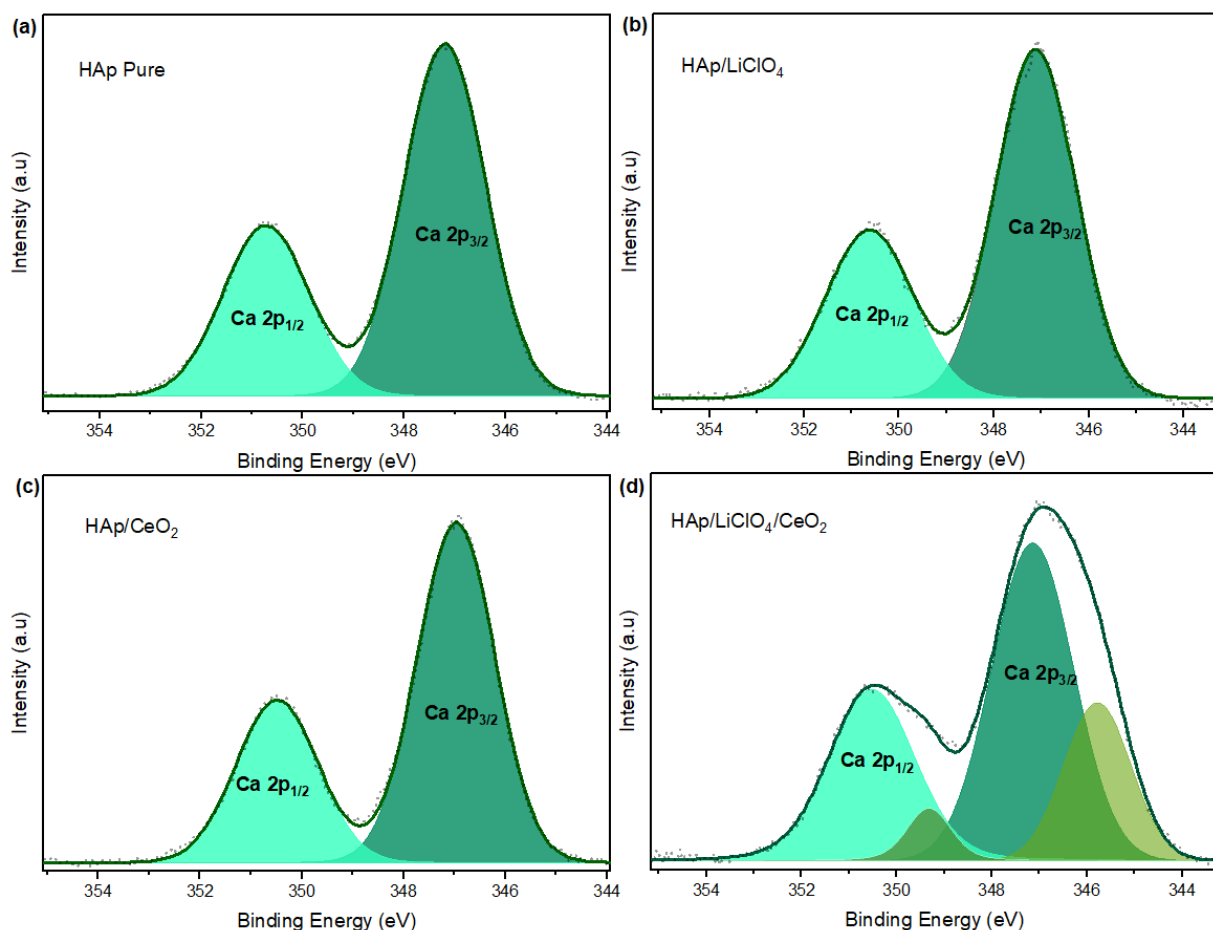


Figure 4.11: Core level Ca 2p XPS spectra of calcined samples at 400 Celsius degrees: (a) HAp Pure, (b) HAp/LiClO<sub>4</sub>(25% w/w), (c) HAp/CeO<sub>2</sub> (0.1% v/w), (d) HAp/LiClO<sub>4</sub>(25% w/w)/CeO<sub>2</sub>(0.1% v/w).

High-energy resolution analysis of individual peaks of each sample was carried out. These high-energy resolution scans of core levels O 1s, Ca 2p, P 2p and Ce 3d are illustrated in Fig. 4.11, Fig 4.12, Fig 4.13 and Fig 4.14 respectively. Each of the Ca 2p peaks displays a doublet band, the Ca 2p<sub>3/2</sub> and Ca 2p<sub>1/2</sub>. The envelopes were fitted with one peak at 347.18 and 350.72 eV respectively for pure HAP as observed in Fig. 4.11a. These peaks present a slight shift to the right (lower binding energy) when the HAP is doped and co-doped. The peaks around 347 and 351 eV, are attributed to Ca bonds characteristic of HAP<sup>141-143</sup>. However, in the figure 4.11d we can observe that each



envelope was fitted with two peaks respectively. It could suggest a major contribution of apatitic calcium phosphate (maximum of peak at 347 and 351 eV) for the first layers of surface of this sample. Corresponding the peaks with smaller intensity (maximum of peak at 345.72 and 349.29 eV) to calcium carbonate<sup>148</sup>.

Sample	Ca 2p <sub>1/2</sub>	Ca 2p <sub>3/2</sub>	P 2p <sub>1/2</sub>	P 2p <sub>3/2</sub>	O 1s	Ce 3d <sub>5/2</sub>	Ce 3d <sub>3/2</sub>	Li 1s
HAp	350.7	347.1	133	133.9	532.81 531.1			
HAp/LiClO <sub>4</sub>	350.6	347.1	133.1	134	532.81 531.1			
HAp/CeO <sub>2</sub>	350.5	347	132.9	133.9	532.6 531 529.7 528.8	882.2 885.1 888.5 898.1	900.6	
HAp/LiClO <sub>4</sub> /CeO <sub>2</sub>	350.5	346.9	132.9	134.1	532.8 531 529.6 528.6	882 885.1 888.3 897.9	900.5	56.1

Table 4.2: Core levels Binding Energies (eV) for calcined samples: HAp, doped HAp and codoped HAp.

Peak fit	Binding Energy (eV)	Chemical Bonds	Composition	References
Li 1s	56.10	Li-Cl	LiCl	[140]
Ca 2p <sub>3/2</sub>	347 / 347.2	Ca-O	Ca <sub>10</sub> (PO <sub>4</sub> ) <sub>6</sub> (OH) <sub>2</sub>	[141, 142]
Ca 2p <sub>1/2</sub>	350.7	Ca-O	Ca <sub>10</sub> (PO <sub>4</sub> ) <sub>6</sub> (OH) <sub>2</sub>	[143]
P 2p <sub>3/2</sub>	133	P-O	Ca <sub>10</sub> (PO <sub>4</sub> ) <sub>6</sub> (OH) <sub>2</sub>	[142]
O 1s	531.3	O-P/O-C	Ca <sub>10</sub> (PO <sub>4</sub> ) <sub>6</sub> (OH) <sub>2</sub>	[142]
	532.8	P-O-P	Ca <sub>10</sub> (PO <sub>4</sub> ) <sub>6</sub> (OH) <sub>2</sub>	[144]
	529.6	Ce-O	CeO <sub>2</sub>	[145]
	528.7	Ce-O	Ce <sub>2</sub> O <sub>3</sub>	[146]
Ce 3d <sub>5/2</sub>	898.3 / 888.6 / 882.2	Ce-O	CeO <sub>2</sub>	[147]
	885.3	Ce-O	Ce <sub>2</sub> O <sub>3</sub>	[147]
Ce 3d <sub>3/2</sub>	900.80	Ce-O	CeO <sub>2</sub>	[147]

Table 4.3: Reported binding energies and their assignments according to NIST Inorganic Crystal Structure Database and respective references

High-resolution spectrum associated with P 2p peak and its deconvolution for calcined samples of pure, doped and co-doped HAp are shown in Figure 4.12. The XPS spectrum of each sample of P 2p consists of two lines, P

$2p_{3/2}$  and  $P 2p_{1/2}$  spaced at around 0.9 eV one from the other. These peak components were around 133 and 133.9 eV respectively. These were attributed to phosphate groups of hydroxyapatite (P=O bonds) according to<sup>142, 143</sup>.

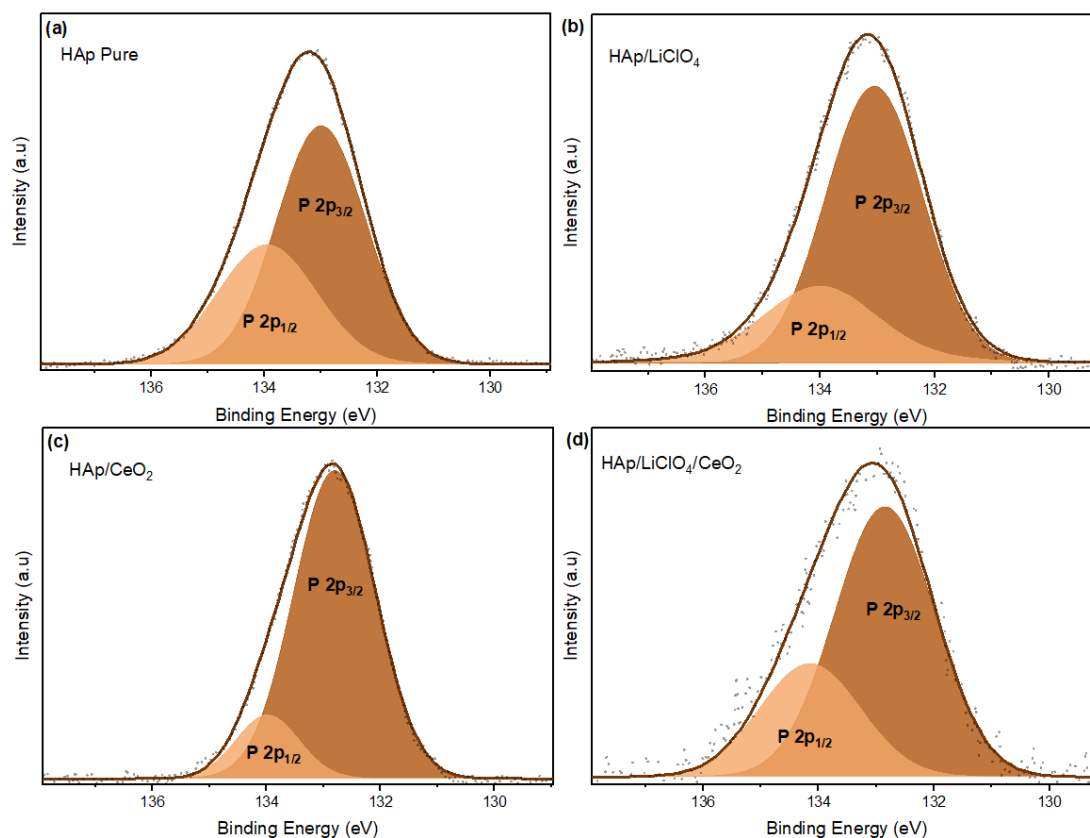


Figure 4.12: Core level P 2p XPS spectra of calcined samples at 400 Celsius degrees: (a) HAp Pure, (b) HAp/LiClO<sub>4</sub>(25% w/w), (c) HAp/CeO<sub>2</sub> (0.1% v/w), (d) HAp/LiClO<sub>4</sub>(25% w/w)/CeO<sub>2</sub>(0.1%v/w).

In Figure 4.13 the XPS high resolution spectra for O 1s peaks are illustrated. The broad O 1s peaks were deconvoluted into 2 peaks for samples without ceria doping, and 4 peaks for the samples with ceria doping, extra peaks could be overlapped. These contributions were fitted at around 528.7, 529.6 eV (ceria doping) correspond to oxides species(O<sup>2-</sup>) specifically to cerium dioxide compounds<sup>132, 133</sup>. Peaks at 531.1 eV, and 532.8 eV are related to hydroxyl oxygen (OH<sup>-</sup>) and phosphate groups (PO<sub>4</sub><sup>3-</sup>) (non-bridging oxygen (P-O)). There are a slight shift in the peaks positions when HAp is doped. The peak around 532.8 eV is the sum of some contributions as bridging oxygen (P-O-P), adsorbed water or Cl-O bonds in the case of the samples doped with lithium perchlorate<sup>144, 148, 149</sup>.

On the other hand, the XPS high resolution spectra for Ce 3d peaks are illustrated in Figure 4.14 two sets of spin-orbital multiplets, corresponding to the  $3d_{3/2}$  and  $3d_{5/2}$  contributions (labeled respectively). Additional spin-orbitals around 907 and 916 eV corresponding to the  $3d_{3/2}$  contribution can also be observed in the survey spectra shown

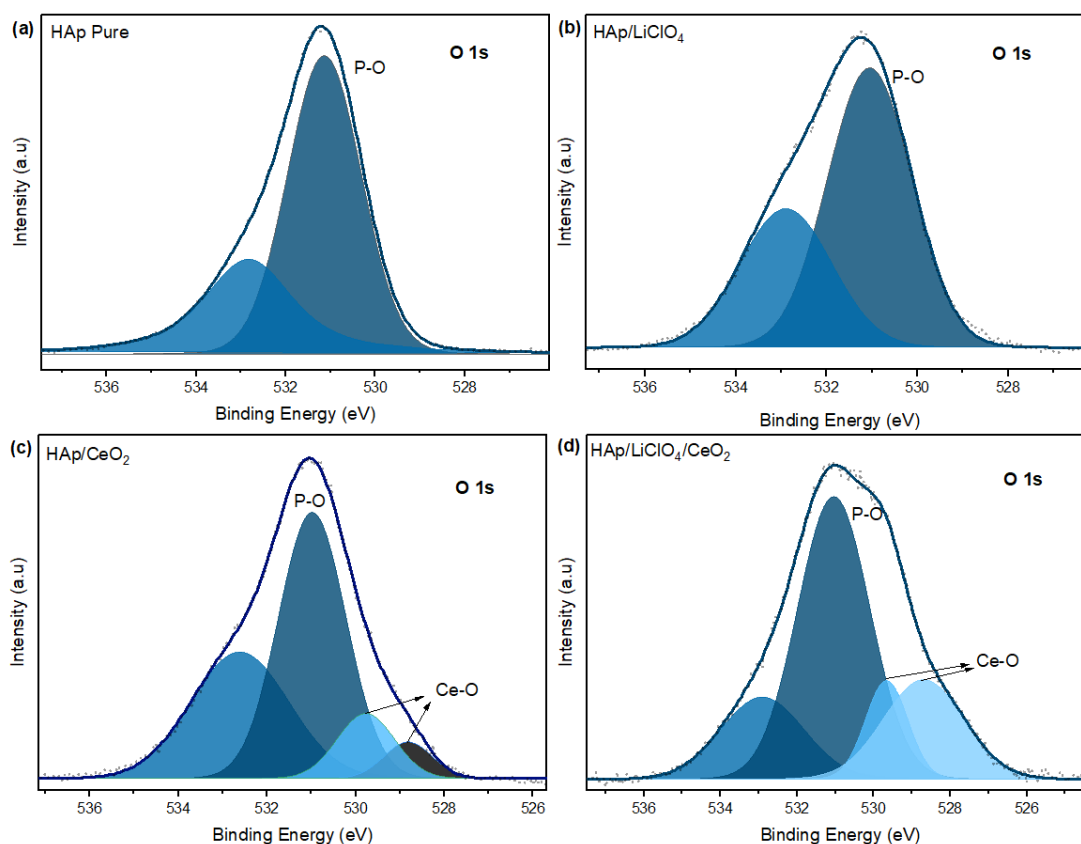


Figure 4.13: Core level O 1s XPS spectra of calcined samples at 400 Celcius degrees: (a) HAp Pure, (b) HAp/LiClO<sub>4</sub>(25% w/w), (c) HAp/CeO<sub>2</sub> (0.1% v/w), (d) HAp/LiClO<sub>4</sub>(25% w/w)/CeO<sub>2</sub>(0.1%v/w).

in Figure 4.10<sup>147, 150</sup>. A deconvolution of the respective 3d<sub>3/2</sub> and 3d<sub>5/2</sub> contributions was performed. As shown in figure 4.14 the respective oxidations states Ce (IV) and Ce(III) were identified and labeled in each deconvoluted peak respectively. The presence of the oxidation state (IV) as the oxide contribution observed in figure 4.13c and 4.13d represents the ceria nanoparticles. We can assume that some percentage of Ce(III) was formed during the synthesis process. Doping of ceria with lithium ions could be considered as a possibility, since they have similar ionic radii Li<sup>+</sup>(0.74Å) and Ce<sup>4+</sup>(0.97Å), and the doping could generate the formation of an oxygen vacancy and might have resulted in an uncompensated oxygen hole. Upon calcination Ce<sup>3+</sup> reacts with these oxygen holes and might have oxidised to Ce<sup>4+</sup>. And this explains the increase in Ce<sup>4+</sup> in fig 4.14d. This indicates that addition of Li ion in the ceria lattice influences the oxidation of Ce<sup>3+</sup> to Ce<sup>4+</sup>. However, we cannot rule out the formation of Ce(III) due to the characteristic process of oxidation-reduction of Ce(IV) under ultrahigh vacuum conditions during XPS measurements<sup>150, 46</sup>.

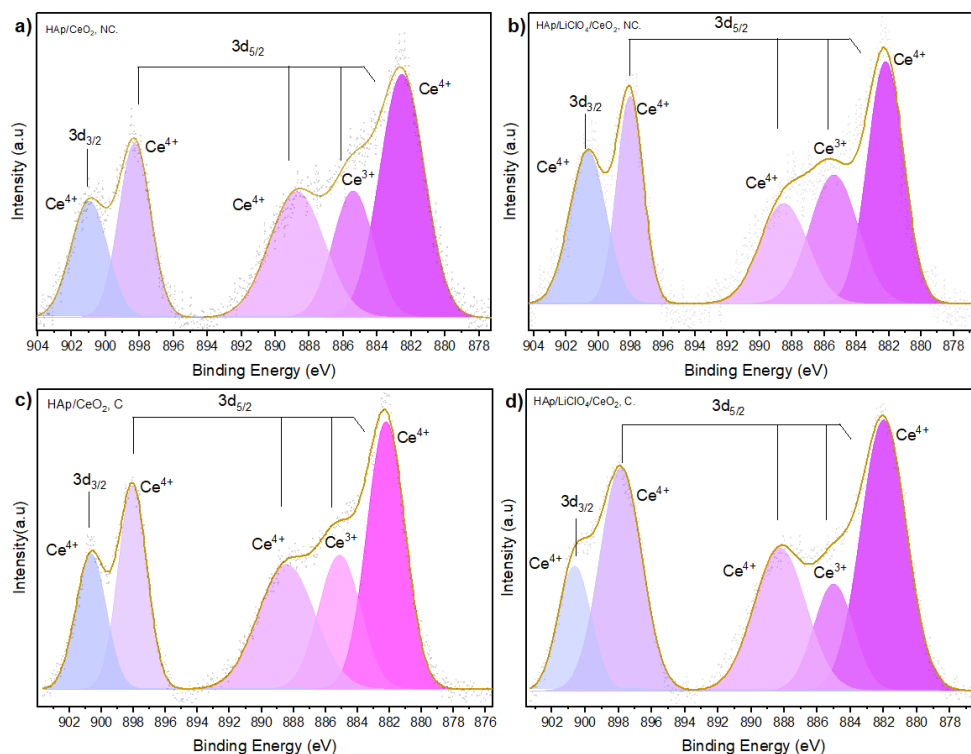


Figure 4.14: Core level Ce 3d XPS spectra: (a) HAp/CeO<sub>2</sub> (0.1% v/w) Uncalcined, (b) HAp/LiClO<sub>4</sub>(25% w/w)/CeO<sub>2</sub>(0.1% v/w) Uncalcined, (c) HAp/CeO<sub>2</sub> (0.1% v/w) Calcined, and (d) HAp/LiClO<sub>4</sub>(25% w/w)/CeO<sub>2</sub>(0.1% v/w) Calcined.

#### 4.1.5 X-ray Powder Diffraction

The crystal structures of uncalcined and calcined HAp, HAp/CeO<sub>2</sub>(0.1% v/w) and HAp/LiClO<sub>4</sub>(25% w/w)/CeO<sub>2</sub> (0.1% v/w) nanocomposites were examined by using XRD analysis. Figure 4.15 illustrates the different diffractograms showing the effects exhibited on the structure of the HAp NPs and ceria NPs doped-hydroxyapatite after being calcined. Raw hydroxyapatite nanoparticles displayed the stronger diffraction peaks at around  $2\theta = 25.65^\circ$ ,  $31.5^\circ$ ,  $31.94^\circ$ ,  $32.185^\circ$ ,  $34.01^\circ$ ,  $39.53^\circ$ ,  $46.38^\circ$  and  $49.24^\circ$ , corresponding to the (002), (3 -2 1), (1 -1 2), (300), (202), (4 -3 0), (4-2 2) and (3 -2 3) planes, which matched with the hexagonal P 6<sub>3</sub>/m carbonated-hydroxyapatite structure (QualX Data Card 00-900-3554)<sup>151</sup>. With the strongest peak (3 -2 1) at  $2\theta = 31.59^\circ$ . It is in agreement with the FTIR results, where an appreciable amount of carbonates could be observed. When HAp is calcined, there is a small shift to the right as we can see in Figure 4.15. The shifted peaks matched closer with the hexagonal P6<sub>3</sub>/m hydroxyapatite structure (QualX Data Card 00-901-1092) than the carbonated-hydroxyapatite structure (QualX Data Card 00-900-3554). With the strongest peak (3 -2 1) at  $2\theta = 31.76^\circ$ . This suggests that most trapped carbonates were released. Besides, this shift also occurs in the ceria NPs doped-HAp sample (Figure 4.15, green and red) and

increases when it is calcined. This shift could be attributed to the releasing of trapped compounds like carbonates or as was observed by FTIR analysis, a slight blue shift was present in the spectra of doped samples, proposing an interaction of the cerium ions with the phosphonated oxygen groups. Another explanation could be related to the formation of Frenkel defects<sup>152</sup>. The amorphous part present in the diffractogram belonging to the HAp/CeO<sub>2</sub> sample (red) is due to low amount of sample used resulting in an overlapping with the amorphous diffractogram of the glass holder used in the XRD measurements.

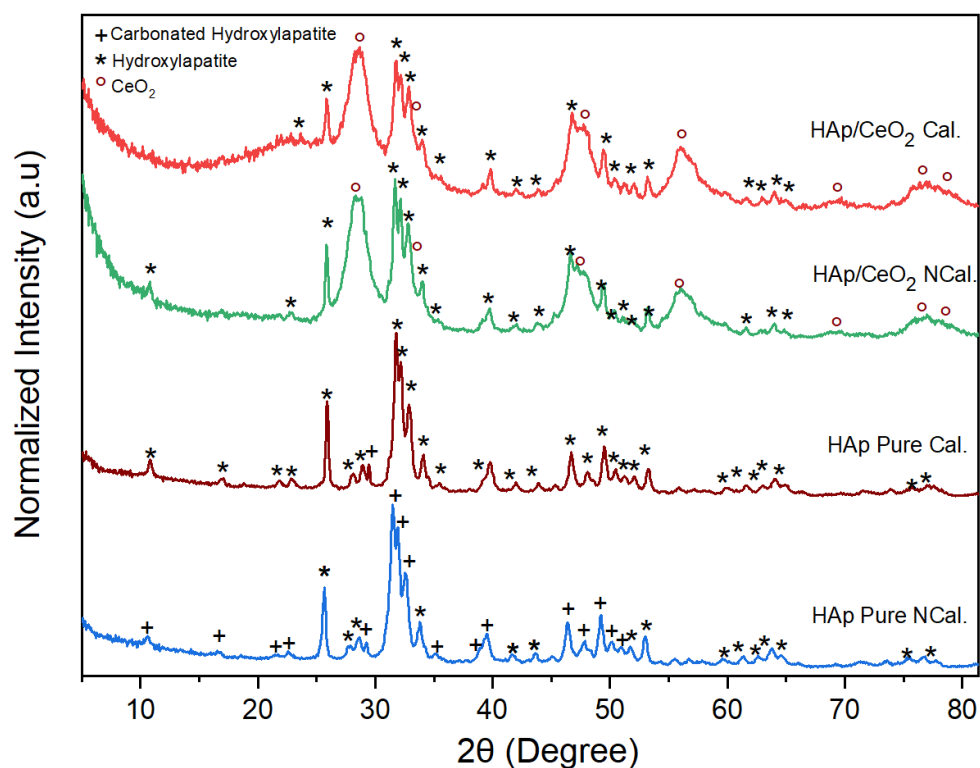


Figure 4.15: XRD diffractograms of uncalcined and calcined samples: blue) Pure HAp uncalcined, maroon) Pure HAp calcined, green) HAp/CeO<sub>2</sub> uncalcined, and red) HAp/CeO<sub>2</sub> uncalcined.

A comparison of doping hydroxyapatite with different compounds and combinations is illustrated in Figure 4.16. Doping HAp with Lithium Perchlorate did not show appreciable changes in the structure, possibly suggesting that Chlorine it is not substituting OH<sup>-</sup> groups and lithium ions may have entered into HAp structure filling interstitial spaces. When hydroxyapatite is doped with ceria nanoparticles, it displayed various extra diffraction peaks at around  $2\theta = 28.65^\circ$ ,  $33.27^\circ$ ,  $47.57^\circ$ ,  $56.49^\circ$ ,  $59.25^\circ$ , and  $69.50^\circ$ . The extra peaks matched well with the cubic fluorite type CeO<sub>2</sub> corresponding to the (111), (200), (220), (311), (222), and (400) planes, (QualX Data Card 00-900-9008), with the strongest peak (111) at around  $2\theta = 28.65^\circ$ <sup>153</sup>. We cannot talk about cerium ions substituting calcium ions in HAp because according to the conditions of synthesis employed these cannot be released from nanoceria crystals.

Moreover, reported studies<sup>154, 155</sup> have shown that substitution of calcium ions in HAp with larger ions implies an increase in the crystal size, and it cannot be observed in the obtained results. This suggests that nanocerium could be doping externally to HAp. The presence of broad diffractions peaks indicates a decreasing in crystallinity of the samples. On the other hand, an interesting change in peak intensity of HAp can be observed in the diffractogram of the co-doped HAp (Figure 4.16 green). This can be attributed to the contribution of a new phase formed Chlorapatite ( $\text{Ca}_5\text{ClPO}_3$ , JCDPS 00-027-0074), space group  $P6_3/m$ , whose main reflection at 32.815 overlaps the second main reflection of hydroxyapatite at 32.59, increasing its intensity. Additionally, a slight shift to the left, indicating a small increase in the cell size, consistent with the difference in lattice parameters between HAp and Chlorapatite (HAp:  $a=9.418$ ,  $b=9.418$ ,  $c=6.88$  vs. Chlorapatite:  $a=9.642$ ,  $b=9.642$ ,  $c=6.775$ ). Lithium Perchlorate is a stable salt that dissolves and dissociates easily in many solvents, specially under high ultrasonic sonication, therefore Chloride can exchange easily with the OH group of Hydroxyapatite and  $\text{Li}^+$  could enter into HAp structure occupying the interstitial sites. The co-doped samples were 20 min under sonication while the doped samples (HAp/ $\text{LiClO}_4$ ) were only 10 min, probably this explains the absence of this phase in the HAp/ $\text{LiClO}_4$  system.

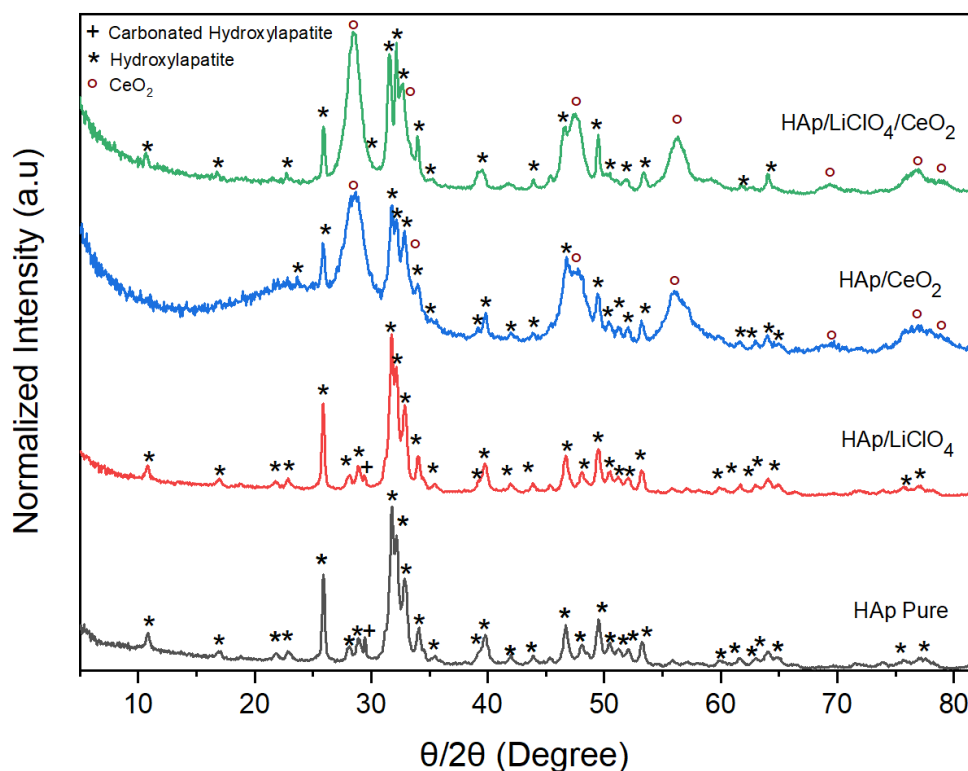


Figure 4.16: XRD diffractograms of calcined HAp, doped and co-doped HAp nanocomposites.

## 4.2 Optical Characterization

Here we performed the optical analysis of the respective samples. UV-Vis Spectroscopy and Photoluminescence Spectroscopy techniques are used to go inside the optical properties (Band gap and photoluminescence) of the respective nanocomposites.

### 4.2.1 Diffuse Reflectance and Band Gap Calculations

The band gap energy ( $E_g$ ) for all the doped and co-doped samples, uncalcined and calcined were calculated from diffuse reflectance experiments. Kubelka-Munk model was used for estimating the absorption coefficient<sup>117</sup>, using the next equation,

$$F(R) = \frac{K}{S} = \frac{(1 - R_\infty)^2}{R_\infty} \approx \alpha \quad (4.1)$$

where, K and S are the absorption and scattering coefficients, respectively, while the reflectance  $R_\infty$  is equal to:  $R_{\text{sample}}/R_{\text{standard}}$ , and  $F(R)$  is the Kubelka-Munk function and it is proportional to the absorption coefficient ( $\alpha$ ).

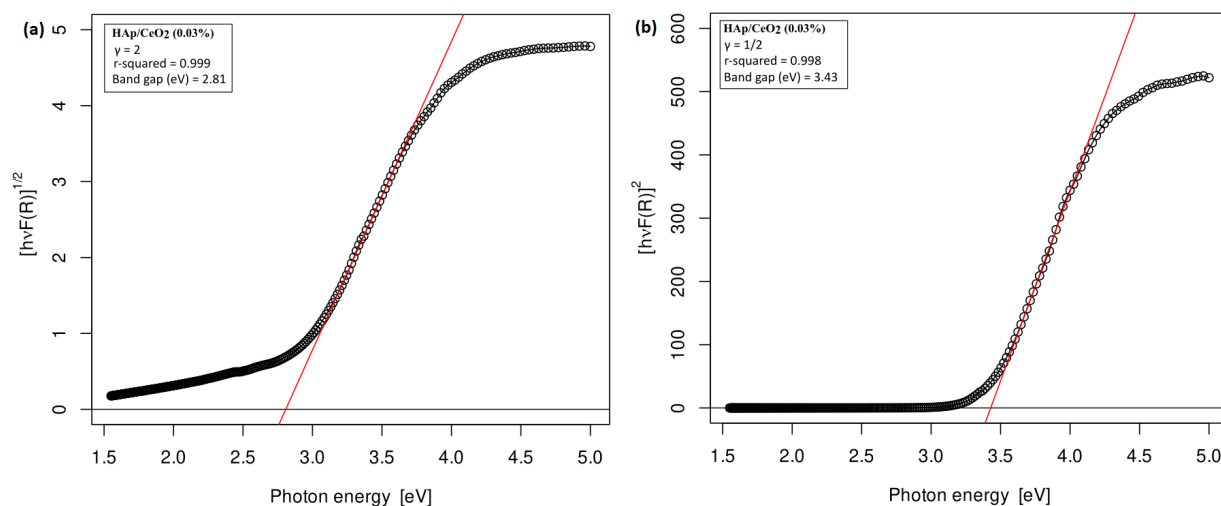


Figure 4.17: Optical band gap energy estimation using extrapolation method for ceria (0.03%) doped-hydroxyapatite: (a) Plot of  $(\alpha h \nu)^{1/2}$  as a function of photon energy; from the linear part of the plot (red line) we obtain the indirect optical band gap.  $\gamma = 2$ , (b) Plot of  $(\alpha h \nu)^2$  as a function of photon energy; from the linear part of the plot (red line) we obtain the indirect optical band gap.

In order to perform the band gap energy estimation Tauc Plot (Figure 4.17) is used considering allowed direct and indirect optical transition. Where,  $\gamma = 1/2$  (direct) and  $\gamma = 2$  (indirect) were used as the exponents in the modified Tauc equation<sup>119</sup>.

$$h\nu F(R) = A * (h\nu - E_g)^\gamma \quad (4.2)$$

So, by plotting  $[F(R)h\nu]^{1/2}$  against  $h\nu$ , we can estimate the optical  $E_g$  of the material from the x-axis ( $\alpha = 0$ ) intercept of the line that is tangent to the inflection point of the curve. The band gap energy values for all the samples are in the range of 3 – 4.11 ( $\gamma = 1/2$ ) and 2.3 – 3.57 eV ( $\gamma = 2$ ) (See complete data in Table 4.8). According

Solvent	% CeO <sub>2</sub>	% LiClO <sub>4</sub>	Calcined	Band Gap ( $\gamma = 1/2$ )	Band Gap ( $\gamma = 2$ )
Water	0.03	0	No	3.43	2.82
Water	0.1	0	No	3.33	2.86
DMF	0.03	0	No	3.13	2.62
DMF	0.1	0	No	3.26	2.74
Water	0.03	0	Yes	3.43	2.81
Water	0.1	0	Yes	3.39	2.91
DMF	0.03	0	Yes	3.01	2.36
DMF	0.1	0	Yes	3.02	2.46
Water	0	25	No	4.11	3.57
Water	0	25	Yes	4.02	3.24
Water	0.03	25	No	3.54	2.96
Water	0.1	25	No	3.32	2.9
DMF	0.03	25	No	3.28	2.68
DMF	0.1	25	No	3.13	2.67
Water	0.03	25	Yes	2.95	2.26
Water	0.1	25	Yes	3.49	3.01
DMF	0.03	25	Yes	3.2	2.48
DMF	0.1	25	Yes	3.06	2.54

Table 4.4: Band Gap (eV) values of the respective HAp-doped system

to reported data<sup>156-157</sup>, and the linearity presented in each band gap approximation, an allowed indirect electronic transition was assumed for discussion. The calculated  $E_g$  of pure HAp was 4.09 for the uncalcined sample and 3.6 eV for the calcined sample. HAp band gaps have been calculated theoretically elsewhere using density functional theory<sup>156,158</sup>, reporting values in the range of 5.23<sup>156</sup> to 5.40 eV<sup>158</sup>. Besides, experimental band gap energy values have been reported from 3.45 eV<sup>159</sup> to 5.78<sup>157</sup>. The obtained  $E_g$  value is in agreement with those values reported in the literature. The differences between theoretical and experimental values could be due to synthesis conditions or heat treatments of hydroxyapatite that can create a strong difference in the density of defects. From the obtained results (Table 4.8) we can see that the presence of ceria nanoparticles reduces significantly the band gap values with respect to the  $E_g$  data reported for HAp either uncalcined or calcined. Furthermore, adding Lithium Perchlorate did not show an effect in the optical band gap but when it is calcined, a decrease in the band width is appreciable,



probably due to the insertion of  $\text{Li}^+$  into the interstices cation sites. The decrease of the optical band gap in samples doped with ceria nanoparticles (compared with the reported data of only HAP) could be related to the  $E_g$  of only ceria nanoparticles<sup>160</sup>, that now is converted in the new band width of the new compound HAp/CeO<sub>2</sub>. Additionally, the decreasing of the  $E_g$  in the HAp doped with Lithium Perchlorate when it is calcined can be also linked with the presence of  $\text{OH}^-$  and  $\text{O}^-$  vacancies that according to Bystrov et al.<sup>161</sup> could create a series of energy levels in the forbidden band that plays an important role in the recombination of electron hole. Moreover, the solvent used during the synthesis has an important effect in the respective  $E_g$  values. It looks that a shorter band gap is resulted when DMF is used as a solvent. It could be due to the dispersion of the respective dopants. From table 8, it can be observed that the band gap (direct permitted transition) increases as the ceria content increases. However in the codoped samples a reduction of the band gap of ceria doped samples was observed for samples treated either in DMF or in water and this is in general not affected by the ceria content in the sample. This can be attributed to the insertion of  $\text{Li}^+$  ions into the ceria structure. The values obtained are well below the reported  $E_g$  for ceria<sup>162</sup>.

#### 4.2.2 Photoluminescence Spectroscopy

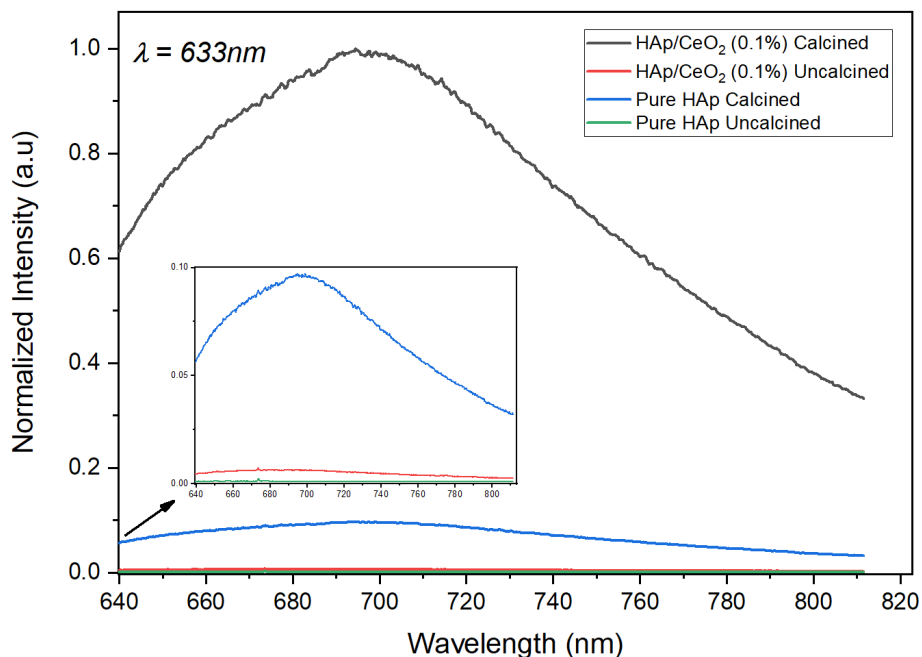


Figure 4.18: Photoluminescence spectra showing the effect of calcination and doping with ceria nanoparticles: uncalcined HAp (green line) and HAp/CeO<sub>2</sub> (0.1%) (red line) shows a poor emission signal. This signal increases ten times when HAp is calcined (blue line), and the nanoceria doped-HAp (black line) exhibits a very high emission (more than 10 times the intensity the calcined HAp)

Photoluminescence spectroscopy is carried out to investigate the luminescent properties of the respective doped-systems. The measurements were carried out with an excitation wavelength of 532 and 633 nm, with an integration time of 5 seconds. Figure 4.18 illustrates a comparison of the photoluminescence (PL) spectra (excitation wavelength of 633 nm) of pure and ceria doped-hydroxyapatite, uncalcined and calcined at 400 °C. Both, pure and doped-HAp uncalcined samples exhibited a poor photoluminescence emission signal compared with the calcined samples. Calcination of HAp increases up to ten times the luminescence response of the sample. Moreover, doping HAp with ceria nanoparticles increases considerably the luminescence response of the nanocomposite (more than 10 times the intensity of the calcined hydroxyapatite). It could be related with the formation of vacancies. It will be more discussed in the following paragraphs.

Figure 4.19a and 4.19b illustrate the PL spectra of doped samples with water and DMF as solvent with an excitation wavelength of 533 nm and 633 nm respectively. At an excitation of 532 nm a broad spectrum is recorded, where 3 emission peaks can be identified at around 694, 710 and 749 nm. On the other hand, an excitation of 633 nm produced a broad emission with peaks at around 683, 694, 702 and 714nm. Spectra obtained with an excitation wavelength of 532 nm contains emission peaks present when an excitation of 633 nm is applied. It is possible that this spectra (Figure 4.18a) contains all the peaks present in figure 4.19b because 532nm has greater energy than 633 nm. However, some peaks cannot be observed due to the broad spectrum. The intensity of the peaks is higher when the solvent used is water. This tendency can be observed with both excitation wavelengths, 532 (Fig. 4.19a) and 633nm (4.19b). Furthermore, a decrease in photoluminescence intensity can be seen when hydroxyapatite is co-doped with ceria nanoparticles (Figure 4.20). It seems that lithium is acting as a quenching material. Although, the PL intensity is still higher than pure calcined HAp. Moreover, the effect solvent is not present in these spectrums. PL intensity of sample synthesized in DMF is similar to sample synthesized in water.

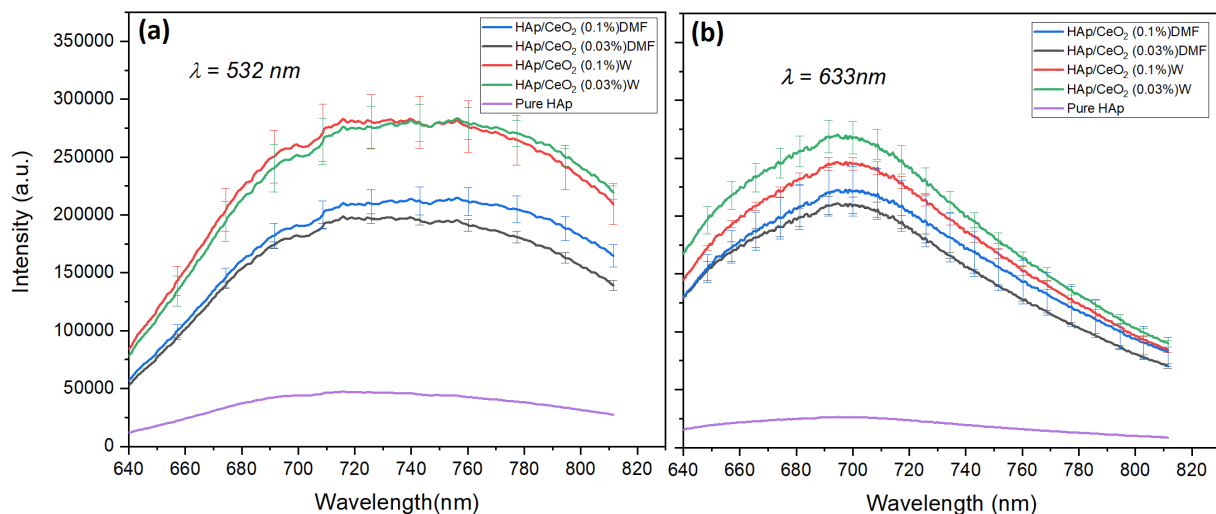


Figure 4.19: Photoluminescence spectra of calcined samples at different excitation wavelengths with the respective error bars: a) excitation wavelength at 532 nm, b) excitation wavelength at 532 nm.

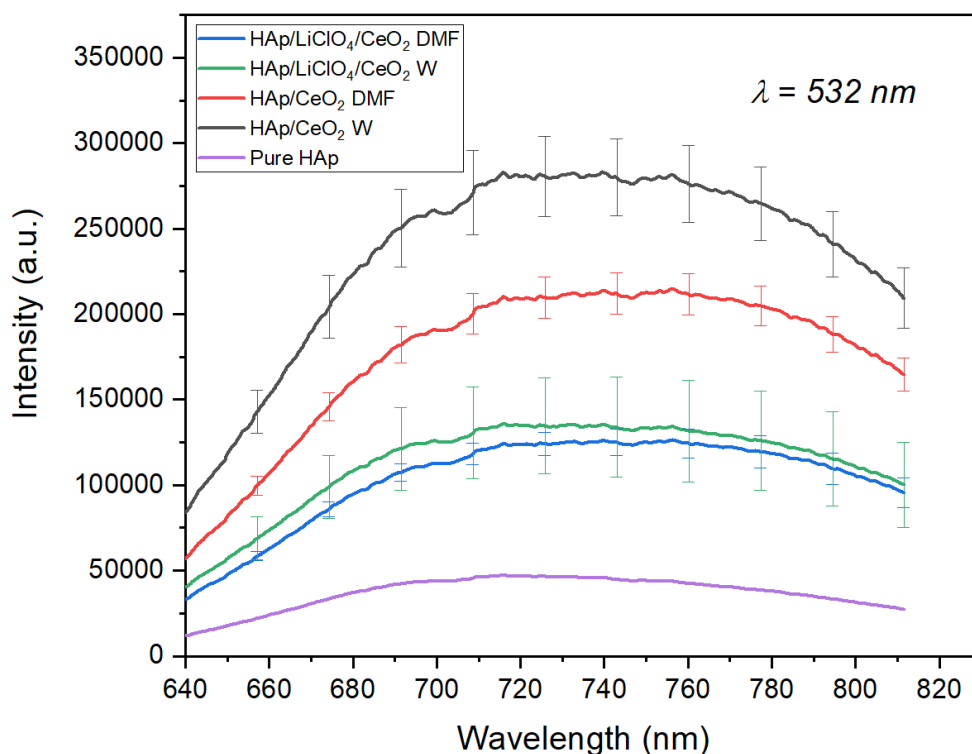


Figure 4.20: Photoluminescence spectra of calcined doped and co-doped samples with an excitation wavelength at 532 nm. Lithium quenching effect can be observed. Reference calcined HAp spectrum (purple line) is shown.

Despite, there are no investigations reporting photoluminescence response of hydroxyapatite and ceria nanoparticles with an excitation wavelength of 532 and 600 nm. This study can be made without taking account the band gap connection with PL. In that context, the increase in photoluminescence (PL) response of calcined hydroxyapatite can be related to the presence of vacancies, defects or impurities in the structure. According to Gonzalez et al.<sup>70</sup> this PL response in hydroxyapatite depends on the presence of defects and impurities that can be thermally activated in a range of temperature from 350 to 450 celsius degrees. Moreover, they added that there is a relation between the PL response and the amount of hydroxyl groups ( $\text{OH}^-$ ) and carbonates ( $\text{CO}_3^{2-}$ ). However, the explanation about the PL response of the nanoceria (0.1% v/w) doped-hydroxyapatite becomes more complicated due to the coexistence of both compounds. So, it is better to understand the luminescence behaviour of ceria nanoparticles and then link it with the PL contribution of HAp. Recent photoluminescence studies<sup>16, 17, 77</sup> of nanoceria have shown different mechanisms through ceria nanoparticles to express their luminescent properties. Relaxation via the 5d-4f transition of the  $\text{Ce}^{3+}$  ions, a down conversion process, causing the conduction band electrons to make a transition to the defect state within the bandgap<sup>16</sup>. Structural organization level and charge transfer transitions between  $\text{O}^{2-}$  and  $\text{Ce}^{4+}$  giving a high concentration of  $\text{Ce}^{3+}$  ions, which is associated with a high concentration of  $\text{O}^-$  vacancies<sup>17, 77</sup>. Therefore, we can attribute this high photoluminescence response to the defects in the structure produced after the calcination

process. And, when HAp is doped with nanoceria, the PL response of the latter is added to the HAp PL. It seems that the synthesis carried out using water as a solvent produced more structural organization level and charge transitions than the synthesis using DMF as solvent. Finally, lithium could be acting as quenching because it is filling defects produced either in the HAp structure or in the nanoceria structure.

### 4.3 Final Discussion and Doping Model

SEM and TEM images allowed us to see the dispersion, morphology and approximate size of nanoparticles. Moreover, SEM, EDS, TEM, Raman, XPS and XRD confirmed the presence of ceria nanoparticles doping HAp. In SEM brighter spots belonging to a higher atomic number element (cerium) was observed. In TEM, ceria Nps were attached on the HAp nanoparticles surface. Moreover, the percentage of this element (cerium) was obtained by using EDS. XPS, gave us the respective oxidation states present in the ceria nanoparticles. And, the characteristic peak of ceria in the Raman spectrum was present as the characteristic peaks in the respective diffractograms. It was also observed by EDS that our HAp was not stoichiometric, and as FTIR as XRD results confirmed that our pure HAp presented carbonate substitutions in its crystal structure substituting the  $\text{OH}^-$  and  $\text{PO}_4^{3-}$  groups, forming A-type and B-type carbonated HAp respectively. A reported sketch of this typical process<sup>42</sup> was shown in Figure 2.2.

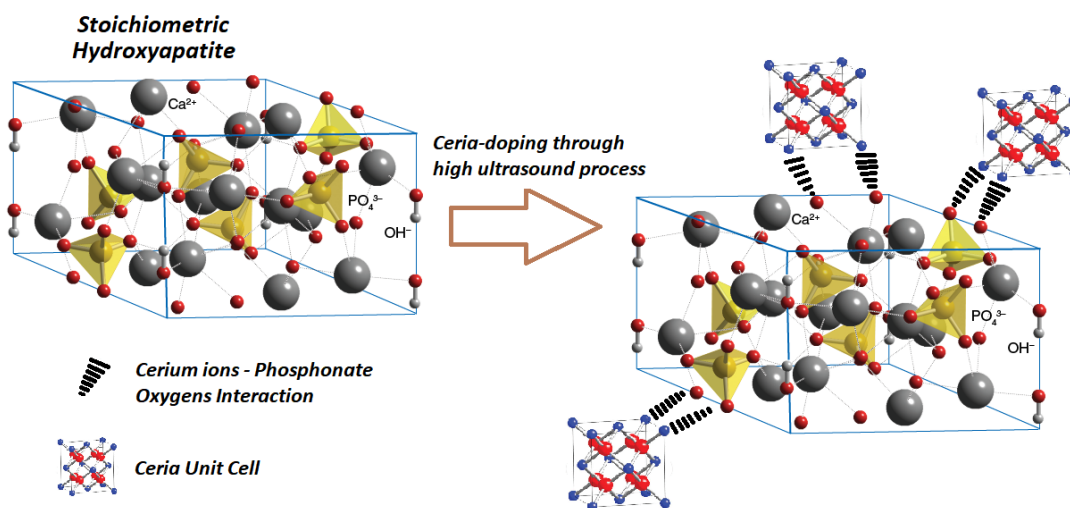


Figure 4.21: Ceria doping externally hydroxyapatite model. Example using a stoichiometric hydroxyapatite unit cell. Modified sketch from Wahba et al.<sup>89</sup>

However, carbonate release after the calcination process was appreciated in the XRD and FTIR results, leading to the creation of vacancies in the HAp structure. Moreover, high resolution XPS measurements showed the presence of  $\text{Ce}^{3+}$ , suggesting the creation of oxygen vacancies in the ceria crystal structure. This formation of vacancies can be clearly considered responsible for the photoluminescent response of each sample. Figure 4.21 illustrates an example

of the proposed external ceria-doped hydroxyapatite model. For simplicity, a stoichiometric hydroxyapatite unit cell [P<sub>63</sub>/m] was taken into account to explain how the hydroxyapatite was doped externally with ceria nanoparticles. However, vacancies formed after carbonates releasing in HAp and oxygen vacancies in ceria crystals have to be considered and the possible insertion of lithium ions into the interstices cation sites of the HAp crystal structure and into the ceria crystal structure. The effect of lithium ions could be observed as a decreasing factor for the band gap value and quenching in the photoluminescent response. Furthermore, chlorapatite was formed after 20 min high frequency ultrasonic sonication in the co-doping systems.



## Chapter 5

# Conclusions & Outlook

In the present work, the development of three-model novel nanosystems with fluorescent properties by high frequency ultrasound synthesis is reported. HAp was doped with Lithium Perchlorate ( $\text{LiClO}_4$ ) and ceria nanoparticles ( $\text{CeO}_2$ ). In addition, a co-doping of hydroxyapatite with these two compounds was performed. In order to get a better dispersion, two solvents were used, an organic (DMF) and an inorganic solvent (Water). The presence of ceria nanoparticles was confirmed with the different characterization techniques used (SEM, EDS, TEM, FTIR Spectroscopy, Raman Spectroscopy, XPS and XRD). SEM results revealed a better dispersion of ceria nanoparticles when the solvent during the synthesis was water. FTIR and XRD results demonstrated the nature of the hydroxyapatite being carbonated (Type A and Type B). They also showed the release of these carbonates when the respective samples are calcined as the modified HAp structure when where partially co-doped changing to a chlorapatite structure. In addition, XPS exhibited the presence of  $\text{Ce}^{3+}$  ions. Being these last two conditions the responsible of the formation of vacancies in the respective structures of HAp and nanoceria. Moreover, optical studies (Reflectance Diffuse Spectroscopy and Photoluminescence) exposed interesting properties of the respective nanocomposites. Optical band gap values are affected depending on the system (Calcined and doped system). Photoluminescence measurements displayed a great difference between photoluminescence intensities between calcined and uncalcined samples. This result can be strongly linked with the creation of vacancies during the calcination process. Also, it could be observed that the concentration of ceria nanoparticles was not affecting the intensities of the photoluminescence peaks. However, as lithium ions acted as quenchers. Besides, the solvent has an important effect in the  $E_g$  (In DMF is smaller than in water) and in the photoluminescence response. It could be related to the dispersion of each system.

In conclusion, external doping of hydroxyapatite with ceria nanoparticles at different concentrations was successfully carried out, being HAp/ $\text{CeO}_2$  the nanocomposite with the highest photoluminescence response. Calcination played an important role in the creation of vacancies. Moreover, Lithium ions seem to enter into interstitial spaces of the hydroxyapatite and/or ceria structures creating defects, and due to the dissociation of  $\text{LiClO}_4$  and the influence of the high frequency ultrasound process during the synthesis of the co-doped samples, chlorine ions partially replaced  $\text{OH}^-$  ions leading in the formation of chlorapatite. Also, the inserted lithium ions were acting as photoluminescence quenchers. Therefore, the respective results suggests potentials applications of HAp/ $\text{CeO}_2$  to be used as a fluorescent

probing for bioimaging. On the other hand, band gap values are in agree with the reported in the literature and this phenomenon can be explained based on crystal defects and charge transfer. However, photoluminescence properties in the range from 660 to 800 nm of the respective doped systems have not been reported and a more extended study is still needed.

To complement this work, biological studies related with the biocompatibility need to be performed. Moreover, a detailed work about lithium doping hydroxyapatite with the high ultrasound sonication method is highly recommended. It should be carried out applying different ultrasonic times, calcination at different temperatures and different amounts of lithium compound. Besides, it is important to do a complete surface characterization and high resolution transmission electron microscopy.

Finally, this nanocomposites could be study for applications as reactive oxygen specie (ROS), biosensor, antibacterial and others.



## Appendix A

# Percentages of the different elements present in the samples obtained from EDS

Element	Series	[wt.%]	[norm. wt.%]	[norm at.%]	Error in wt.% (1 Sigma)
Phosphorous	K-series	12.17604531	9.437578998	5.573798085	0.505958423 7
Calcium	K-series	31.81715191	24.6612818	11.25626129	0.952818689
Carbon	K-series	26.57907998	20.60128397	31.37615215	3.19793724
Oxygen	K-series	58.44434149	45.29985523	51.79378847	6.593295248

Table A.1: Measured weight percentages of HAp doped with Lithium Perchlorate (25% w/w) using water as solvent.

Element	Series	[wt.%]	[norm. wt.%]	[norm at.%]	Error in wt.% (1 Sigma)
Phosphorus	K-series	11.95268649	18.69037954	32.92538871	0.498834226
Calcium	K-series	23.29771581	36.43056741	49.59827974	0.706062496
Cerium	L-series	28.7006077	44.87905304	17.47633154	0.788945617

Table A.2: Measured weight percentages of HAp doped with ceria NPs (0.1%v/w) using DMF as solvent.

Element	Series	[wt.%]	[norm. wt.%]	[norm at.%]	Error in wt.% (1 Sigma)
Phosphorus	K-series	19.69493995	24.45675215	33.73321172	0.804318882
Chlorine	K-series	0.726142985	0.901708715	1.086600224	0.052123811
Calcium	K-series	44.88697476	55.73967826	59.41707323	1.335056708
Cerium	L-series	15.22160476	18.90186087	5.763114825	0.433180363

Table A.3: Measured weight percentages of calcined HAP co-doped with ceria NPS (0.1% v/w) and Lithium Perchlorate (25% w/w) using DMF as solvent.

Element	Series	[wt.%]	[norm. wt.%]	[norm at.%]	Error in wt.% (1 Sigma)
Phosphorus	K-series	15.09354417	17.48526949	28.73816123	0.622704592
Chlorine	K-series	2.336687657	2.706959541	3.886986434	0.106491542
Calcium	K-series	36.53116543	42.3198995	53.75503668	1.091505314
Cerium	L-series	32.36008711	37.48787147	13.61981566	0.885662506

Table A.4: Measured weight percentages of calcined HAP co-doped with ceria NPs (0.1% v/w) and Lithium Perchlorate (25% w/w) using water as solvent

# Bibliography

- [1] T. J. Drake, X. Julia Zhao, and W. Tan, "Bioconjugated Silica Nanoparticles for Bioanalytical Applications," in *Nanobiotechnology*, pp. 444–457, Weinheim, FRG: Wiley-VCH Verlag GmbH & Co. KGaA, jan 2005.
- [2] P. Dogra, N. L. Adolph, Z. Wang, Y. S. Lin, K. S. Butler, P. N. Durfee, J. G. Croissant, A. Noureddine, E. N. Coker, E. L. Bearer, V. Cristini, and C. J. Brinker, "Establishing the effects of mesoporous silica nanoparticle properties on in vivo disposition using imaging-based pharmacokinetics," *Nature Communications*, vol. 9, pp. 1–14, dec 2018.
- [3] J. K. Patra, G. Das, L. F. Fraceto, E. V. R. Campos, M. D. P. Rodriguez-Torres, L. S. Acosta-Torres, L. A. Diaz-Torres, R. Grillo, M. K. Swamy, S. Sharma, S. Habtemariam, and H. S. Shin, "Nano based drug delivery systems: Recent developments and future prospects 10 Technology 1007 Nanotechnology 03 Chemical Sciences 0306 Physical Chemistry (incl. Structural) 03 Chemical Sciences 0303 Macromolecular and Materials Chemistry 11 Medical and He," *Journal of Nanobiotechnology*, vol. 16, sep 2018.
- [4] J. Li, D. Kuang, Y. Feng, F. Zhang, and M. Liu, "Glucose biosensor based on glucose oxidase immobilized on a nanofilm composed of mesoporous hydroxyapatite, titanium dioxide, and modified with multi-walled carbon nanotubes," *Microchimica Acta*, vol. 176, pp. 73–80, jan 2012.
- [5] A. Ślósarczyk, Z. Paszkiewicz, and C. Paluszkiwicz, "FTIR and XRD evaluation of carbonated hydroxyapatite powders synthesized by wet methods," in *Journal of Molecular Structure*, vol. 744-747, pp. 657–661, jun 2005.
- [6] I. Rehman and W. Bonfield, "Characterization of hydroxyapatite and carbonated apatite by photo acoustic FTIR spectroscopy," *Journal of Materials Science: Materials in Medicine*, vol. 8, pp. 1–4, jan 1997.
- [7] Y. Honda, T. Anada, S. Morimoto, Y. Shiwaku, and O. Suzuki, "Effect of Zn<sup>2+</sup> on the physicochemical characteristics of octacalcium phosphate and its hydrolysis into apatitic phases," *Crystal Growth and Design*, vol. 11, pp. 1462–1468, may 2011.
- [8] I. A. Neacsu, A. E. Stoica, B. S. Vasile, and E. Andronescu, "Luminescent hydroxyapatite doped with rare earth elements for biomedical applications," *Nanomaterials*, vol. 9, feb 2019.

- [9] S. Tavakol, M. R. Nikpour, E. Hoveizi, B. Tavakol, S. M. Rezayat, M. Adabi, S. Shajari Abokheili, and M. Jahanshahi, "Investigating the effects of particle size and chemical structure on cytotoxicity and bacteriostatic potential of nano hydroxyapatite/chitosan/silica and nano hydroxyapatite/chitosan/silver; as antibacterial bone substitutes," *Journal of Nanoparticle Research*, vol. 16, no. 10, 2014.
- [10] N. Matsumoto, K. Yoshida, K. Hashimoto, and Y. Toda, "Thermal stability of  $\beta$ -tricalcium phosphate doped with monovalent metal ions," *Materials Research Bulletin*, vol. 44, no. 9, pp. 1889–1894, 2009.
- [11] V. P. Padmanabhan, T. S. Sankara Narayanan, S. Sagadevan, M. E. Hoque, and R. Kulandaivelu, "Advanced lithium substituted hydroxyapatite nanoparticles for antimicrobial and hemolytic studies," *New Journal of Chemistry*, vol. 43, pp. 18484–18494, dec 2019.
- [12] A. A. White, S. M. Best, and I. A. Kinloch, "Hydroxyapatite-carbon nanotube composites for biomedical applications: A review," *International Journal of Applied Ceramic Technology*, vol. 4, pp. 1–13, jan 2007.
- [13] A. Y. Estevez, S. Pritchard, K. Harper, J. W. Aston, A. Lynch, J. J. Lucky, J. S. Ludington, P. Chatani, W. P. Mosenthal, J. C. Leiter, S. Andreescu, and J. S. Erlichman, "Neuroprotective mechanisms of cerium oxide nanoparticles in a mouse hippocampal brain slice model of ischemia," *Free Radical Biology and Medicine*, vol. 51, no. 6, pp. 1155–1163, 2011.
- [14] A. Hui, J. Liu, and J. Ma, "Synthesis and morphology-dependent antimicrobial activity of cerium doped flower-shaped ZnO crystallites under visible light irradiation," *Colloids and Surfaces A: Physicochemical and Engineering Aspects*, vol. 506, pp. 519–525, oct 2016.
- [15] L. Truffault, D. F. Rodrigues, H. R. N. Salgado, C. V. Santilli, and S. H. Pulcinelli, "Loaded Ce-Ag organic-inorganic hybrids and their antibacterial activity," *Colloids and Surfaces B: Biointerfaces*, vol. 147, pp. 151–160, nov 2016.
- [16] A. Hajjiah, E. Samir, N. Shehata, and M. Salah, "Lanthanide-doped ceria nanoparticles as backside coaters to improve silicon solar cell efficiency," *Nanomaterials*, vol. 8, p. 357, jun 2018.
- [17] M. Palard, J. Balencie, A. Maguer, and J. F. Hochepped, "Effect of hydrothermal ripening on the photoluminescence properties of pure and doped cerium oxide nanoparticles," *Materials Chemistry and Physics*, vol. 120, no. 1, pp. 79–88, 2010.
- [18] N. Shehata, E. Samir, S. Gaballah, A. Hamed, and A. Elrasheedy, "Embedded ceria nanoparticles in crosslinked PVA electrospun nanofibers as optical sensors for radicals," *Sensors (Switzerland)*, vol. 16, no. 9, 2016.
- [19] R. A. Freitas, "What is nanomedicine?," *Nanomedicine: Nanotechnology, Biology, and Medicine*, vol. 1, pp. 2–9, mar 2005.
- [20] Y. Xia, Y. Xiong, B. Lim, and S. E. Skrabalak, "Shape-controlled synthesis of metal nanocrystals: Simple chemistry meets complex physics?," jan 2009.

- [21] D. Peer, J. M. Karp, S. Hong, O. C. Farokhzad, R. Margalit, and R. Langer, "Nanocarriers as an emerging platform for cancer therapy," *Nature Nanotechnology*, vol. 2, pp. 751–760, dec 2007.
- [22] Y. Jin, S. Kannan, M. Wu, and J. X. Zhao, "Toxicity of luminescent silica nanoparticles to living cells," *Chemical Research in Toxicology*, vol. 20, pp. 1126–1133, aug 2007.
- [23] V. Wagner, A. Dullaart, A. K. Bock, and A. Zweck, "The emerging nanomedicine landscape," *Nature Biotechnology*, vol. 24, pp. 1211–1217, oct 2006.
- [24] N. Malik, T. Arfin, and A. U. Khan, "Graphene nanomaterials: Chemistry and pharmaceutical perspectives," in *Nanomaterials for Drug Delivery and Therapy*, pp. 373–402, Elsevier, jan 2019.
- [25] M. Sharon and A. Mewada, *Carbon Dots as Theranostic Agents*. Hoboken, NJ, USA: John Wiley & Sons, Inc., aug 2018.
- [26] I. L. Medintz, S. A. Trammell, H. Mattoussi, and J. M. Mauro, "Reversible Modulation of Quantum Dot Photoluminescence Using a Protein-Bound Photochromic Fluorescence Resonance Energy Transfer Acceptor," *Journal of the American Chemical Society*, vol. 126, pp. 30–31, jan 2004.
- [27] W. C. Chan and S. Nie, "Quantum dot bioconjugates for ultrasensitive nonisotopic detection," *Science*, vol. 281, pp. 2016–2018, sep 1998.
- [28] B. Pan, D. Cui, Y. Sheng, C. Ozkan, F. Gao, R. He, Q. Li, P. Xu, and T. Huang, "Dendrimer-modified magnetic nanoparticles enhance efficiency of gene delivery system," *Cancer Research*, vol. 67, pp. 8156–8163, sep 2007.
- [29] M. B. Esch, L. E. Locascio, M. J. Tarlov, and R. A. Durst, "Detection of Viable *Cryptosporidium* arvum Using DNA-Modified Liposomes in a Microfluidic Chip," *Analytical Chemistry*, vol. 73, pp. 2952–2958, jul 2001.
- [30] J. A. A. Ho and R. A. Durst, "Preparation of reagents for the determination of fumonisin B1 by flow-injection immunoanalysis," *Analytica Chimica Acta*, vol. 414, no. 1-2, pp. 51–60, 2000.
- [31] S. Santra, P. Zhang, K. Wang, R. Tapeç, and W. Tan, "Conjugation of biomolecules with luminophore-doped silica nanoparticles for photostable biomarkers," *Analytical Chemistry*, vol. 73, no. 20, pp. 4988–4993, 2001.
- [32] S. Santra, K. Wang, R. Tapeç, and W. Tan, "Development of novel dye-doped silica nanoparticles for biomarker application," *Journal of Biomedical Optics*, vol. 6, no. 2, p. 160, 2001.
- [33] E. J. Park, M. Brasuel, C. Behrend, M. A. Philbert, and R. Kopelman, "Ratiometric Optical PEBBLE Nanosensors for Real-Time Magnesium Ion Concentrations Inside Viable Cells," *Analytical Chemistry*, vol. 75, pp. 3784–3791, aug 2003.

- [34] J. H. Kim, S. H. Kim, H. K. Kim, T. Akaike, and S. C. Kim, "Synthesis and characterization of hydroxyapatite crystals: A review study on the analytical methods," *Journal of Biomedical Materials Research*, vol. 62, no. 4, pp. 600–612, 2002.
- [35] L. L. Hench, *An introduction to bioceramics*. second ed., 2013.
- [36] "Hydroxyapatite Ca<sub>5</sub>(OH)(PO<sub>4</sub>)<sub>3</sub>.." <https://www.chemtube3d.com/sshydroxyapatite/http://www.chemtube3d.com/solidstate/SSHhydroxyapatite.htm>. Accessed: 2020-08-29.
- [37] E. Rivera-Muñoz, "Hydroxyapatite-Based Materials: Synthesis and Characterization," in *Biomedical Engineering - Frontiers and Challenges*, InTech, aug 2011.
- [38] Y. Tang, Y. Du, Y. Li, X. Wang, and X. Hu, "A thermosensitive chitosan/poly(vinyl alcohol) hydrogel containing hydroxyapatite for protein delivery," *Journal of Biomedical Materials Research - Part A*, vol. 91, pp. 953–963, dec 2009.
- [39] A. Z. Alshemary, M. Akram, Y. F. Goh, M. R. Abdul Kadir, A. Abdolahi, and R. Hussain, "Structural characterization, optical properties and in vitro bioactivity of mesoporous erbium-doped hydroxyapatite," *Journal of Alloys and Compounds*, vol. 645, pp. 478–486, may 2015.
- [40] E. Boanini, M. C. Cassani, K. Rubini, C. Boga, and A. Bigi, "(9R)-9-hydroxystearate-functionalized anticancer ceramics promote loading of silver nanoparticles," *Nanomaterials*, vol. 8, jun 2018.
- [41] S. Salman, S. Soundararajan, G. Safina, I. Satoh, and B. Danielsson, "Hydroxyapatite as a novel reversible in situ adsorption matrix for enzyme thermistor-based FIA," *Talanta*, vol. 77, pp. 490–493, dec 2008.
- [42] M. Vallet-Regi and D. Navarrete, "Chapter 1: Biological apatites in bone and teeth," in *RSC Nanoscience and Nanotechnology*, vol. 2016-Janua, pp. 1–29, Royal Society of Chemistry, 2016.
- [43] M. S. Wickleder, "Crystal Structure of LiClO<sub>4</sub>," *Zeitschrift für anorganische und allgemeine Chemie*, vol. 629, pp. 1466–1468, aug 2003.
- [44] C. W. Kamienski, D. P. McDonald, M. W. Stark, and J. R. Papcun, "Lithium and Lithium Compounds," in *Kirk-Othmer Encyclopedia of Chemical Technology*, Hoboken, NJ, USA: John Wiley & Sons, Inc., apr 2004.
- [45] C. Korsvik, S. Patil, S. Seal, and W. T. Self, "Superoxide dismutase mimetic properties exhibited by vacancy engineered ceria nanoparticles," *Chemical Communications*, pp. 1056–1058, feb 2007.
- [46] F. Zhang, P. Wang, J. Koberstein, S. Khalid, and S. W. Chan, "Cerium oxidation state in ceria nanoparticles studied with X-ray photoelectron spectroscopy and absorption near edge spectroscopy," *Surface Science*, vol. 563, pp. 74–82, aug 2004.
- [47] S. Deshpande, S. Patil, S. V. Kuchibhatla, and S. Seal, "Size dependency variation in lattice parameter and valency states in nanocrystalline cerium oxide," *Applied Physics Letters*, vol. 87, pp. 1–3, sep 2005.

- [48] M. Mogensen, N. M. Sammes, and G. A. Tompsett, "Physical, chemical and electrochemical properties of pure and doped ceria," *Solid State Ionics*, vol. 129, pp. 63–94, apr 2000.
- [49] A. Trovarelli, *Catalysis by ceria and related materials*. London: Imperial College Press, reprinted. ed., 2005.
- [50] R. Street, "Defects and processes in nonmetallic solids," *IEEE Journal of Quantum Electronics*, vol. 22, no. 5, pp. 739–739, 2004.
- [51] K. Ghillanyova and D. Galusek, *Ceramics Science and Technology, Materials and Properties, vol 2*. John Wiley & Sons, 2011.
- [52] B. Rzigalinski, K. Meehan, R. M. Davis, and W. C. Miles, "Radical nanomedicine Article in Nanomedicine," *Nanomedicine*, vol. 1, pp. 399–412, dec 2007.
- [53] M. Nolan, J. E. Fearon, and G. W. Watson, "Oxygen vacancy formation and migration in ceria," *Solid State Ionics*, vol. 177, pp. 3069–3074, nov 2006.
- [54] N. Cioateră, V. Pârvulescu, A. Rolle, and R. N. Vannier, "Effect of dopant on the thermal and electrical behavior of nanostructured ceria materials," in *Proceedings of the International Semiconductor Conference, CAS*, vol. 2, pp. 317–320, 2010.
- [55] B. C. Steele and A. Heinzl, "Materials for fuel-cell technologies," *Nature*, vol. 414, pp. 345–352, nov 2001.
- [56] K. Suzuki, H. Miyazaki, Y. Yuzuriha, Y. Maru, and N. Izu, "Characterization of a novel gas sensor using sintered ceria nanoparticles for hydrogen detection in vacuum conditions," *Sensors and Actuators, B: Chemical*, vol. 250, pp. 617–622, oct 2017.
- [57] S. Tsunekawa, T. Fukuda, and A. Kasuya, "Blue shift in ultraviolet absorption spectra of monodisperse CeO<sub>2-x</sub> nanoparticles," *Journal of Applied Physics*, vol. 87, no. 3, pp. 1318–1321, 2000.
- [58] M. S. Rahman, E. K. Evangelou, A. Dimoulas, G. Mavrou, and S. Galata, "Anomalous charge trapping dynamics in cerium oxide grown on germanium substrate," *Journal of Applied Physics*, vol. 103, no. 6, 2008.
- [59] T. Dhannia, S. Jayalekshmi, M. C. Santhosh Kumar, T. Prasada Rao, and A. Chandra Bose, "Effect of iron doping and annealing on structural and optical properties of cerium oxide nanocrystals," *Journal of Physics and Chemistry of Solids*, vol. 71, no. 7, pp. 1020–1025, 2010.
- [60] M. Nyoka, Y. E. Choonara, P. Kumar, P. P. D. Kondiah, and V. Pillay, "Synthesis of Cerium Oxide Nanoparticles Using Various Methods: Implications for Biomedical Applications," *mdpi.com*, vol. 10, feb 2020.
- [61] T. Dhannia, S. Jayalekshmi, M. C. Santhosh Kumar, T. Prasada Rao, and A. Chandra Bose, "Effect of iron doping and annealing on structural and optical properties of cerium oxide nanocrystals," *Journal of Physics and Chemistry of Solids*, vol. 71, no. 7, pp. 1020–1025, 2010.
- [62] H. Leverenz, "Luminescence of solids," *Journal of Chemical Education*, vol. 27, no. 10, p. 586, 1950.

- [63] D. A. Skoog, F. J. Holler, and S. R. Crouch, *Principles of instrumental analysis*. Boston, MA: Cengage Learning, seventh ed., 2018.
- [64] K. V. Murthy and H. S. Virk, “Luminescence phenomena: An introduction,” 2014.
- [65] J. R. Lakowicz, *Principles of fluorescence spectroscopy*. third ed., 2006.
- [66] M. Y. Berezin and S. Achilefu, “Fluorescence lifetime measurements and biological imaging,” *Chemical Reviews*, vol. 110, pp. 2641–2684, may 2010.
- [67] H. C. Ishikawa-Ankerhold, R. Ankerhold, and G. P. Drummen, “Advanced fluorescence microscopy techniques-FRAP, FLIP, FLAP, FRET and FLIM,” 2012.
- [68] C. Ronda, *Luminescence: from theory to applications*. 2007.
- [69] S. McKeever, *Thermoluminescence of solids*. 1988.
- [70] G. Gonzalez, C. Costa-Vera, L. J. Borrero, D. Soto, L. Lozada, J. I. Chango, J. C. Diaz, and L. Lascano, “Effect of carbonates on hydroxyapatite self-activated photoluminescence response,” *Journal of Luminescence*, vol. 195, pp. 385–395, mar 2018.
- [71] K. Matsunaga and A. Kuwabara, “First-principles study of vacancy formation in hydroxyapatite,” *APS*, vol. 75, no. 1, 2007.
- [72] C. Zhang, J. Yang, Z. Quan, P. Yang, C. Li, Z. Hou, and J. Lin, “Hydroxyapatite nano- and microcrystals with multiform morphologies: Controllable synthesis and luminescence properties,” *Crystal Growth and Design*, vol. 9, pp. 2725–2733, jun 2009.
- [73] A. V. Bystrova, Y. D. Dekhtyar, A. I. Popov, J. Coutinho, and V. S. Bystrov, “Modified hydroxyapatite structure and properties: Modeling and synchrotron data analysis of modified hydroxyapatite structure,” *Ferroelectrics*, vol. 475, pp. 135–147, jan 2015.
- [74] T. R. Machado, J. C. Sczancoski, H. Beltrán-Mir, I. C. Nogueira, M. S. Li, J. Andrés, E. Cordoncillo, and E. Longo, “A novel approach to obtain highly intense self-activated photoluminescence emissions in hydroxyapatite nanoparticles,” *Elsevier*, 2016.
- [75] L. G. Bach, X. T. Cao, M. R. Islam, H. G. Kim, and K. T. Lim, “Combination of surface initiated reversible addition fragmentation chain transfer polymerization, thiol-ene click chemistry and coordination chemistry for the fabrication of a novel photoluminescent hydroxyapatite nanohybrids,” *Journal of Nanoscience and Nanotechnology*, vol. 15, pp. 5897–5900, jan 2015.
- [76] J. Chu and A. Sher, *Device Physics of Narrow Gap Semiconductors*. Springer New York, 2010.



- [77] R. C. Deus, J. A. Cortés, M. A. Ramirez, M. A. Ponce, J. Andres, L. S. R. Rocha, E. Longo, and A. Z. Simões, "Photoluminescence properties of cerium oxide nanoparticles as a function of lanthanum content," *Elsevier*, 2015.
- [78] D. D. Chung, "Cement-Matrix Composites," in *Carbon Composites*, pp. 333–386, Elsevier, jan 2017.
- [79] S. Bystryak, A. S. Peshkovsky, and S. L. Peshkovsky, "Scalable high-power ultrasonic technology for the production of translucent nanoemulsions," *Article in Chemical Engineering and Processing*, vol. 69, pp. 77–82, 2013.
- [80] Y. Wang, X. Yang, Z. Gu, H. Qin, L. Li, J. Liu, and X. Yu, "In vitro study on the degradation of lithium-doped hydroxyapatite for bone tissue engineering scaffold," *Materials Science and Engineering C*, vol. 66, pp. 185–192, sep 2016.
- [81] C. Yang, P. Yang, W. Wang, J. Wang, M. Zhang, and J. Lin, "Solvothermal synthesis and characterization of Ln (Eu<sup>3+</sup>, Tb<sup>3+</sup>) doped hydroxyapatite," *Journal of Colloid and Interface Science*, vol. 328, no. 1, pp. 203–210, 2008.
- [82] O. A. Graeve, R. Kanakala, A. Madadi, B. C. Williams, and K. C. Glass, "Luminescence variations in hydroxyapatites doped with Eu<sup>2+</sup> and Eu<sup>3+</sup> ions," *Biomaterials*, vol. 31, no. 15, pp. 4259–4267, 2010.
- [83] K. Ravindranadh, B. Babu, V. Pushpa Manjari, G. Thirumala Rao, M. C. Rao, and R. V. Ravikumar, "Optical and structural properties of undoped and Mn<sup>2+</sup> doped Ca–Li hydroxyapatite nanopowders using mechanochemical synthesis," *Journal of Luminescence*, vol. 159, pp. 119–127, 2015.
- [84] K. Ravindranadh, B. Babu, M. C. Rao, J. Shim, C. Venkata Reddy, and R. V. Ravikumar, "Structural and photoluminescence studies of Co<sup>2+</sup> doped Ca–Li hydroxyapatite nanopowders," *Journal of Materials Science: Materials in Electronics*, vol. 26, pp. 6667–6675, sep 2015.
- [85] C. S. Ciobanu, C. L. Popa, and D. Predoi, "Cerium-doped hydroxyapatite nanoparticles synthesized by the co-precipitation method," *Journal of the Serbian Chemical Society*, vol. 81, pp. 433–446, may 2016.
- [86] P. Phatai, C. M. Futralan, S. Utara, P. Khemthong, and S. Kamonwannasit, "Structural characterization of cerium-doped hydroxyapatite nanoparticles synthesized by an ultrasonic-assisted sol-gel technique," *Results in Physics*, vol. 10, pp. 956–963, 2018.
- [87] S. Chaudhary, P. Sharma, Renu, and R. Kumar, "Hydroxyapatite doped CeO<sub>2</sub> nanoparticles: Impact on biocompatibility and dye adsorption properties," *RSC Advances*, vol. 6, no. 67, pp. 62797–62809, 2016.
- [88] K. Li, Q. Shen, Y. Xie, M. You, L. Huang, and X. Zheng, "Incorporation of cerium oxide into hydroxyapatite coating protects bone marrow stromal cells against H<sub>2</sub>O<sub>2</sub>-induced inhibition of osteogenic differentiation," *Biological Trace Element Research*, vol. 182, no. 1, pp. 91–104, 2018.

- [89] S. M. Wahba, A. S. Darwish, and S. M. Kamal, "Ceria-containing uncoated and coated hydroxyapatite-based galantamine nanocomposites for formidable treatment of Alzheimer's disease in ovariectomized albino-rat model," *Materials Science and Engineering C*, vol. 65, pp. 151–163, aug 2016.
- [90] W. Huang, Z. Mao, L. Chen, Y. Chi, H. Jiang, B. L. Zimba, G. Xiong, and Q. Wu, "Synthesis and characterisation of fluorescent and biocompatible hydroxyapatite nanoparticles with cerium doping," *Micro and Nano Letters*, vol. 13, no. 5, pp. 699–703, 2018.
- [91] M. A. Fanovich, M. S. Castro, and J. M. Porto López, "Analysis of the microstructural evolution in hydroxyapatite ceramics by electrical characterisation," *Ceramics International*, vol. 25, no. 6, pp. 517–522, 1999.
- [92] P. Valério, F. N. Oktar, G. Goller, S. Ozyegin, A. P. Shainberg, A. M. Goes, and M. F. Leite, "Biocompatibility evaluation of lithium-hydroxyapatite composites," in *Key Engineering Materials*, vol. 309-311 II, pp. 1121–1124, 2006.
- [93] S.-H. Oh, S.-Y. Choi, Y.-K. Lee, K. Nam Kim, and S.-H. Choi, "Effects of lithium fluoride and maleic acid on the bioactivity of calcium aluminate cement: Formation of hydroxyapatite in simulated body fluid," *Journal of Biomedical Materials Research*, vol. 67A, pp. 104–111, oct 2003.
- [94] G.-L. Yang, F.-M. He, X.-F. Yang, X.-X. Wang, and S.-F. Zhao, "In vivo evaluation of bone-bonding ability of RGD-coated porous implant using layer-by-layer electrostatic self-assembly," *Journal of Biomedical Materials Research Part A*, vol. 90A, pp. 175–185, jun 2009.
- [95] J. Zhou, L. G. Ming, B. F. Ge, J. Q. Wang, R. Q. Zhu, Z. Wei, H. P. Ma, C. J. Xian, and K. M. Chen, "Effects of 50Hz sinusoidal electromagnetic fields of different intensities on proliferation, differentiation and mineralization potentials of rat osteoblasts," *Bone*, vol. 49, pp. 753–761, oct 2011.
- [96] N. Aydin and M. Bezer, "The effect of an intramedullary implant with a static magnetic field on the healing of the osteotomised rabbit femur," *International Orthopaedics*, vol. 35, pp. 135–141, jan 2011.
- [97] B. Henderson and G. Imbusch, *Optical Spectroscopy of Inorganic Solids*. Oxford [Oxfordshire] ;New York: Clarendon Press ;Oxford University Press, 1989.
- [98] I. Uysal, F. Severcan, A. Tezcaner, and Z. Evis, "Co-doping of hydroxyapatite with zinc and fluoride improves mechanical and biological properties of hydroxyapatite," *Progress in Natural Science: Materials International*, vol. 24, no. 4, pp. 340–349, 2014.
- [99] K. Ravindranadh, B. Babu, C. Venkata Reddy, J. Shim, M. C. Rao, and R. V. Ravikumar, "EPR and Optical Studies of Fe<sup>3+</sup>-Doped Ca–Li Hydroxyapatite Nanopowder: Mechanochemical Synthesis," *Applied Magnetic Resonance*, vol. 46, no. 1, 2015.
- [100] D. J. Stokes, *Principles and Practice of Variable Pressure/Environmental Scanning Electron Microscopy (VP-ESEM)*. 2008.

- [101] W. Zhou and Z. L. Wang, "Scanning Microscopy for Nanotechnology," tech. rep., 2006.
- [102] J. Goldstein, *Scanning Electron Microscopy and X-Ray Microanalysis*. Springer US, 2003.
- [103] H. Kohl and L. Reimer, "Transmission electron microscopy: physics of image formation," tech. rep., 2008.
- [104] C. Carter and D. Williams, *Transmission electron microscopy: Diffraction, imaging, and spectrometry*. 2016.
- [105] P. Van der Heide, *X-ray photoelectron spectroscopy: An introduction to principles and practices*. John Wiley & Sons, mar 2012.
- [106] J. F. Moulder, W. F. Stickle, P. E. Sobol, and K. D. Bomben, *08 Handbook of X-ray Photoelectron Spectroscopy*, vol. 3. Minnesota: Perkin-Elmer Corporation: Eden Prairie, 1979.
- [107] B. Crist, "Xps photoemission process - a 3 step model," 12 2018.
- [108] C. Cushman, S. Chatterjee, G. Major, N. Smith, A. Roberts, and M. Linford, "Trends in advanced xps instrumentation. 1. overview of the technique, automation, high sensitivity, imaging, snapshot spectroscopy, gas cluster ion beams, and multiple analytical techniques on the instrument.," *Vacuum Technology Coating*, 11 2016.
- [109] B. Smith, *Fundamentals of Fourier transform infrared spectroscopy*. CRC Press, 2011.
- [110] P. R. Griffiths and J. A. D. Haseth, "OICENTENNIAL. 1 807 A WILEY il 2 2007. ; > r Fourier Transform Infrared Spectrometry Second Edition," tech. rep., 2007.
- [111] PerkinElmer Life and Analytical Sciences, "FT-IR Spectroscopy Attenuated Total Reflectance (ATR)," 2005.
- [112] M. Hazle, M. Mehicic, D. Gardiner, and P. Graves, "Practical Raman Spectroscopy," *Vibrational Spectroscopy*, vol. 1, no. 1, p. 104, 1990.
- [113] G. D. Nascimento, *Raman Spectroscopy*. InTech, apr 2018.
- [114] E. Smith and G. Dent, *Modern Raman Spectroscopy*. Wiley, second ed., feb 2019.
- [115] U. Sahoo, A. Seth, and R. Chawla, *UV/ Visible Spectroscopy: Absorption Spectroscopy*. Saarbrücken: LAP LAMBERT Academic Publishing, 2012.
- [116] J. I. Pankove and Physics, *Optical Processes in Semiconductors (Dover Books on Physics)*. 2010.
- [117] P. Kubelka and F. Munk, "An Article on Optics of Paint Layers (engl. Übersetzung)," *Z. Tech. Phys*, vol. 12, no. 1930, pp. 593–601, 1931.
- [118] R. López and R. Gómez, "Band-gap energy estimation from diffuse reflectance measurements on sol-gel and commercial TiO<sub>2</sub>: A comparative study," *Journal of Sol-Gel Science and Technology*, vol. 61, pp. 1–7, jan 2012.

- [119] J. Tauc, R. Grigorovici, and A. Vancu, "Optical Properties and Electronic Structure of Amorphous Germanium," *physica status solidi (b)*, vol. 15, no. 2, pp. 627–637, 1966.
- [120] S. G. Rathod, R. F. Bhajantri, V. Ravindrachary, P. K. Pujari, and T. Sheela, "Ionic conductivity and dielectric studies of LiClO<sub>4</sub> doped poly(vinylalcohol)(PVA)/chitosan(CS) composites," *Journal of Advanced Dielectrics*, vol. 04, p. 1450033, oct 2014.
- [121] T. Library, *Photoluminescence, Phosphorescence, and Fluorescence Spectroscopy: Physical*. Independently Published, 2019, 2019.
- [122] S. Rotman, *Wide-gap luminescent materials: theory and applications*. Springer, 1997.
- [123] A. Kitai, *Luminescent materials and applications*, vol. 25. West Sussex: John Wiley & Sons, Ltd, 2008.
- [124] V. M. Gerrish, "Characterization and Quantification of Detector Performance," in *Semiconductors and Semimetals*, vol. 43, pp. 493–530, 1995.
- [125] U. König, R. S. Angélica, N. Norberg, and L. Gobbo, "Rapid X-ray diffraction (XRD) for grade control of bauxites," *Icsoba 2012*, no. November 2012, p. 11, 2012.
- [126] J. P. Patel and P. H. Parsania, "Characterization, testing, and reinforcing materials of biodegradable composites," in *Biodegradable and Biocompatible Polymer Composites: Processing, Properties and Applications*, pp. 55–79, Elsevier, jan 2017.
- [127] "Methods for Assessing Surface Cleanliness," in *Developments in Surface Contamination and Cleaning, Volume 12* (R. Kohli and K. Mittal., eds.), pp. 23–105, Elsevier, jan 2019.
- [128] M. M. Heravi, M. Ghavidel, and L. Mohammadkhani, "Beyond a solvent: Triple roles of dimethylformamide in organic chemistry," *RSC Advances*, vol. 8, no. 49, pp. 27832–27862, 2018.
- [129] S. Rades, V. D. Hodoroaba, T. Salge, T. Wirth, M. P. Lobera, R. H. Labrador, K. Natte, T. Behnke, T. Gross, and W. E. Unger, "High-resolution imaging with SEM/T-SEM, EDX and SAM as a combined methodical approach for morphological and elemental analyses of single engineered nanoparticles," *RSC Advances*, vol. 4, no. 91, pp. 49577–49587, 2014.
- [130] N. Rameshbabu, T. S. Kumar, T. G. Prabhakar, V. S. Sastry, K. V. Murty, and K. Prasad Rao, "Antibacterial nanosized silver substituted hydroxyapatite: Synthesis and characterization," *Journal of Biomedical Materials Research - Part A*, vol. 80, pp. 581–591, mar 2007.
- [131] J. Kolmas, E. Groszyk, and U. Piotrowska, "Nanocrystalline hydroxyapatite enriched in selenite and manganese ions: physicochemical and antibacterial properties," *Nanoscale Research Letters*, vol. 10, pp. 1–9, dec 2015.
- [132] A. Grunenwald, C. Keyser, A. Sautereau, E. Crubézy, B. Ludes, and C. Drouet, "Revisiting carbonate quantification in apatite (bio)minerals: a validated FTIR methodology," *Journal of Archaeological Science*, vol. 49, pp. 134–141, sep 2014.

- [133] A. Kafilak, A. Ślósarczyk, and W. Kolodziejcki, "A comparative study of carbonate bands from nanocrystalline carbonated hydroxyapatites using FT-IR spectroscopy in the transmission and photoacoustic modes," *Journal of Molecular Structure*, vol. 997, no. 1-3, pp. 7–14, 2011.
- [134] F. Ren and Y. Leng, "Carbonated apatite, Type-A or Type-B?," *Key Engineering Materials*, vol. 493-494, pp. 293–297, 2012.
- [135] M. Kazanci, P. Fratzl, K. Klaushofer, and E. P. Paschalis, "Complementary information on in vitro conversion of amorphous (precursor) calcium phosphate to hydroxyapatite from raman microspectroscopy and wide-angle X-ray scattering," *Calcified Tissue International*, vol. 79, pp. 354–359, nov 2006.
- [136] Y. H. Liu, J. C. Zuo, X. F. Ren, and L. Yong, "SYNTHESIS AND CHARACTER OF CERIUM OXIDE (CeO<sub>2</sub>) NANOPARTICLES BY THE PRECIPITATION METHOD," *Metalurgija*, vol. 4, pp. 463–465, oct 2014.
- [137] L. Qiu, J. Lin, L. Wang, W. Cheng, Y. Cao, X. Liu, and S. Luo, "A Series of Imidazolyl-Containing Bisphosphonates with Abundant Hydrogen-Bonding Interactions: Syntheses, Structures, and Bone-Binding Affinity," *Australian Journal of Chemistry*, vol. 67, p. 192, mar 2014.
- [138] E. Mavropoulos, M. Hausen, A. M. Costa, G. Alves, A. Mello, C. A. Ospina, M. Mir, J. M. Granjeiro, and A. M. Rossi, "The impact of the RGD peptide on osteoblast adhesion and spreading on zinc-substituted hydroxyapatite surface," *Journal of Materials Science: Materials in Medicine*, vol. 24, no. 5, pp. 1271–1283, 2013.
- [139] C. Battistoni, M. P. Casaletto, G. M. Ingo, S. Kaciulis, G. Mattogno, and L. Pandolfi, "Surface characterization of biocompatible hydroxyapatite coatings," *Surface and Interface Analysis*, vol. 29, pp. 773–781, nov 2000.
- [140] W. E. Morgan, J. R. Van Wazer, and W. J. Stec, "Inner-Orbital Photoelectron Spectroscopy of the Alkali Metal Halides, Perchlorates, Phosphates, and Pyrophosphates," *Journal of the American Chemical Society*, vol. 95, pp. 751–755, feb 1973.
- [141] M. A. Stranick and M. J. Root, "Influence of strontium on monofluorophosphate uptake by hydroxyapatite XPS characterization of the hydroxyapatite surface," *Colloids and Surfaces*, vol. 55, pp. 137–147, jan 1991.
- [142] T. Hanawa and M. Ota, "Calcium phosphate naturally formed on titanium in electrolyte solution," *Biomaterials*, vol. 12, pp. 767–774, oct 1991.
- [143] N. T. T. Linh, P. D. Tuan, and N. V. Dzung, "The Shifts of Band Gap and Binding Energies of Titania/Hydroxyapatite Material," *Journal of Composites*, vol. 2014, pp. 1–5, 2014.
- [144] D. F. Mercado, G. Magnacca, M. Malandrino, A. Rubert, E. Montoneri, L. Celi, A. Bianco Prevot, and M. C. Gonzalez, "Paramagnetic iron-doped hydroxyapatite nanoparticles with improved metal sorption properties. A bioorganic substrates-mediated synthesis," *ACS Applied Materials and Interfaces*, vol. 6, pp. 3937–3946, mar 2014.

- [145] A. E. Hughes, J. D. Gorman, P. J. Patterson, and R. Carter, "Unusual peak shifts in the core levels of CeO<sub>2</sub> films deposited on Si(100)," *Surface and Interface Analysis*, vol. 24, pp. 634–640, sep 1996.
- [146] T. L. Barr, C. G. Fries, F. Cariati, J. C. Bart, and N. Giordano, "A spectroscopic investigation of cerium molybdenum oxides," *Journal of the Chemical Society, Dalton Transactions*, pp. 1825–1829, jan 1983.
- [147] E. Paparazzo, G. M. Ingo, and N. Zacchetti, "X-ray induced reduction effects at CeO<sub>2</sub> surfaces: An x-ray photoelectron spectroscopy study," *Journal of Vacuum Science & Technology A: Vacuum, Surfaces, and Films*, vol. 9, pp. 1416–1420, may 1991.
- [148] H. Sebei, D. Pham Minh, A. Nzihou, and P. Sharrock, "Sorption behavior of Zn(II) ions on synthetic apatitic calcium phosphates," *Applied Surface Science*, vol. 357, pp. 1958–1966, dec 2015.
- [149] J. L. Grosseau-Poussard, B. Panicaud, F. Pedraza, P. O. Renault, and J. F. Silvain, "Iron oxidation under the influence of phosphate thin films," *Journal of Applied Physics*, vol. 94, pp. 784–788, jul 2003.
- [150] M. Engelhard, S. Azad, C. Peden, and S. Thevuthasan, "X-ray Photoelectron Spectroscopy Studies of Oxidized and Reduced CeO<sub>2</sub> (111) Surfaces," *Surface Science Spectra*, vol. 11, pp. 73–81, dec 2004.
- [151] M. E. Fleet, X. Liu, and P. L. King, "Accommodation of the carbonate ion in apatite: An FTIR and X-ray structure study of crystals synthesized at 2–4 GPa," *American Mineralogist*, vol. 89, pp. 1422–1432, oct 2004.
- [152] E. Mamontov and T. Egami, "Structural defects in a nano-scale powder of CeO<sub>2</sub> studied by pulsed neutron diffraction," *Journal of Physics and Chemistry of Solids*, vol. 61, pp. 1345–1356, aug 2000.
- [153] R. W. G. Wyckoff, "Interscience publishers, new york, new york rocksalt structure," *Crystal structures*, vol. 1, pp. 85–237, 1963.
- [154] J. C. Elliott, "Structure and chemistry of the apatites and other calcium orthophosphates," *Studies in Organic Chemistry*, vol. 18, pp. 94008066–94008066, 1994.
- [155] E. A. Ofudje, A. I. Adeogun, M. A. Idowu, and S. O. Kareem, "Synthesis and characterization of Zn-Doped hydroxyapatite: scaffold application, antibacterial and bioactivity studies," *Heliyon*, vol. 5, p. e01716, may 2019.
- [156] A. Slepko and A. A. Demkov, "First-principles study of the biomineral hydroxyapatite," *Physical Review B - Condensed Matter and Materials Physics*, vol. 84, p. 134108, oct 2011.
- [157] M. Tsukada, M. Wakamura, N. Yoshida, and T. Watanabe, "Band gap and photocatalytic properties of Ti-substituted hydroxyapatite: Comparison with anatase-TiO<sub>2</sub>," *Journal of Molecular Catalysis A: Chemical*, vol. 338, pp. 18–23, mar 2011.
- [158] L. Calderín, M. J. Stott, and A. Rubio, "Electronic and crystallographic structure of apatites," *Physical Review B - Condensed Matter and Materials Physics*, vol. 67, p. 134106, apr 2003.

- [159] G. Rosenman, D. Aronov, L. Oster, J. Haddad, G. Mezinskis, I. Pavlovska, M. Chaikina, and A. Karlov, "Photoluminescence and surface photovoltage spectroscopy studies of hydroxyapatite nano-Bio-ceramics," *Journal of Luminescence*, vol. 122-123, pp. 936–938, jan 2007.
- [160] I. N. Bazhukova, S. Y. Sokovnin, V. G. Ilves, A. V. Myshkina, R. A. Vazirov, N. Pizurova, and V. V. Kasyanova, "Luminescence and optical properties of cerium oxide nanoparticles," *Optical Materials*, vol. 92, no. October 2018, pp. 136–142, 2019.
- [161] V. S. Bystrov, C. Piccirillo, D. M. Tobaldi, P. M. Castro, J. Coutinho, S. Kopyl, and R. C. Pullar, "Oxygen vacancies, the optical band gap ( $E_g$ ) and photocatalysis of hydroxyapatite: Comparing modelling with measured data," *Applied Catalysis B: Environmental*, vol. 196, pp. 100–107, 2016.
- [162] A. Filtschew, K. Hofmann, and C. Hess, "Ceria and Its Defect Structure: New Insights from a Combined Spectroscopic Approach," *Journal of Physical Chemistry C*, vol. 120, pp. 6694–6703, mar 2016.